

Dynamics of Seminal PV Elements

A dissertation submitted to the
SWISS FEDERAL INSTITUTE OF TECHNOLOGY (ETH)
ZÜRICH

for the degree of
DOCTOR OF NATURAL SCIENCE

presented by
RENÉ FEHLMANN
Dipl. Phys. ETH
born 23 April 1966
citizen of Buchs (SG)



CatE

accepted on the recommendation of
Prof. Dr. H. C. Davies, examiner
Dr. A. J. Simmons, co-examiner
Prof. Dr. C. Schär, co-examiner

Leer - Vide - Empty

Für Ursula

Leer - Vide - Empty

Contents

Abstract	ix
Zusammenfassung	xi
1 Introduction	1
1.1 The Concepts of the Mid-Latitude Flow Phenomena	1
1.1.1 Synoptic Scale Cyclogenesis	2
1.1.2 Frontal Waves	3
1.2 Aims of this Study	3
2 Basic Notions and Tools	5
2.1 The Concept of Potential Vorticity	5
2.2 Models and Data Set	10
2.2.1 The Quasi-Geostrophic Model	11
2.2.2 ECMWF Data	12
2.2.3 The Europa-Modell	13
2.3 Diagnostic Tools	13
2.3.1 Condensational Heating	14
2.3.2 Lagrangian Trajectories	15
2.3.3 Potential Vorticity Inversion	16
2.3.4 Q -vector diagnostics	18
3 Idealised Studies	21
3.1 Introduction	21
3.2 Some Comparative Features	24
3.2.1 Analytical Solutions of Shear Lines in QG, BQG and SQG	25
3.2.2 Analytical Solutions of (Ellipsoidal) Elliptical Vortices in (QG), BQG and SQG	26
3.3 Linear Instability	28
3.3.1 Basic State	28
3.3.2 Normal Mode Analysis	30
3.3.3 Mathematical Symmetries	31
3.3.4 Growth Rates, Wave Lengths, and Structures of the Normal Modes	31

3.4	Nonlinear QG-Simulations	38
3.4.1	Infinite Band, Normal Mode Initial Conditions	39
3.4.2	Finite Strips	44
3.5	PE Simulations of Interior PV Anomalies	47
3.5.1	Low-Level PV-Bands	47
3.5.2	Upper-Level Intrusions	49
3.6	Discussion	52
4	Case Study of a Frontal Wave Cyclone	55
4.1	Introduction	55
4.2	PV Structures of a Frontal Cyclogenesis Event	57
4.3	Diabatic Processes	61
4.3.1	Model Derived Precipitation	61
4.3.2	\mathbf{Q} -Vector Analysis	62
4.3.3	Diabatic Heating and PV Rates	62
4.3.4	Lagrangian Trajectory Analysis of the Low-Level PV-Band	66
4.4	Dry Simulations	67
4.5	Dry Simulation with a Diagnosed PV-Rate	71
4.6	Inversion of Key PV Elements	73
4.6.1	The Low-Level PV-Band	73
4.6.2	The Upper-Level Anomaly P_{s1}	75
4.6.3	The Upper-Level Anomaly P_{s2}	75
4.7	The Influence of the Upper-Level Structure	75
4.7.1	A Simulation without Anomaly P_{s1}	77
4.7.2	A Simulation without Anomaly P_{s2}	78
4.8	Discussion	79
5	PV-Retrodiction	83
5.1	Introduction	83
5.2	The Approach	84
5.3	A Case-Study	85
5.3.1	Synopsis of the Analysed Event	85
5.3.2	A Forecast	89
5.3.3	Application of the Approach	90
5.3.4	Discussion	93
5.4	Further Remarks	96
6	Climatology of PV-errors	99
6.1	The Approach	99
6.1.1	Error Measures	101
6.2	Results	102
6.2.1	The Seasonal Analysis for 1993	103
6.2.2	The Period of February 1997 – FASTEX Cases	108

6.3 Discussion	109
7 Further Remarks	111
A Potential Vorticity Inversion	115
A.1 Mathematical Formulation of the Problem	115
A.2 Discretization and Numerical Algorithm	117
B Exact Solutions of Shear Lines	121
B.1 Infinite θ -Band	121
B.2 Infinite PV-Band	122
B.3 The Kirchhoff Ellipse	125
C The Profile Parameter	127
D Linear Instability	129
D.1 Transformation into an Algebraic Problem	129
D.2 Numerical Treatment	130
E The Resolution and the Domain Size	131
References	133
Acknowledgments / Dank	141
Curriculum Vitae	143

Leer - Vide - Empty

Abstract

Cyclones and anticyclones are the dominant synoptic scale meteorological weather systems in midlatitudes. An attractive way to study dynamical aspects of these structures is provided by the PV framework. From this perspective an atmospheric *state* can be viewed as an assemblage of distinct PV anomalies, and the associated *dynamics* can be interpreted in terms of the self-development and interaction of seminal PV elements. In this thesis several aspects of midlatitude cyclogenesis are investigated within this PV framework using idealised and NWP models and case study analyses.

In the first part of the thesis aspects of the dynamics of idealised PV structures that are considered to be pivotal for the genesis of extratropical cyclones are studied within idealised dynamical frameworks – quasi-geostrophic and PE dynamics on an f -plane – and with simple ambient flow settings. Classical normal mode analysis is performed for a basic state comprising localised interior PV/surface warm bands with the ambient flow structure prescribed by a uniform barotropic and/or baroclinic shear. Aspects of the nonlinear development of the most unstable modes are also investigated as well as the dynamics of bands of finite length. It is demonstrated that different ambient flow characteristics as well as the structure of the shear line itself generate a palette of unstable modes with a wide range of different wave lengths and growth rates. In the nonlinear phase these anomalies are strongly influenced by the ambient flow structure. The results corroborate and extend the findings from earlier studies, e.g. the stabilisation due to adverse shear, and secondary instabilities or stabilisation of strong PV (or θ) gradients at the edges of the bands for certain ambient flow settings.

In the second part a case study of one particular frontal wave development is undertaken. The analysis of this event is based on the initialised analysis fields of the ECMWF and on simulations with a limited area model. Simulations for different initial configurations, characterised by modified upper-level PV structures, and with and without parametrised physical subgrid-scale processes, suggest that at least for this particular case the development of the secondary cyclone depends crucially on the structure and the evolution of a low-level prefrontal PV band induced by condensational heating. Simulations where condensational subgrid-scale processes are replaced by diagnostically deduced PV rates lend credence to this interpretation of frontal waves.

The remainder of the thesis is devoted to problems concerning misforecasts of numerical weather prediction (NWP) models. The uncertainty of forecasts made with such NWP models arises from uncertainty caused by two distinct error sources: (i) imperfections in

the model formulations, and (ii) errors in the specification of the initial model state. Here a diagnostic tool is developed to analyse the contribution of the latter source to misforecasts. It makes use of the time history of the dynamical fields and fundamental physical conservation properties and is based on the PV perspective. The tool is applied to one misforecast of a rapidly developing Atlantic cyclone. Thereby insight is gained on the localised geographical distribution of the inaccuracy in the initial analysis fields – expressed in terms of PV errors. Moreover, this diagnostic method provides some insights to the dynamics of the misforecast and in particular points to the importance, at least for this particular frontal wave cyclone, of tropopause level structures for the development.

As a rider to this study a first step is made to derive a statistical climatology of the distribution of initial state PV errors. This can help to indicate where there is need for an improved observational data set by either routine observations or adaptive strategies. The analysis is performed for the northern Atlantic sector for the year of 1993. It is found that errors in the initial fields occur dominantly at the entrance to the Atlantic storm track. The climatology of PV errors can also point on the geographical location where strong diabatic processes at tropopause levels occur, and thereby provides some indication of the distribution of local irreversible mixing of stratospheric and tropospheric air by diabatical decay of PV streamers at the end of the Atlantic storm track.

Taken together the foregoing studies serve to illustrate the intrinsic usefulness of the PV perspective as a framework for prompting theoretical and observational studies that both shed light upon the dynamics and prediction of synoptic-scale atmospheric flow.

Zusammenfassung

Die dominanten synoptisch skaligen Wettersysteme in mittleren Breiten sind Tief- und Hochdruckgebiete. Das Konzept der potentiellen Wirbelstärke (PV) liefert einen interessanten Ansatz, um Aspekte dieser dynamischen Strukturen zu studieren. Innerhalb dieses Konzepts kann ein atmosphärischer *Zustand* als eine Verteilung von verschiedenen PV-Anomalien betrachtet werden. Die zugehörige *Dynamik* wird dann durch die Selbstentwicklung und Wechselwirkung dieser erzeugenden PV-Elemente beschrieben. In der vorliegenden Arbeit werden innerhalb dieses Konzepts mehrere Aspekte der Zyklogenese in mittleren Breiten mittels idealisierter und numerischer Wettervorhersagemodelle untersucht.

Im ersten Teil der Arbeit werden mittels idealisierter dynamischer Werkzeuge – Dynamik, basierend auf den quasi-geostrophischen und primitiven Gleichungen auf einer f -Ebene – dynamische Aspekte idealisierter PV-Strukturen mit einfachen umgebenden Strömungsstrukturen untersucht, welche man als zentral bezüglich der Entstehung außertropischer Tiefdruckgebiete betrachtet. Für Grundzustände, welche lokale innere PV- oder warme Bodenbänder darstellen und welchen barotrope und/oder barokline Scherungen überlagert sind, wird eine klassische Normalmoden Analyse durchgeführt. Ebenso werden Aspekte der nicht linearen Entwicklung der instabilsten Normalmoden und die Dynamik von Bändern endlicher Länge untersucht. Es wird gezeigt, dass verschiedene Charakteristika der umgebenden Strömung sowie die Struktur der Scherungslinie selbst eine Palette von instabilen Moden mit einem weiten Spektrum von verschiedenen Wellenlängen und Wachstumsraten erzeugen. In der nicht linearen Phase werden diese Anomalien wesentlich durch die umgebende Strömung beeinflusst. Die Resultate bestätigen und erweitern Erkenntnisse früherer Arbeiten, z.B. die Stabilisierung durch entgegenwirkende Scherung und sekundäre Instabilitäten oder Stabilisierung von starken PV (oder θ) Gradienten an den Kanten der Bänder für gewisse Spezifikationen der umgebenden Strömung.

Im zweiten Teil wird eine Fallstudie einer speziellen frontalen Wellenentwicklung unternommen. Die Analyse dieses Ereignisses basiert auf initialisierten Analysefeldern des EZMWs und auf Simulationen mit einem Modell, welches auf einem endlichen Gebiet operiert. Simulationen für verschiedene Anfangskonfigurationen, welche durch verschiedene Strukturen der oberen PV-Verteilung charakterisiert sind und solche mit und ohne parametrisierten physikalischen Prozessen, welche auf einer kleineren Skala als der des Modells stattfinden, legen nahe, dass, zumindest in dem vorliegenden Fall, die Entwicklung der sekundären Zyklone wesentlich von der Struktur und der Entwicklung eines präfrontalen troposphärischen PV-Bandes, welches durch diabatisches heizen induziert wird, abhängt. Simulationen, bei welchen die parametrisierten Kondensationsprozesse durch diagnostisch ermit-

telte PV-Raten ersetzt werden, lassen diese Interpretation von frontalen Wellen glaubwürdig erscheinen.

Der restliche Teil dieser Arbeit ist Problemen gewidmet, welche die Fehlvorhersage von numerischen Wettervorhersagemodellen betreffen. Die Unsicherheit der Wettervorhersage mit solch numerischen Modellen entsteht durch Unsicherheiten, deren Ursache zwei verschiedene Quellen haben: (i) Ungenauigkeiten in der Formulierung des Modells und (ii) Fehler in der Spezifizierung des Anfangszustandes. Hier wird ein diagnostisches Hilfsmittel entwickelt, um den Beitrag zu Fehlvorhersagen der letzteren obengenannten Quelle zu analysieren. Dieses Hilfsmittel benützt die Zeitentwicklung der dynamischen Felder zusammen mit fundamentalen physikalischen Erhaltungssätzen und ist auf dem PV-Konzept begründet. Es wird auf eine Fehlvorhersage einer sich schnell entwickelnden atlantischen Zyklone angewendet. Dadurch werden Einsichten bezüglich der lokalisierten geographischen Verteilung von Ungenauigkeiten in den Anfangsdaten gewonnen – ausgedrückt durch PV-Fehler. Überdies liefert diese diagnostische Methode Einblicke in die Dynamik von Fehlvorhersagen und im speziellen weist sie, zumindest in der vorliegenden frontalen Wellenzyklone, auf die Wichtigkeit für die Entwicklung von Strukturen auf der Tropopausenhöhe hin.

Zusätzlich zu dieser Studie wird ein erster Schritt gemacht, um eine statistische Klimatologie der Verteilung von PV-Fehlern in den Anfangsdaten zu gewinnen. Solch eine Analyse kann einen Hinweis liefern, wo Bedarf für eine Verbesserung entweder durch routinemässige oder adaptive Messmethoden im Beobachtungsnetz besteht. Die Analyse wird für den nördlichen atlantischen Sektor für das Jahr 1993 durchgeführt. Es stellt sich heraus, dass PV-Fehler in den Startfeldern vorwiegend beim Eingang der atlantischen Sturmbahn auftreten. Die Klimatologie der PV-Fehler kann ebenso auf die geographische Lage von starken diabatischen Prozessen, welche auf Tropopausenhöhe stattfinden, hinweisen und liefert dadurch einige Anhaltspunkte betreffend der Verteilung von lokalen, irreversiblen Mischprozessen von stratosphärischer und troposphärischer Luft durch diabatischen Zerfall von PV-Bändern am Ende der atlantischen Sturmbahn.

Chapter 1

Introduction

The dominant synoptic-scale, midlatitude weather phenomena are cyclones and anticyclones. Their characteristic length scale is $\sim 2000 - 4000$ km. Within these structures other sub-synoptic- or meso-scale features can develop such as fronts, and wave-developments on the fronts.

The sub-synoptic- and meso-scale features can in turn interact with the synoptic-scale systems on a comparatively short time scale (~ 1 day) and thereby influence the overall synoptic development, for example via latent heat release through cloud condensation.

One task of the weather services is the prediction of these weather elements. An inaccurate representation of the atmospheric systems or the dynamical and physical processes may cause mis-forecasts of numerical weather prediction models. Therefore from both a theoretical and forecasting standpoint there is need for further study of the inter-scale interactions. In fact the observation programme FASTEX will provide an observational data base for the further study of these systems.

One dynamically-based approach to the study of these atmospheric flow phenomena and their interaction is the potential vorticity (PV) framework. In this framework the development and interaction of the flow features are described as the self-development and interaction of certain key PV elements.

The approach adopted in the present study is to investigate the generation and dynamics of seminal atmospheric PV elements. It involves both, the use of idealised models and case study analyses of the dynamics of typical PV features associated with synoptic and sub-synoptic midlatitude atmospheric flow.

1.1 The Concepts of the Mid-Latitude Flow Phenomena

The Bergen school frontal model (Bjerknes 1919, Bjerknes and Solberg 1922) was a landmark in the development of descriptive theories of cyclogenesis and still influences the construction of weather charts. Their ‘structure model’ describes the formation of a family of midlatitude cyclones on a pre-existing baroclinic zone, the ‘polar front’. The life cycle of one such cyclone was envisaged to start as a small perturbation on the polar front that then evolved a cold

and a warm front structure. In the final phase of the development the latter is overtaken by the cold front. This conceptual model has been extended by adding to the frontal structures the notions of a T-bone structure, bent-back warm front and cold frontal fracture (Shapiro and Keyser 1990).

It has been recognised that in addition to the pure wave instability mechanism of the baroclinic zone another cyclogenesis mechanism can be the coupling of the surface development with upper-level flow structures. For example Petterssen and Smebye (1971) identified two prototypes of cyclogenesis: a type A development describes the continuously growing of an initially small disturbance, a type B development the interaction of an upper-level disturbance which moves over a baroclinic zone near the surface.

The structure models have influenced, and been influenced by a series of analytical, idealised numerical, and case study analyses and contributed to a better descriptive formulation of the atmospheric flow phenomena.

1.1.1 Synoptic Scale Cyclogenesis

The Bergen School conceptual model of cyclogenesis has been followed by many theoretical studies of baroclinic instability. The earlier work was that of Charney (1947) and Eady (1949). Eady found that in the quasi-geostrophic limit a basic state of uniform horizontal temperature gradient is unstable to linear perturbations. The wavelength (~ 4000 km) and a growth rate (~ 2 days) of the most unstable mode are comparable to the observed large scale cyclones. Thereafter a number of studies with a more realistic basic state have been undertaken in the quasi-geostrophic, semi-geostrophic or primitive equation framework, and with f -plane, β -plane or spherical geometry (for a partial list of these idealised studies see Wernli 1995).

It is generally accepted that large scale cyclones gain most of their energy by a conversion of the baroclinic energy of the basic state. The palette of front-structures and life cycles of cyclones is determined by the ambient flow (e.g. the barotropic wind shear) but not so much by the initial state perturbation. Early idealised simulations of the growing phase of large scale extratropical cyclones in spherical geometry with primitive equation dynamics are those by Gall (1976) and Simmons and Hoskins (1976). Later with an increased resolution of the numerical models the simulation of the baroclinic waves could be continued over the full life cycle including maturity and decay (Simmons and Hoskins 1978, Simmons and Hoskins 1979). It could be shown that during the growing phase conversion of baroclinic into kinetic energy has been the main driving mechanism and during the decay barotropic processes became more important. (For a review of these simulations see Simmons 1994.)

It has been shown by Davies et al. (1991) that an ambient wind shear 'modifies the track, strength, horizontal scale shape and the vertical tilt of the highs and lows and the occurrence, intensity, and vertical coherence of the fronts'. In their study the observed front structures in a cyclonically sheared development resemble that of the Shapiro-Keyser model. The study by Thorncroft et al. (1993) shows that a barotropic shear influences the occurrence of upper level features: The tropopause PV (or θ) structures turn either cyclonically to give a large scale roll-up, or anticyclonically to form an elongated streamer.

1.1.2 Frontal Waves

Interest in frontal waves, as instabilities of midlatitude frontal zones, goes back beyond the time of the Bergen school. Subsequent studies in the late 1980's have led to significant advances. Within the baroclinic waves of the aforementioned synoptic scale cyclones, the action of the deformation of the basic state is to form locally intense fronts which attain small length scales in finite time. The resulting intense fronts may themselves undergo instability to form secondary cyclones. These secondary systems occur on the mesoscale, can have extremely large growth rates, and are notoriously difficult to forecast. Many recent studies have focused on these secondary instabilities, although it could be argued that the difference between the secondary systems and their parent instabilities might only be one of scale. For example in a simulation of the basic life cycle experiment of Simmons and Hoskins (1980) with an increased resolution, the development of a secondary frontal wave can be observed (Thorncroft and Hoskins 1990).

The issues at stake are the energy source for the development (whether baroclinic, as the primary synoptic frontal cyclones are known to be, or barotropic as some studies have found), what factors favour 'explosive' growth, the role of moist processes (in conditioning the primary front and in influencing the secondary system) and the structure of the mature frontal wave.

Wave development on extended fronts is a common feature of daily weather charts but not all of these waves develop into mature cyclones. Some factors that make forecasting frontal waves difficult are their small scales (comparable with the resolution of numerical weather prediction models), their rapid growth rate and that their development may be sensitive to flow structures which may only inaccurately be represented in the initial observational data set.

1.2 Aims of this Study

In this thesis a study is made of the dynamics of PV elements that relate to the evolution of extratropical cyclones. This includes an identification of the key PV elements and an analysis of their relative importance, the physical processes involved in the formation of these elements, and their dynamical evolution and interaction. This is done both with highly simplified dynamical models to study the dynamics of idealised PV anomalies and with real case simulations to examine sensitivity aspects (e.g. various physical processes and individual PV elements).

In chapter 2 the conceptual framework of the PV-perspective is set out. Some of the standard descriptions of atmospheric flow phenomena as displayed in this framework are presented and an outline given of the diagnostic tools used to identify the PV elements and to study their dynamical importance. Also a brief account is given of the dynamical models used in this study.

Chapter 3 is devoted to the dynamics of idealised PV elements. The linear instability and the nonlinear evolution is studied of PV-related elongated anomalies. Such elements are often observed in the lower troposphere in connection with frontal wave developments and in the upper troposphere/lower stratosphere the development of PV streamers is a common

feature.

An analysis of a frontal wave cyclogenesis event with a numerical weather prediction model is carried out in chapter 4. Simulations are performed to study the impact of latent heat release on the rapid developing cyclone. The development of the key PV elements is compared with the idealised results.

In chapter 5 a strategy is outlined to explore the contribution of errors in the specification of tropopause-level flow features to the misforecast of individual synoptic and sub-synoptic weather systems¹. The approach entails the identification of key upper-level PV error elements at the forecast-time, their Lagrangian retrodiction back to the initial analysis-time with intermittent PV-inversion, and a forward integration starting from the revised initial state. The procedure can yield direct information on the role and strength of upper-level effects, and if the revised “forecast” verifies successfully it can indicate the nature of the analysis error and its likely source.

In chapter 6 a statistical-climatological analysis of the PV error as defined in chapter 5 is undertaken. Such an investigation can point on the regions where there is need for an improved observational data set. This analysis is performed for the northern Atlantic sector for the year 1993.

¹This part corresponds to a paper with the title ‘Misforecasts of Synoptic Systems: Diagnosis via PV-Retrodiction’ (Fehlmann and Davies 1997).

Chapter 2

Basic Notions and Tools

The atmospheric structures of interest in the present thesis are considered from the potential vorticity standpoint. The objectives are to introduce the basic notion that will be needed, and the diagnostic tools that will be used, in the subsequent chapters. In section 2.1 the concept of potential vorticity is introduced and an account given of its fundamental properties. In section 2.2 a description is provided of the dynamical setting adopted for the idealised studies, and the data set and the numerical model used herein for the case studies. Finally in section 2.3 a description is provided of the tools to analyse the source and physical processes involved in the formation of PV structures, and to analyse the potential of the contribution to the dynamics of these structures.

2.1 The Concept of Potential Vorticity

A dynamically-based view of synoptic and sub-synoptic scale atmospheric flow phenomena is provided by the potential vorticity perspective. It stems from to the work of Rossby (1940) and Ertel (1942) who deduced that PV (for a mathematical definition see equation (2.1)) is a conserved quantity in the frictionless and adiabatic limit. The idea of diagnosing in the balanced-flow limit the flow structure from the spatial distribution of the PV – the so-called PV-invertibility principle – was first stated in a rudimentary form by Kleinschmidt (1950). In a case study he observed that a surface cyclone over the Baltic was accompanied by a ‘Zyklonenkörper’, i.e. a body of high PV values near the tropopause. He claimed that the development of the upper-level PV was independent of the surface cyclone but had influenced the low-level development.

The mean climatological PV distribution based on ten year ECMWF analysis fields is displayed in Fig. 2.1. The zonal mean (panel b) shows that due to the increase of the static stability in the stratosphere the PV distribution transits from ~ 0.5 pvu¹ in the troposphere to much higher values in the stratosphere. The 2 pvu surfaces lies in the transition zone between the more highly stably stratified stratosphere and the troposphere. This together with the conservation of PV on an isentrope in the adiabatic limit has prompted the definition of the 2 pvu iso-surface as the dynamical tropopause. On a 320 K isentropic surface the PV

¹The potential vorticity units are defined as $1 \text{ pvu} = 10^{-6} \text{ K m}^2 \text{ kg}^{-1} \text{ s}^{-1}$.

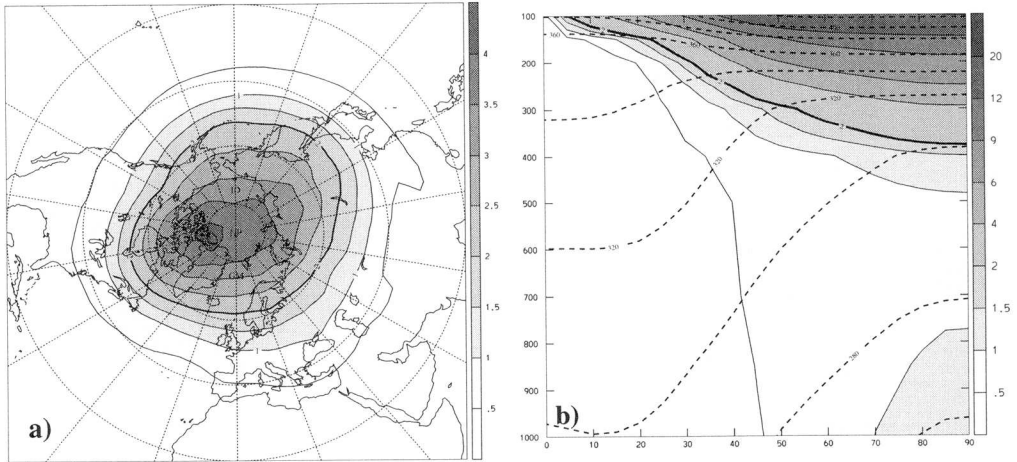


FIG. 2.1: Climatological distribution of the potential vorticity as calculated from ECMWF ten year mean fields (Hoskins et al. 1989). Panel (a) shows on the 320 K isentropic surface (contour interval 0.5 pvu, 2 pvu contour bold), and panel (b) the zonal mean potential vorticity (shaded, 2 pvu contour bold). In panel (b) the zonal mean potential temperature (dashed lines, contour interval 20 K) is overlaid.

distribution shows (panel a) higher values towards the pole, because of the contribution of the Earth rotation to the absolute vorticity. Deviations away from the climatological distribution can be linked to the PV patterns accompanying the development of specific weather systems.

These key PV elements can be major undulations and streamers of potential vorticity in the upper-troposphere lower-stratosphere, elongated pre-frontal anomalies of enhanced PV, coherent structures of high PV values in the vicinity of cyclones (PV-towers), and fronts (as boundary elements). Fig. 2.2 displays two typical PV distributions in the lower troposphere (panel a), and near the tropopause (panel b). These depictions indicate several anomalies: – (i) an elongated low-level PV-band co-aligned with a surface front (**A**) or (**B**) and (ii) in the upper troposphere a PV streamer (**C**), a cut-off structure (**D**), a tropospheric incursion (**E**), or a synoptic-scale trough (**F**). Dynamically such anomalies are linked with the evolution of fronts, cyclones and anti-cyclones. Note in this specific example the vertical coherency of the trough (**F**) with the surface frontal system (**A**), and the cut-off (**D**) with the frontal system at the eastern seaboard of North-America.

Several objective definitions for PV anomalies have been proposed. One method involves temporal filtering of the data, typically into a time-mean or a slowly varying background field and a perturbation field (Davis and Emanuel 1991). The resulting perturbation on the background field can then be further partitioned into distinct elements of dynamical importance. In this thesis piecewise inversions of anomalies will be performed. To define these anomalies we adopt a more pragmatic approach, e.g. in chapter 4 a subjective identification of elements with anomalous PV values will be applied.

In a seminal article Hoskins et al. (1985) set out the properties of the PV perspective –

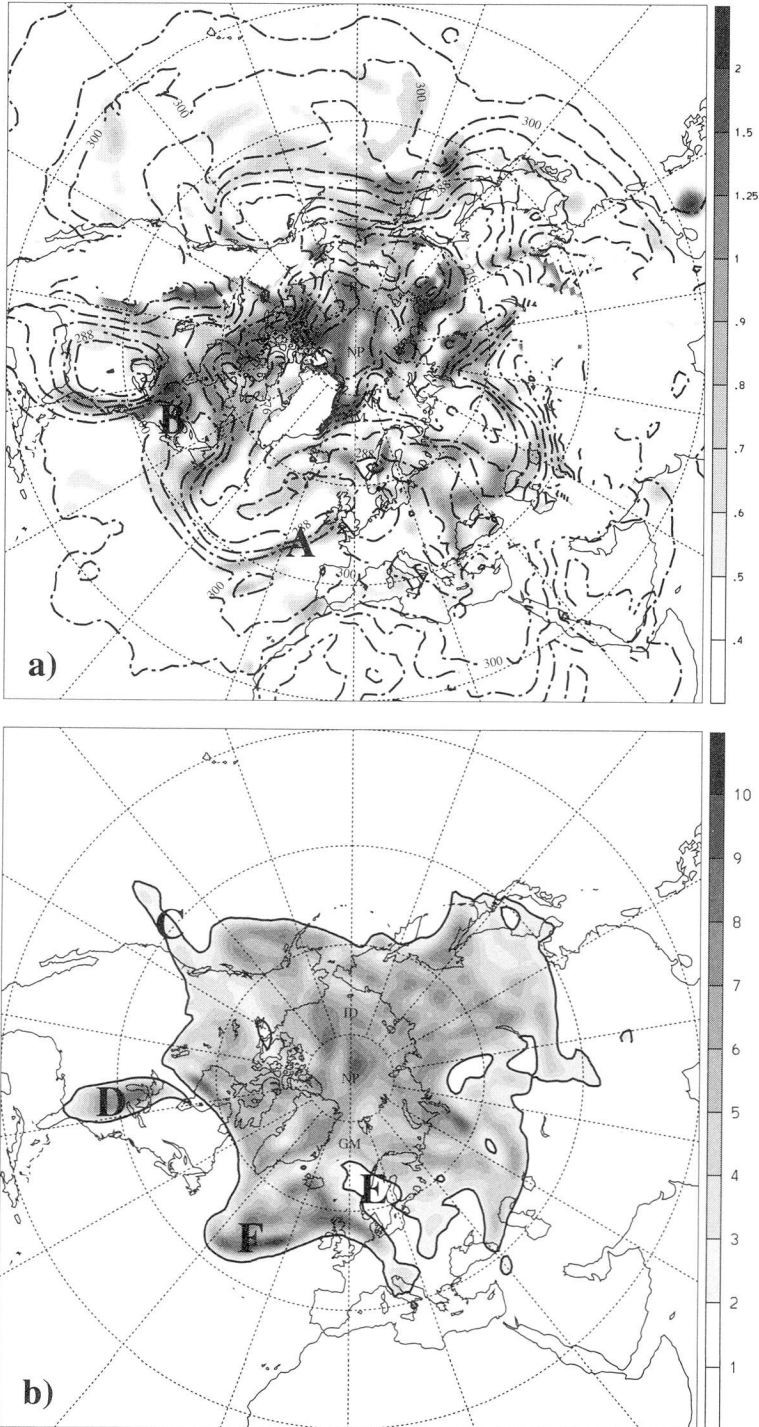


FIG. 2.2: Typical maps of the potential vorticity on the 850 hPa (panel a) and the 320 K (panel b) surface of the Northern hemisphere for 18 UTC on 20 October 1989. Displayed fields are on panel a) PV, shaded, spacing as indicated, and potential temperature, dash-dotted lines, spacing 4 K, and on panel b) PV shaded, spacing 1 pvu, PV=2 pvu is indicated by a solid line.

PV-conservation, PV-inversion and the principle of PV-partition of the flow in terms of coherent and distinct elements. A short description of these properties follows:

(i) *The conservation property* in its full form was first stated by Ertel (1942). He showed that the quantity

$$Q = \frac{1}{\rho} \boldsymbol{\omega} \cdot \nabla \theta, \quad (2.1)$$

is conserved along a trajectory of an air parcel for an adiabatic and frictionless flow, where ρ , $\boldsymbol{\omega}$, and θ stand for the density, the three dimensional absolute vorticity $f\mathbf{k} + \nabla \times \mathbf{u}$ and the potential temperature. In what follows we adopt the hydrostatic assumption

$$dp = -g\rho dz,$$

and in this limit the potential vorticity reduces to the form

$$Q = -g\boldsymbol{\omega}_p \cdot \nabla_p \theta. \quad (2.2)$$

This approximation has been denoted as Ertel's potential vorticity. The subscript p in equation (2.2) indicates that the pressure is used as the vertical coordinate (and this will be omitted hereafter).

The temporal evolution of PV can be expressed in a flux form (Haynes and McIntyre 1987)

$$\frac{\partial Q}{\partial t} = \nabla \cdot (-Q\mathbf{u} + g\dot{\theta}\boldsymbol{\omega} + g\mathbf{F} \times \nabla \theta). \quad (2.3)$$

This relationship states that the local change of PV is generated by the advection of PV with the wind field $\mathbf{u}=(u, v, \omega)$, diabatic heating $\dot{\theta}$ and frictional force \mathbf{F} including effects of turbulence (Shapiro 1976) or dissipation (Schär and Smith 1993) (note that this expression is again in a pressure coordinate system).

In the present study we focus on the contribution to the potential vorticity production rate of diabatic heating. In general this is comparatively small in the stratosphere but can be large in the tropospheric environment of extratropical cyclones.

(ii) *A partition of the flow* into PV anomalies enables atmospheric flow phenomena such as cyclogenesis and quasi-geostrophic instabilities to be related to the self-development and strong interaction of key PV-elements.

(iii) *The invertibility principle* refers to the diagnostic deduction of the flow structure given the PV distribution in the interior domain and appropriate boundary conditions (the potential temperature at the horizontal and the tangential wind-components at the lateral boundaries of the domain). For application this principle requires a specification of some kind of balance condition and a specification of the reference state. In the present study the working assumption is made of a quasi-geostrophic balanced atmosphere, i.e. pressure gradient and Coriolis force are, to a first approximation, in a state of balance². In principle the assumption holds only for flow structures with small Rossby numbers, but it will be

²In fact the inversion technique which will be used in this study on real data sets, goes beyond the quasi-geostrophic assumption. Quasi-geostrophic inversion will be applied iteratively on PV perturbations – a piecewise potential inversion – and after each iteration a nonlinear normal-mode initialisation will be applied on the resulting fields.

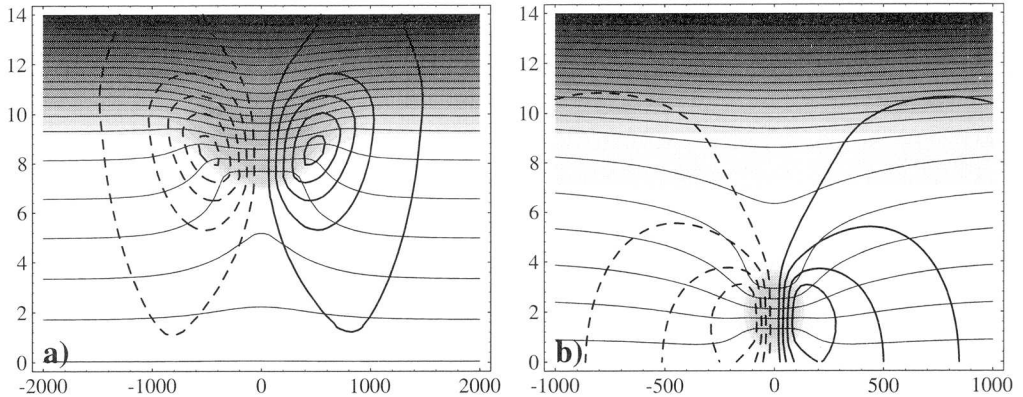


FIG. 2.3: Inversed flow structure of an upper-level PV intrusion (panel a) and a low-level PV band (panel b). Shown is PV, shaded, potential temperature, thin lines, and across wind fields, thick lines.

shown that, in practice, this balance condition gives a reasonably accurate inversion even for sub-synoptic phenomena.

To illustrate the flow structure associated with related PV anomalies Fig. 2.3 shows the flow associated with (panel a) a circular upper-level PV anomaly, and (panel b) the flow linked to a low-level PV band. The positive PV anomaly near the tropopause is associated with a warm (cold) thermal anomaly located above (below) the PV anomaly. In effect the static stability of the atmosphere is reduced beneath the anomaly. The cyclonic wind field also has a distinct signal at the surface.

The low-level PV band induces a cyclonic shear line in the troposphere. The inverted flow structures of both the upper-level and low-level anomalies give an estimate of the far field influence of the anomalies and determine therefore the region where interaction with other PV elements can occur. Furthermore the inversion of these PV anomalies gives, via the reduction of the static stability, an indication of where condensation is more likely to occur.

The invertibility can be formulated as an electrostatic analogy. In particular for quasi-geostrophic PV (Bishop and Thorpe 1994c) and Ertel's PV (Thorpe and Bishop 1995) this analogy states that the PV can be expressed as the divergence of a vector field. This vector field corresponds to the electric displacement field in a dielectric medium. The quasi-geostrophic PV can be approximated as

$$e_f = f_0 \rho \frac{Q - \bar{Q}}{\rho_0 Q_0} \quad (2.4)$$

where Q , \bar{Q} and Q_0 are, respectively, Ertel's PV, Ertel's PV of a balanced basic state depending only on the latitude and the height and Ertel's PV of an only vertically depending reference state. The weighted deviation of the zonal mean e_f plays the role of the free charges. In effect equation (2.4) states that it is the relative amplitude of an anomaly which defines the total charge and therefore the strength of a PV anomaly. The strength of such an anomaly,

expressed by the free charge e_f , depends, as indicated above, on the relative deviation of the potential vorticity from a zonal reference value.

As an example of this PV-concept Fig. 2.4 demonstrates following Hoskins et al. (1985) the interaction mechanism of an upper-level anomaly with the surface baroclinicity. The velocity field of the upper-level anomaly is such that the warm air is advected to the north and induces a stronger warm surface anomaly. Moreover, by the invertibility principle, the latter is associated with a cyclonic wind field which can serve to advect the upper-level anomaly further south. The latter implies, in turn from (2.4) and the climatological distribution (Fig. 2.1), a stronger PV charge e_f of the upper-level anomaly. This interaction mechanism between upper- and low-level structures has been linked to, and viewed as the prototype of a type B development.

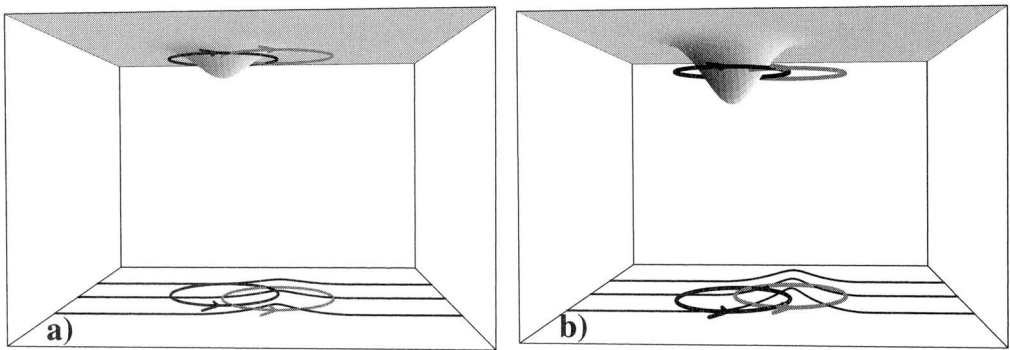


FIG. 2.4: Sketch of cyclogenesis associated with the interaction of an upper-level PV anomaly and a low-level baroclinic region according to Hoskins et al. (1985). In (a) an upper-level PV anomaly, indicated by an intrusion of high PV stratospheric air into the troposphere, and associated with a cyclonic wind field, is inducing on the pre-existing surface baroclinicity a temperature anomaly, which itself induces a cyclonic wind field. This wind field advects the upper-level anomaly further south and amplifies it thereby (b) which in turn induces a stronger surface temperature anomaly.

2.2 Models and Data Set

Recent progress in the understanding of atmospheric flow phenomena is strongly influenced by the development of more refined idealised numerical models and more realistic numerical weather prediction models. Simulations with idealised numerical models can provide insight on the dynamics of extratropical cyclones. These dynamical models are often operated in simple settings and with elementary physical processes. Two approaches adopted for these models are the normal mode and singular vector techniques. Baroclinic instabilities and frontal wave development have been studied where one gained insight within the quasi-geostrophic, semi-geostrophic or primitive equation framework, and have yielded a qualitative description of the development and served to test various ‘conceptual models’.

Numerical weather prediction models on the other hand, enable detailed case studies to be performed of observed events. Such studies can reveal the usefulness and the deficiencies of the more idealised models. The combination of both, together with suitable diagnostic tools, can illuminate different aspects of synoptic and sub-synoptic weather systems.

2.2.1 The Quasi-Geostrophic Model

The quasi-geostrophic set of equations in the Boussinesq approximation is adopted to study the flow of an incompressible inviscid fluid on an f -plane which is vertically stratified with a uniform Brunt-Väisälä frequency, N . The Boussinesq reference state defined by the density ρ_0 , the pressure p_0 , and the potential temperature θ_0 can be obtained by an integration of a combination of the hydrostatic assumption, the ideal gas law and the definition of the potential temperature, see appendix A. Here the assumption is made of a semi-infinite atmosphere. The basic non-dimensionalised equations are

$$\left. \begin{aligned} \frac{D_g q}{Dt} &= 0 \\ \frac{D_g \Theta}{Dt} + (\widetilde{\text{Ro}})^{-1} w &= 0 \\ q &= \Delta \psi \\ \Theta &= \frac{\partial \psi}{\partial z} \end{aligned} \right\}. \quad (2.5)$$

$\frac{D_g}{Dt} = \frac{\partial}{\partial t} + u_g \frac{\partial}{\partial x} + v_g \frac{\partial}{\partial y}$ is the advective derivative following the geostrophic flow. These equations have been non-dimensionalised using a velocity scale U and a length scale a . The Rossby number, $\widetilde{\text{Ro}} = U/(af)$, is defined in terms of the corresponding dimensional setting, see Table 2.1. The effective Rossby number of a specific flow structure depends on the field

Horizontal scale	a
Vertical scale	af/N
Horizontal velocity scale	U
Vertical velocity scale	fU/N
Time scale	a/U
Temperature scale	$UN\theta_0(z)/g$
Pressure scale	$afU\rho_0(z)$

TABLE 2.1: Dimensional scales of the quasi-geostrophic system as expressed in (2.5). Note that the temperature and the pressure scale depend on the height through the Boussinesq reference state.

values (see below). We make the convention of an x - and y -axis pointing respectively in the south (warm) and east (zonal) direction. Lateral boundary conditions are $\partial_x \psi' = 0$ and $\partial_y \psi' = 0$ with $\psi' = \psi - \frac{1}{2} \Lambda x^2$, i.e. the limitation to a flow with vanishing velocities at infinity is made, except for a flow component due to a horizontal barotropic shear along the W-E orientation. Equation (2.5) is a Poisson equation for q with Neumann boundary conditions

and specifies the streamfunction ψ and the predictive components are the time evolution of q in the interior and Θ at the surface where $w = 0$. Here q denotes the quasi-geostrophic potential vorticity, ψ and Θ are the scaled deviations of the Boussinesq reference pressure and the potential temperature, f the Coriolis parameter and g the gravitational constant.

For numerical solutions of equation (2.5) we confine our-self to the case of a uniform quasi-geostrophic PV, given by the barotropic shear component, i.e. $q = \Lambda$. The same numerical model as in Schär and Davies (1990) has been used. By a spectral decomposition of the potential temperature anomaly at the surface the solution of the (in the case of a constant q.g. PV) Laplace equation for ψ' is straightforward. The thermal tendency is computed using

$$\frac{D_s \Theta}{Dt} = 0 \quad \text{at } z = 0 \quad (2.6)$$

where a leapfrog step in combination with an Asselin filter is used.

2.2.2 ECMWF Data

The operational global model of the European Center for Medium-Range Weather Forecasts (ECMWF) is a state-of-the-art model for numerical weather prediction. The current version³ T213/L31 of the model utilises the hydrostatic primitive equations and has sophisticated parametrisation schemes for relevant physical processes including cloud development, precipitation, radiation, gravity wave drag, turbulence and diffusion, and planetary boundary layer and surface effects (Simmons 1991, Hortal 1991). For use in this thesis the data are interpolated on the rotated grid of the Europa Modell (EM) with a grid spacing of 0.5° (see below).

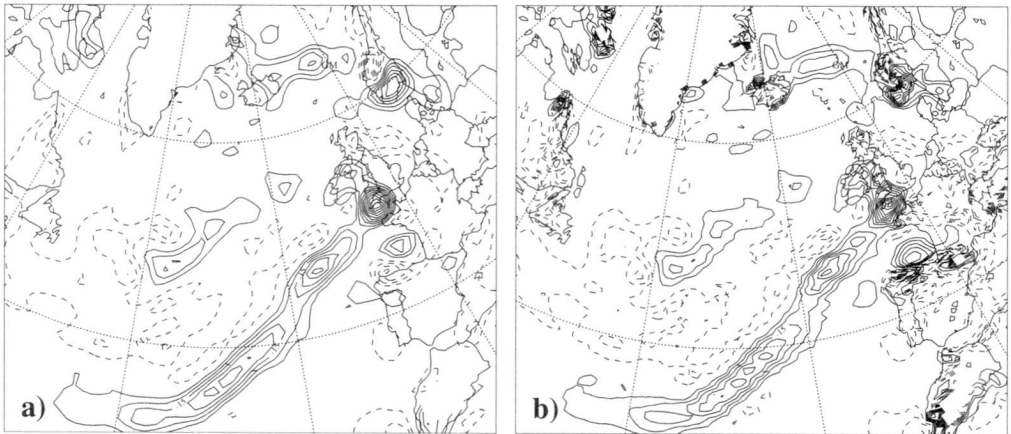


FIG. 2.5: Vertical velocity-field (spacing 5 hPa h^{-1}) from the initialised analysis data of the ECMWF (panel a) and diagnostically deduced ω -field by the EM (panel b).

³Before the 17 September 1991 the model version T106/L19 was in operation, i.e. for the case studies before this date the initialised analysis fields with a resolution of about 150 km in midlatitudes have been used.

The data assimilation-initialisation-forecast cycle incorporates observational data from various operational sources (surface stations, radiosondes, balloon and satellite soundings, commercial aircraft and drifting buoys) and produces initialised analysis fields at 00, 06, 12 and 18 UTC. It is the latter fields that are used as the analysis fields/the observational data base for this study.

The vertical velocity field ω is a diagnostic variable of the so called Europa Modell (EM), the limited area numerical weather prediction model of the German Weather Service, see below. For the trajectory calculations and the diabatic heating rates the ω -field of the EM will be used. In Fig. 2.5 the velocity field from the ECMWF, which is available with the initialised analysis, is compared with the diagnostically deduced ω -field of the EM for one specific case. It illustrates that the diagnostically deduced vertical velocity field of the EM is over the ocean comparable with that of the ECMWF. Differences in the ω -field over land are due to the different representation of the orography in the two models.

2.2.3 The Europa-Modell

In the present study real case simulations are performed with the EM, the operational weather prediction model of the German Weather Service (DWD) and the Swiss Meteorological Institute (SMA), developed by the DWD (Majewski 1991). It is a limited area NWP-model which operates on a rotated grid with a horizontal resolution of 0.5° (~ 56 km) and is based on the hydrostatic set of primitive equations. Hybrid vertical coordinates are used and we operate in this study with 32 levels.

The parametrised physical processes include a surface layer formulation, a boundary layer and turbulence formulation, a soil model with two layers in the soil for the heat and water budgets as well as a snow representation scheme, grid-scale cloud microphysics of Kessler-type, moist convection, a radiative transfer formulation, and a forth-order horizontal diffusion scheme.

In our case the model is initialised by the analysis fields of the ECMWF and at the lateral boundaries relaxed in 6 h intervals on the analysis fields.

2.3 Diagnostic Tools

A range of diagnostic tools are used in this thesis to analyse the PV related structures and mechanisms. First we estimate the diabatic effects due to condensational heating by computing the diabatic PV rates. Second trajectory calculations are performed to analyse the diabatical generation and annihilation of PV. These trajectory calculations assume the “diffusion-free” advection of the PV. Third the application of inversion to specific PV elements is performed to (a) estimate the contribution of these elements to the dynamical evolution and (b) to generate a range of different balanced initial fields to study the influence of specific PV elements on the dynamics.

Ageostrophic flow structures play an important role in the formation of strong frontal structures. A traditional diagnostic tool to analyse this mechanism is provided by the \mathbf{Q} -vector formalism. Such a diagnosis has been applied to analyse idealised simulations in a

quasi-geostrophic, semi-geostrophic of primitive equation framework.

2.3.1 Condensational Heating

The thermodynamic variables are calculated following the empirical formulae of Bolton (1980). The condensational heating rate is diagnosed with the aid of the expression

$$\dot{\theta}_c = \frac{\theta L}{T c_p} \frac{Dq}{Dt}$$

(see Berrisford 1988) where $\frac{D}{Dt} = \partial_t + \mathbf{u} \cdot \nabla$ is the total time derivative following the trajectory of an air parcel, L denotes the latent heat of condensation of water, c_p is the heat capacity of water at constant pressure, and q is the specific humidity. Following Rossa (1995) and Wernli (1995) the assumption is made that condensation occurs where ascending air is saturated. Within these regions one can write

$$\frac{Dq}{Dt} = \frac{dq_s}{dT} \frac{DT}{Dt}$$

(q_s denotes the saturation mixing ratio). Together with the definition of θ this leads to the following approximated formula in isobaric coordinates for the diabatic material change of θ due to resolvable-scale condensation ($\kappa = R/c_p$):

$$\dot{\theta}_c = \frac{-\frac{L\kappa\theta\omega}{c_p p} \frac{dq_s}{dT}}{1 + \frac{L}{c_p} \frac{dq_s}{dT}} \cdot \begin{cases} \left(1 - \exp\left(\frac{RH_0 - RH}{5}\right)\right) & \text{if } \omega < 0 \text{ and } RH_0 \geq RH \\ 0 & \text{else} \end{cases} \quad (2.7)$$

Condensation is assumed to occur for relative humidity values larger than a threshold value RH_0 , which was chosen equal to 80%. (The latter feature seeks to account for condensation processes in a grid box even if the whole area is below saturation.) Fig. 2.6 shows how its value varies with respect to the relative humidity.

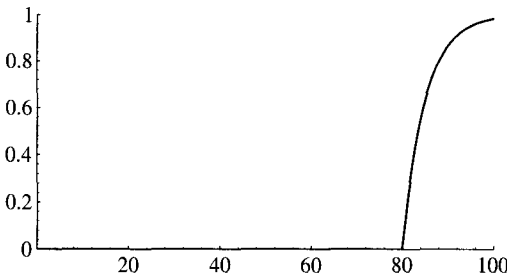


FIG. 2.6: A switch which acts to simulate sub-grid scale rain which can occur even if the whole area in a grid box is not saturated. The value is zero for relative humidities $RH < 80\%$ and 0.98 for $RH = 100\%$ (Berrisford 1988). Without this switch latent heating is much too small.

The diabatic heating rate leads then directly to an estimation of the condensationally produced PV rate due to equation (2.3):

$$\frac{DQ}{Dt} = g\omega \cdot \nabla \dot{\theta} \approx g\zeta \frac{\partial \dot{\theta}}{\partial p}, \quad (2.8)$$

where ζ denotes the vertical component of the absolute vorticity vector.

2.3.2 Lagrangian Trajectories

Three-dimensional kinematic trajectories are calculated following the method of Pettersen (1956). Details of the calculations can be found in Wernli (1995). The calculations are performed in the rotated EM-grid. The trajectory calculation consists of a forward time-step of the form $\mathbf{x}^{n+1} = \mathbf{x}^n + \mathbf{u}(\mathbf{x}^n)\Delta t$ followed by several iterations where the mean wind $\bar{\mathbf{u}} = \frac{1}{2}(\mathbf{u}(\mathbf{x}^n) + \mathbf{u}(\mathbf{x}^{n+1}))$ is used for the time-step. For application in the present study three iterations and a time-step of $\Delta t = 0.5$ h (Seibert 1993) was chosen. The interpolation of the wind fields was linear both in time and space. As a demonstration of the accuracy of this trajectory calculation method in Fig. 2.7 the upper level PV structure is compared with the 24 h forward traced PV structure of the 24 h earlier PV distribution.

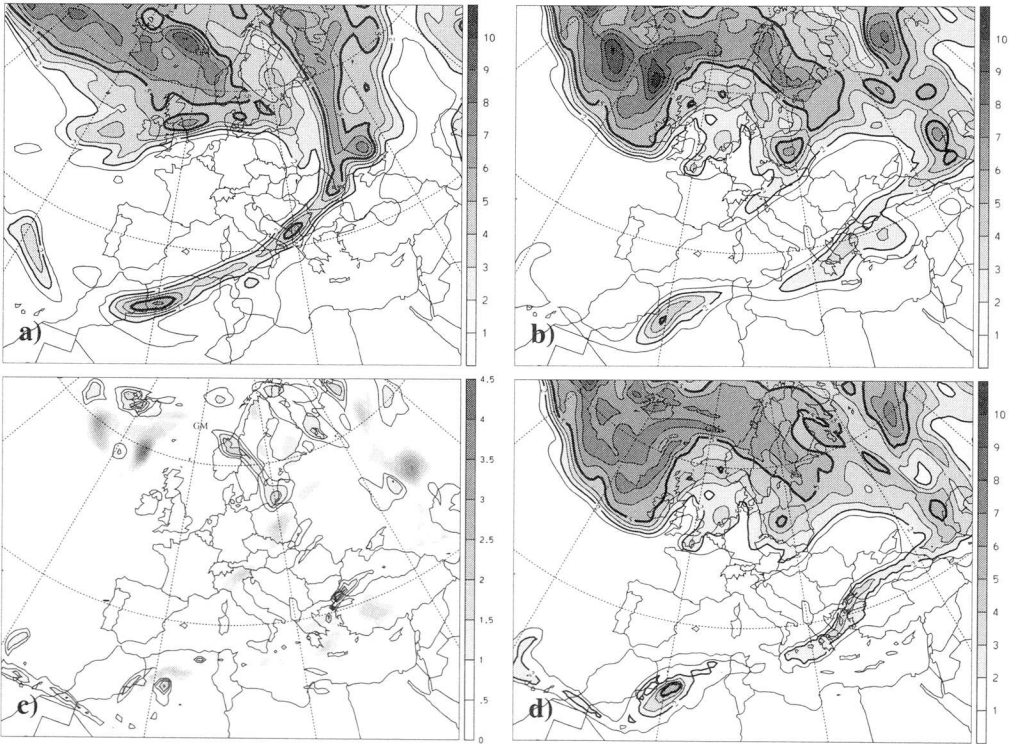


FIG. 2.7: Comparison of the analysed PV with the advected distribution on the 320 K isentropic surface. Panel a) 12 UTC 11. November 1991, panel b) 12 UTC 12. November 1991, panel d) 24 h forward advected PV distribution valid for 12 UTC 12. November 1991, panel c) absolute value of the difference between the analysed and advected PV. Weaker PV values in the analysed field than in the advected are overlaid.

This demonstrates the accuracy of the trajectory calculation and the conservation property of the PV in the upper troposphere and stratosphere (in the model formulation this property is not explicitly formulated). The result is better than could be expected because

the wind fields are available only every 6 h and are linearly interpolated in time. In particular even the detailed structures of the observed PV distribution are well represented in the advected PV field up to specific isolated positive and negative anomalies in the difference field.

Furthermore the positive and negative differences between the observed and advected PV field (in the limit where they are not caused by either the model formulation or trajectory errors) can be attributed to either inconsistencies in the time series of the initialised analysis fields or to diabatic activity e.g. due to condensational heating. PV anomalies in the difference field which are associated to higher values in the advected than in the observed PV distribution can be related to a decay of the anomaly due to diabatic heating processes in the troposphere. The other anomalies have in this limit to be considered as due to errors in the initialised analyses.

2.3.3 Potential Vorticity Inversion

In recent years several techniques to attribute the wind and mass distribution associated with some anomalies in the potential vorticity field have been proposed and studied based on different balance conditions, such as quasi-geostrophic, semi-geostrophic, gradient wind, or some nonlinear balance (Charney 1955). These techniques have been applied to idealised configurations and to real cases (e.g. Thorpe 1986, Davis and Emanuel 1991, Davis 1992, Hakim et al. 1996).

Here we adopt a linearisation of the PV and a linear balance condition. Advantages are that the attribution problem has then a unique solution, i.e. for a given PV anomaly the corresponding wind- and mass-fields are uniquely defined.

The inversion of the potential vorticity is performed by (i) a specification of the reference state through the static stability N_0^2 of the reference state, and (ii) by an inversion of the PV in the quasi-geostrophic limit. In this limit the streamfunction is related to the q.g. PV in the interior and the boundary values by:

$$q = \frac{\partial^2 \psi}{\partial x^2} + \frac{\partial^2 \psi}{\partial y^2} + \frac{f^2}{\rho_0} \frac{\partial}{\partial z} \left(\frac{\rho_0}{N_0^2} \frac{\partial \psi}{\partial z} \right) \quad (2.9)$$

$$\left. \begin{aligned} \frac{\theta^*}{\theta_0} &= f \frac{\partial \psi}{\partial z} \\ u &= -\frac{\partial \psi}{\partial y} \\ v &= \frac{\partial \psi}{\partial x} \end{aligned} \right\} \quad (2.10)$$

The relative quasi-geostrophic potential vorticity is related to Ertel's PV in a first approximation by

$$q \approx \frac{\rho_0 g}{\theta_0 N_0^2} Q - f. \quad (2.11)$$

Higher orders are obtained as follows, by an iteration of an inversion of the residual PV distribution: Let \tilde{u} , \tilde{v} , \tilde{p} , and \tilde{T} be wind-fields, pressure, and temperature obtained by an

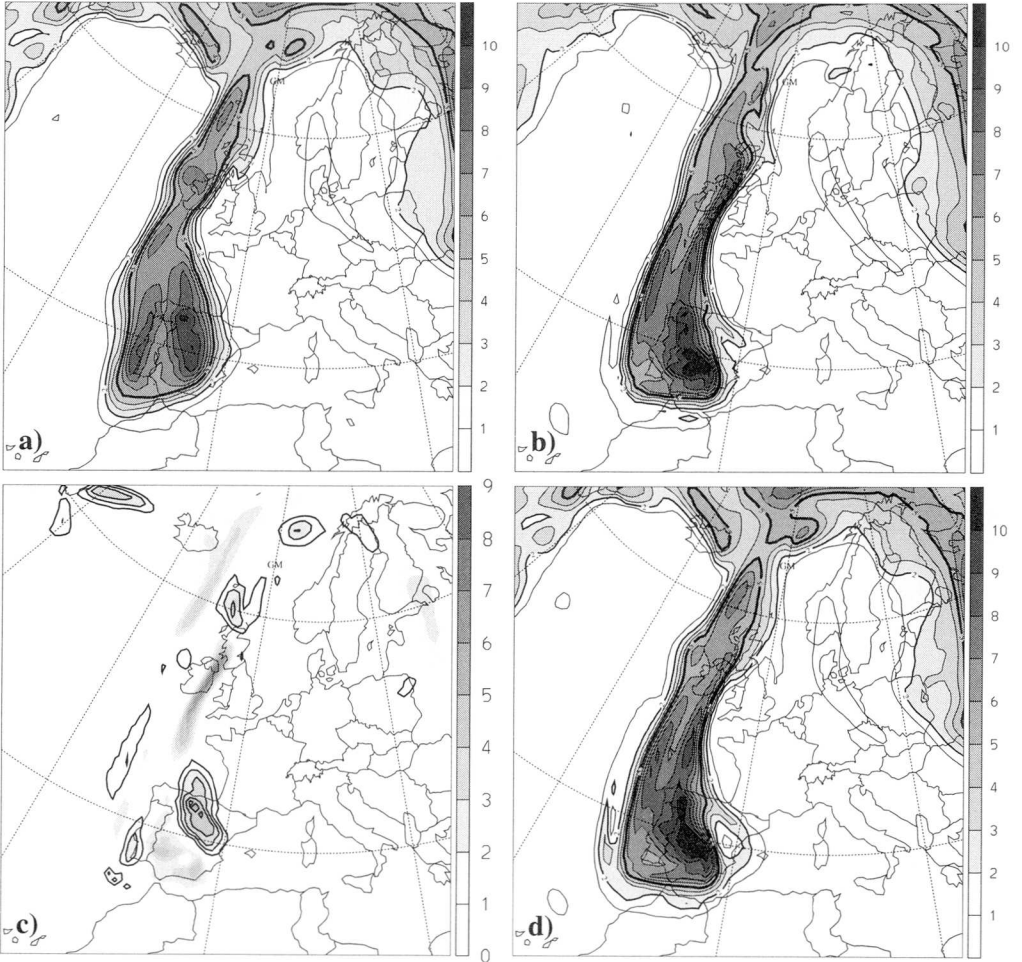


FIG. 2.8: Potential vorticity inversion of a real data PV distribution. Panel a) original PV field, panel b) modified PV distribution, panel c) difference between these two structures which gives the field to be inverted. Panel d) PV distribution of the inverted flow field.

inversion of the approximation q in (2.11), with \tilde{Q} the corresponding PV and Q the PV-field to be inverted ($|\delta Q|/Q \ll 1$ where $\delta Q = Q - \tilde{Q}$). Then to first order $\delta u, \delta v \dots$ ($u = \tilde{u} + \delta u$, $v = \tilde{v} + \delta v, \dots$) are given by an inversion of

$$\delta q \approx \frac{\rho_0 g}{\theta_0 N_0^2} \delta Q.$$

This procedure is applied to idealised PV configurations and to real case data. In the latter case after each inversion step a nonlinear normal mode initialisation of the EM is made. Fig. 2.8 shows the PV-field of a real data inversion after three iterations. For details

of the inversion formulation and the numerical techniques see appendix A.

Note that this method of relating the quasi-geostrophic potential vorticity to the Ertel PV makes use of the electrostatic analogy of Ertel's PV. Let Q_0 be Ertel's PV of an atmosphere at rest. We have

$$Q_0 = \frac{f}{\rho_0} \frac{\partial \theta_0}{\partial z} = \frac{f \theta_0 N_0^2}{\rho_0 g}$$

and the quasi-geostrophic PV of equation (2.11) can be expressed as

$$q = f \frac{Q - Q_0}{Q_0},$$

and deviations of a basic PV distribution can be expressed as a quasi-geostrophic PV by

$$\delta q = f \frac{Q - \tilde{Q}}{Q_0}.$$

2.3.4 \mathbf{Q} -vector diagnostics

A quasi-geostrophic \mathbf{Q} -vector will be applied to diagnose features of the primitive equation simulations. Furthermore we do not take into account the diabatic contribution to the frontogenesis, i.e. our \mathbf{Q} -vectors (or forcing function) include only the dynamical contribution to frontogenesis. The surface baroclinicity expressed by the thermal gradient $\nabla_h \theta$, the vertical vorticity, and the vertical velocity w are related through⁴

$$\left. \begin{aligned} \frac{D_g}{Dt}(\nabla_h \theta) &= \mathbf{Q} \quad (\text{for } z = 0) \\ \frac{D_g}{Dt} \zeta &= (\widetilde{\text{Ro}})^{-1} \partial_z w \\ (\widetilde{\text{Ro}})^{-1} \Delta w &= 2 \nabla_h \cdot \mathbf{Q} \end{aligned} \right\}. \quad (2.12)$$

Here, \mathbf{Q} denotes the quasi-geostrophic \mathbf{Q} -vector (Hoskins et al. 1978), i.e.

$$\mathbf{Q} = - \begin{pmatrix} \partial_x u_y \partial_x \theta + \partial_x v_y \partial_y \theta \\ \partial_y u_y \partial_x \theta + \partial_y v_y \partial_y \theta \end{pmatrix}. \quad (2.13)$$

The \mathbf{Q} -vector links the ageostrophic and quasi-geostrophic flow fields. Frontogenesis and frontolysis due to a deformation field can be measured by the frontogenesis function (Petterssen 1936, Miller 1948, Keyser et al. 1988).

$$\frac{D_g}{Dt}(\nabla_h \theta)^2 = 2 \mathbf{Q} \cdot \nabla_h \theta. \quad (2.14)$$

Apparent from the definition of the \mathbf{Q} -vector one can introduce a tensor-field Q which describes the locally linear mapping between the \mathbf{Q} -vector and the horizontal gradient of

⁴The equations are expressed in the same non-dimensional system as equations (2.5).

the potential temperature (Schär and Wernli 1993). This tensor is only dependent on the kinematic properties of the flow field and takes the form

$$Q_g = - \begin{pmatrix} \partial_x u_g & \partial_x v_g \\ \partial_y u_g & \partial_y v_g \end{pmatrix}. \quad (2.15)$$

In general the kinematic tensor Q can be decomposed into the parts representing the diver-

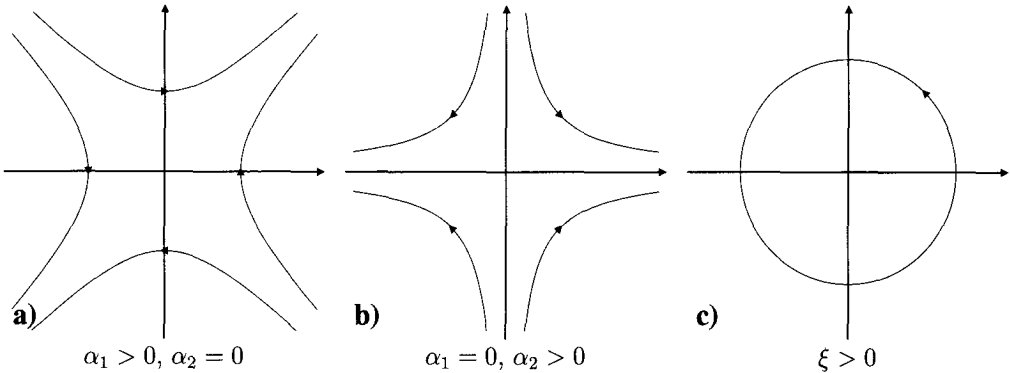


FIG. 2.9: The flow structure of a pure deformation (panel a and b) and of a pure rotation (panel c). Note that in the coordinate system where the deformation matrix is diagonal with positive entry in the first column ($\alpha_1 > 0$, $\alpha_2 = 0$) the deformation axis is the x -axis, the dilatation the y -axis.

gence, the deformation and the rotation of the flow. With this tensor-field the frontogenesis function can be expressed as

$$\frac{D_g}{Dt} (\nabla_h \Theta)^2 = 2 \nabla_h \Theta \cdot Q_g \nabla_h \Theta. \quad (2.16)$$

For the quasi-geostrophic component the divergence part vanishes such that we have

$$Q_g = -\frac{1}{2} \begin{pmatrix} \alpha_2 & \alpha_1 \\ \alpha_1 & -\alpha_2 \end{pmatrix} + \frac{\xi}{2} \begin{pmatrix} 0 & -1 \\ 1 & 0 \end{pmatrix} = Q_g^{def} + Q_g^{rot}. \quad (2.17)$$

The Q_g^{def} component is traceless symmetric and therefore there exists *locally* a *rotated* coordinate system such that the deformation tensor reads

$$Q_g^{def} = -\frac{1}{2} \begin{pmatrix} \alpha & 0 \\ 0 & -\alpha \end{pmatrix} \quad (2.18)$$

with $\alpha = \sqrt{\alpha_1^2 + \alpha_2^2}$ the strength of the deformation. The eigenvector belonging to the positive eigenvalue $\alpha/2$ points in the direction of the deformation axis. Streamfunctions of prototypes of a purely deformation or purely rotation flow field are:

$$\psi_{def} = \frac{\alpha_1}{4} (x^2 - y^2) - \frac{\alpha_2}{2} xy \quad \text{and} \quad \psi_{rot} = \frac{\xi}{4} (x^2 + y^2). \quad (2.19)$$

The associated flow structures of these prototypes are portrayed in Fig. 2.9

The rotation part of the Q -matrix does not affect the strength of the baroclinicity, but only its direction. However deformation increases the baroclinicity $\nabla_h \Theta$ parallel to the deformation axis. This axis is given by the eigenvector \mathbf{e}_+ belonging to the positive eigenvalue $\alpha/2$ of Q_g^{def} and can be expressed as

$$\mathbf{e}_+ = \alpha \sqrt{\frac{1}{1 + \frac{\alpha_1}{\alpha_2 + \alpha}}} \begin{pmatrix} -\frac{\alpha_1}{\alpha_2 + \alpha} \\ 1 \end{pmatrix} \quad (2.20)$$

The length of \mathbf{e}_+ has been chosen equal to the strength of the deformation. Frontogenetic forcing is strongest where the deformation value is large and the vector \mathbf{e}_+ parallels the horizontal thermal gradient.

Chapter 3

Idealised Studies

3.1 Introduction

From a potential vorticity perspective an atmospheric *state* can be viewed as an assemblage of distinct PV anomalies, and the associated atmospheric *dynamics* can be viewed in terms of the evolution and interaction of these anomalies. In this chapter, a limited study is undertaken of the self-dynamics of isolated PV structures and their interaction with the ambient flow. These structures are related to either surface or upper tropospheric shear lines.

In the lower troposphere shear lines appear in connection with pre-frontal anomalous PV bands and are an integral feature of frontal synoptic systems. Bands of enhanced PV values (or of enhanced surface temperature values¹) have been linked to the development of frontal-waves. Such anomalies can be generated by strong diabatic processes during frontogenesis which in turn are linked to ageostrophic motion, see e.g. Thorpe and Emanuel (1985). Typically pre-frontal PV anomalies have a width of ~ 250 km, a length of ~ 1500 km, and are confined between about 950 and 450 hPa.

It can be inferred using general stability criteria (Charney and Stern 1962) that such PV anomalies are the possible seat of dynamical instability. The instability of such shear lines has been studied in terms of internal potential vorticity (Joly and Thorpe 1990a, Joly and Thorpe 1990b, Malardel et al. 1993) or in terms of surface temperature anomalies (Schär and Davies 1990, Joly 1995). Note in passing that: – (i) the latter author adopted a non-modal approach based on the adjoint method and this can yield solutions with a growth rate faster than that of normal modes, and (ii) chapter 4 is devoted to a case study of a frontal wave development that contained such a PV structure.

In the stratosphere elongated PV structures on isentropic surfaces occur frequently as a result of extraction from the high PV reservoir of the polar stratosphere to lower latitudes in an erosion process along the surf zone of the stratospheric polar vortex. Likewise anomalies of high PV values in the upper troposphere can be interpreted as intrusions of stratospheric air. Initially the latter anomalies can have a width of ~ 400 km and a length of ~ 1000 km. In their further development deformation and stretching can alter these scales to less than 100 km width and more than 2500 km length. Appenzeller and Davies (1992) demonstrated

¹Surface temperature anomalies can also be considered as infinitesimal PV anomalies (Bretherton 1966).

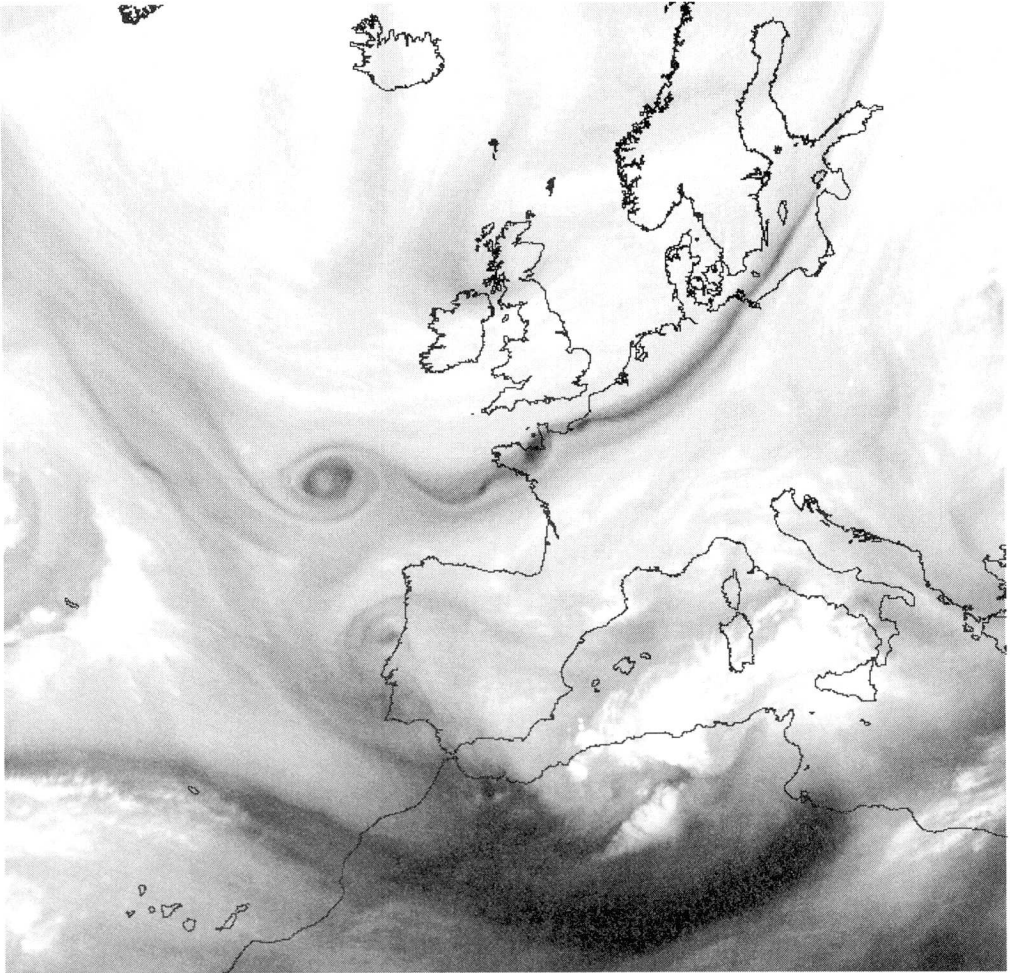


FIG. 3.1: Water vapour imagery for 06 UTC on April 29 1996.

that anomalous dry strips in the water vapour (WV) satellite images are associated with anomalous high PV anomalies near the tropopause.

Satellite images (or isentropic PV charts) show strips of dry air (or high PV values) that can break-off and roll-up (Appenzeller et al. 1996). In this breaking process a series of isolated elliptical-shaped vortices can be generated linked by thin connecting filaments that can themselves undergo a secondary instability. Fig. 3.1 shows such a vortex over the Atlantic, west of France with a streamer that extends from the Baltic Sea to the west of Brittany. This filament exhibits a further unstable development that results in three smaller scale vortices.

The larger scaled positive upper-level PV anomalies can interact with the low-level struc-

tures and can therefore have a significant impact on the dynamics and weather at lower levels. The smaller-scale structures are also important. The irreversible nonlinear evolution of these anomalies leads to a mixing of the stratospheric high PV air with the tropospheric low PV air (see, e.g., Holton et al. 1995 and references therein).

In recent years highly idealised model studies have been undertaken of tropospheric or tropopause level shear lines. Thereby some dynamical aspects can be examined which are beyond the resolution of operational NWP models. Here we compare aspects of surface QG dynamics with the PE dynamics of interior PV anomalies to form a bridge to these earlier studies.

The PV and θ -bands are studied in highly idealised settings. For example the ambient flow structure with which the anomaly can interact will be characterised by two parameters: a uniform barotropic shear and a uniform baroclinicity. These constitute useful proxies to more real settings. For example for a pre-frontal PV or θ -anomaly the barotropic shear, whether it is cyclonic or anti-cyclonic, will be determined by the relative location of the anomaly to the mother cyclone. (If the anomaly is close to the center of the cyclone the shear will be cyclonic.) Likewise the strength of the baroclinicity can vary from case to case of frontal wave development, and it can also alter during the development due to in-situ frontogenesis.

The PV (θ) strip itself will be characterised by a shape parameter which represents the maximal PV (θ) gradient at the edge of the anomaly. In practise this parameter can also be modified during the development, e.g. cloud diabatic effects that might have generated the anomaly can further increase the gradient of the anomaly.

Juckes (1995) derived an analytical solution for the maximal growth rate and the wave length of the most unstable mode of the linear instability problem of an infinite surface θ -band with top-hat profile. He compared the instability characteristics with numerical solutions for smoothed edges. It was deduced that the strip becomes more unstable if the maximal temperature gradient at the edge of the strip is reduced and the wave-length of the most unstable mode is thereby reduced.

Dritschel (1989b) investigated the influence of adverse shear on the stability of a vorticity strip. It was shown that adverse shear stabilises a vortex strip. He introduced as well a profile parameter and noted that the growth rate is very similar for a range of different profiles.

Here a systematic analysis is undertaken of the sensitivity in parameter space of barotropic and baroclinic shear and the shape of the anomaly. We start with a discussion of two limit forms of the quasi-geostrophic framework (section 3.2). Shear lines in these two limits correspond to infinite deep or infinitesimal shallow PV anomalies and the study of the flow structure of analytical solutions should indicate the appropriateness of these two limit forms. A linear instability analysis is carried out of a surface temperature band with a special emphasis on the dependence of the growth rate on the barotropic shear, the baroclinicity, and the shape parameter (section 3.3). In section 3.4 we will also discuss the nonlinear development of these bands with a superimposed normal mode as initial state, of bands of finite length, and of elliptical structures. The rest of the chapter is devoted to the nonlinear development of internal PV anomalies in the PE framework (section 3.5).

3.2 Some Comparative Features

Several limit forms of the quasi-geostrophic framework as described by equations (2.5) have been used to study linear and nonlinear aspects of shear lines and nonlinear dynamics of elliptical vortices. One limit form is achieved by considering a semi-infinite atmosphere with uniform quasi-geostrophic potential vorticity q which represents merely a uniform barotropic background shear. In this case the mathematical formulation of the problem reduces to two dimensions. The dynamics is given by an advection with the geostrophic flow of the scalar Θ at the surface, where the temperature distribution in turn specifies the flow field. This dynamical system has been denoted as the surface quasi-geostrophic system (SQG). Another limit form is given if the streamfunction ψ is independent of the vertical coordinate. In this case the QG system reduces to the two-dimensional Euler flow equations and this system shall be denoted as the barotropic quasi-geostrophic system (BQG).

A different limit form to study tropopause dynamics has been introduced by Juckes (1994). He considered shallow intrusions of stratospheric air into the troposphere in the quasi-geostrophic limit, where the troposphere and the stratosphere have been characterised each by a constant Brunt-Väisälä frequency N_t and N_s . Here the tropopause is treated as the interface of constant low and high potential vorticity values, and anomalies are treated as negative anomalies of the tropopause altitude. Juckes showed that the resulting equations representing this tropopause dynamics are mathematically equivalent with SQG, but with a rescaled Brunt-Väisälä frequency.

A complementary view of a tropopause level cyclonic anomaly can be achieved by adopting a two-layer model, with PV anomalies located on upper tropospheric isentropes. This yields a dynamical framework that is similar to BQG (Wirth 1996).

Some comparative features of SQG and BQG dynamics follow immediately from the equations. In BQG the streamfunction induced by a point vortex at \mathbf{x}' in an unbounded two-dimensional domain is given by

$$\psi = \frac{1}{2\pi} \log(|\mathbf{x} - \mathbf{x}'|)$$

whereas in SQG the streamfunction induced by a point temperature anomaly at the surface is given by

$$\psi = -\frac{1}{2\pi} \frac{1}{|\mathbf{x} - \mathbf{x}'|}.$$

Corresponding velocities are proportional to r^{-1} for BQG and r^{-2} for SQG flow, where r is the distance from the point vortex or temperature anomaly. A consequence of the more singular nature of the Greens function of SQG is that SQG is more characterised by local interaction where in BQG anomalies can interact on larger distances. Furthermore it has been shown that for smooth initial vorticity distributions in BQG no singular vorticity gradients can be produced in finite time (Rose and Sulem 1978) where in SQG from numerical studies there is evidence of a finite-time collapse (Constantin et al. 1994).

There are other differences in the stability of shear lines in BQG and SQG. Held et al. (1995) noted that on the filaments that are produced in the nonlinear development of a strip of potential temperature a second instability on a reduced length scale by a factor of

10 – 100 may evolve which is not observed in the analogue vorticity strip. They argued that as a vorticity filament is stretched, the growth rate of secondary instabilities on this filament remains constant, since vorticity is conserved. As a result, the filament is relatively easily stabilised by large-scale shears and strains induced by remote vorticity distributions, as these need only be of the same order of magnitude as the shear induced by the filament itself (see, e.g., Dritschel 1989b). In contrast, in the SQG case, it is the potential temperature within the filament that is conserved, while the vorticity, and the growth rate of the instability, increases as the filament is stretched and thinned. Whatever environmental strain field that exists will eventually be overcome, and the second instability of the filament is inevitable. The process seems to be related to what is observed for example on the water vapour image (see again Fig. 3.1) even though here the scale reduction is only one of $\sim 3 - 5$. A caveat of such an explanation of the observed “second instability” on the satellite imagery is that the Rossby number for the second instability can become very large and SQG may no longer be applicable. In fact it has been noted that the cascade to small scales in SQG is governed by a $k^{-8/3}$ energy spectrum and the Rossby number increases as $k^{2/3}$ (Blumen 1978, Hoyer and Sadourny 1982). As a consequence SQG will in general break at some stage of the nonlinear development.

Some further indication of the appropriateness of SQG and BQG limits is sought by a comparison of solutions of idealised (top hat profile) infinite shear lines and elliptical (or ellipsoidal) vortices.

3.2.1 Analytical Solutions of Shear Lines in QG, BQG and SQG

In QG the flow structure of an elliptical infinite PV band can be solved exactly (see appendix B). Here the solution is given of an anomaly of width a and height c in an unbounded atmosphere:

$$\Delta\psi = q = \begin{cases} q_0 & \text{if } ((x/a)^2 + (z/c)^2) \leq 1 \\ 0 & \text{elsewhere.} \end{cases}$$

By the method of images one can construct, out of the above solution for ψ , the flow field of a PV band centered at z_0 with homogeneous Neumann boundary conditions at $z = 0$, i.e. with vanishing potential temperature at the surface. A deep PV band, i.e. large vertical extension c should be approximated by a vorticity band in BQG, where a shallow PV band should correspond to a θ -band in SQG. For a quantitative comparison it is necessary to comment on the relation between the amplitudes q_0 , ζ_0 and Θ_0 of the PV, vorticity, and potential temperature strip and the profiles. For an infinite deep PV strip, the potential vorticity in the strip equals the vorticity, i.e. in the limit $c \rightarrow \infty$ we have to compare the solution for $q_0 = \zeta_0$ and for a top-hat profile in the vorticity. For an infinitesimal shallow PV strip, i.e. $c \rightarrow 0$, we note that in the QG solution of the PV band the maximal amplitude of the potential temperature can be found at the upper boundary of the PV strip and is (see appendix B.2)

$$\Theta_{max} = q_0 \frac{ac}{a+c}.$$

To imitate the shallow PV band the corresponding temperature profile should be a smooth

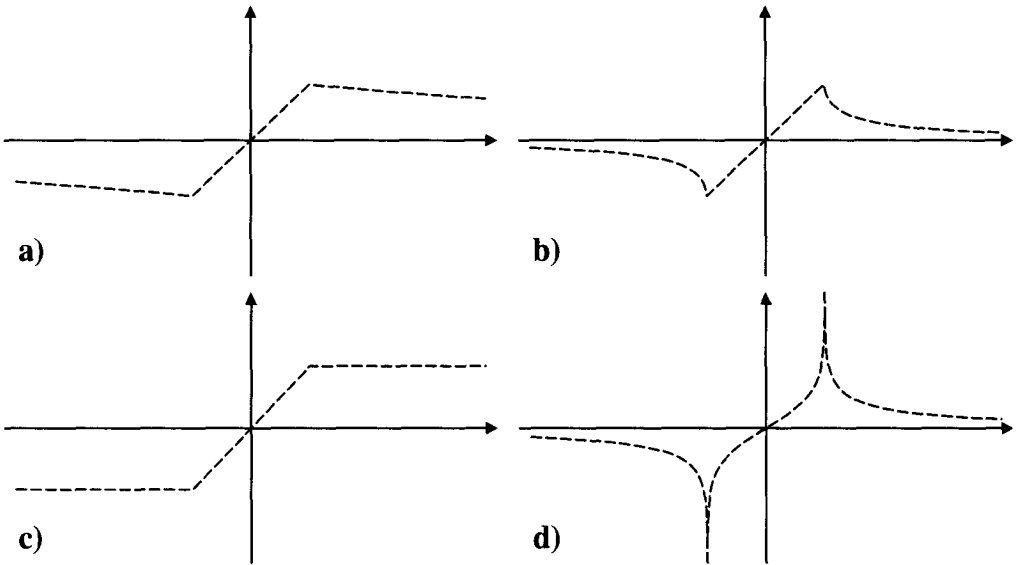


FIG. 3.2: Wind field of shear lines in QG (panel a and b), BQG (panel c), and SQG (panel d). Note that the left panels and the right panels have not the same velocity scales.

distribution. Here we compare the shallow PV band with a top-hat θ -band with an amplitude as given above.

Fig. 3.2 shows the velocity field of a deep and shallow elliptical PV band with $c = 10a$ (panel a) and $c = a/10$ (panel b) and the velocity field of a top-hat vorticity (panel c) and potential temperature band (panel d). Apart from the region where there is a discontinuity in the temperature profile the velocity field of the θ -band is very similar to that of the shallow PV strip. It indicates the appropriateness of the two limit forms of QG to study deep and shallow PV anomalies. Note the singularity in the wind field for the case of a temperature anomaly. For continuous θ -distributions, considered later in the linear instability analysis, there are no such singularities. (Note that the singularity renders contour dynamics less tractable in SQG than for BQG.)

3.2.2 Analytical Solutions of (Ellipsoidal) Elliptical Vortices in (QG), BQG and SQG

Besides analytical solutions of infinite bands there exist analytical solutions of elliptical (in BQG or SQG) or ellipsoidal (in QG) vortices.

In the case of BQG Kirchoff found in the last century that an elliptical vortex with semi-axes a and b and constant vorticity ζ_0 in the ellipse, whilst the surrounding fluid is

moving irrotationally, rotates without changing its shape with an angular velocity of²

$$\Omega = \frac{ab}{(a+b)^2} \zeta_0.$$

The rotation reaches a maximum for an ellipse that approaches a circular shape. A stability analysis shows that this vortex is stable as long as the length to width ratio is less than 3 and unstable otherwise (Love 1893).

Meacham (1992) carried out a similar analysis of a PV ellipsoid in an unbounded atmosphere. He considered a PV distribution given by

$$\Delta\psi = q = \begin{cases} q_0 & \text{if } ((x/a)^2 + (y/b)^2 + (z/c)^2) \leq 1 \\ 0 & \text{elsewhere} \end{cases}$$

He showed that such a configuration rotates around the vertical axis without changing its shape. In the limit where the vertical extension of the ellipsoid goes to infinity his solution for the angular velocity goes to the Kirchhoff result, whereas for the case of a shallow ellipsoid the angular velocity decreases.

From Meacham's solution one can produce a range of elliptical smooth surface temperature anomalies that rotate without changing their shape: Take the PV ellipsoid centered at $z_0 < -c$ (i.e. an imaginary subterranean ellipsoid). This induces an elliptical temperature anomaly at the surface which will rotate with the corresponding angular velocity of the ellipsoid. The profile for such a temperature pattern is determined by the two parameters z_0 and c .

The influence of these two parameters, z_0 and c , on the θ -profile can easily be illustrated for the infinite elliptical PV strip, i.e. in the limit where $b \rightarrow \infty$. In Fig. 3.3 temperature profiles are shown for $\{a : c = 10 : 1\}$ with $z_0 = -c$ (panel a) and for $\{a : c = 3 : 1\}$ with $z_0 = -4c$ (panel b). It serves to illustrate that profiles with both strong and with weak maximal gradients can be constructed with this method of subterranean PV anomalies, and therefore there exist elliptical θ -anomalies in SQG with strong and weak gradients that rotate without changing their shape.

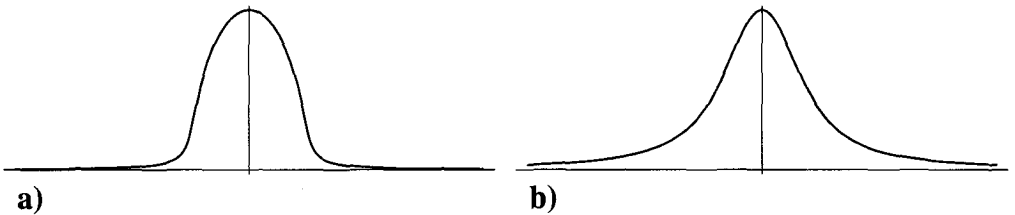


FIG. 3.3: Potential temperature distribution induced by an imaginary infinite elliptical PV strip centered under the surface at z_0 with vertical extension c . Panel a) is derived for $\{a : c = 10 : 1\}$ and $z_0 = -c$ and panel b) for $\{a : c = 3 : 1\}$ and $z_0 = -4c$.

²This solution can be derived from the streamfunction of the infinite elliptical PV band. See appendix B.3 for details.

3.3 Linear Instability

In this section we adopt the SQG framework and examine the stability of a band of enhanced potential temperature in a barotropic semi-infinite atmosphere to three-dimensional perturbations. In particular we study the influence of the ambient flow characterised by uniform barotropic and baroclinic background shear, as well as the effect of different shapes of the incipient θ -anomaly upon the nature of the instability. These different shapes are characterised by a shape parameter δ that is proportional to the slope of the temperature at the half-width location (see Appendix C for a definition and description of the temperature profiles). A linear analysis can indicate the dependence of the instability characteristics (e.g. the growth rate and wave-length of the most unstable mode) on these three parameters.

The quasi-geostrophic approximation and its limit forms hold only for small Rossby numbers. In Table 3.1 two possible dimensional settings are given, which can be linked

Setting		I	II	
Horizontal scale (km)	a	250	500	
Vertical scale (m)	af/N	2500	5000	
Horizontal velocity scale (m/s)	U	10	30	
Time scale (h)	a/U	7	4.6	
Temperature scale (K)	$UN\theta_0(z)/g$	at $z=0$ km	3.0	9.2
		at $z=10$ km	3.4	10.2
Rossby number	$U/(af)$	0.4	0.6	

TABLE 3.1: Two dimensional settings for e.g. a low-level PV band (I) and an upper level intrusion (II).

to tropospheric and tropopause level shear-lines. We have specified the settings with the characteristic scales of 250 km width and 10 m s^{-1} velocity associated with low-level PV anomalies, and by 500 km width and 30 m s^{-1} velocity associated with upper-level PV anomalies. Furthermore we have chosen the following characteristic midlatitude values: $f = 10^{-4} \text{ s}^{-1}$, $N = 10^{-2} \text{ s}^{-1}$, $g = 9.8 \text{ m s}^{-2}$, and $\Theta_0 = 300 \text{ K}$.

3.3.1 Basic State

The configuration of the two-dimensional thermal transition at the ground for four different values of a shape-parameter δ is shown in Fig. 3.4. The limit $\delta = 1$ yields an anomaly that is triangular, and the limit $\delta \rightarrow \infty$ gives the top-hat profile. Notice that the half-width is the same for all values of δ . For different values of the shape parameter there is a significant difference in the corresponding surface velocity. For $\delta = 6$ the maximal velocity is ~ 1 and for $\delta = 1$ it reduces to ~ 0.5 . Therefore the corresponding effective Rossby number is for $\delta = 6$ equal to the Rossby number of the dimensional setting $\tilde{R}\bar{o} = U/(af)$, and for $\delta = 1$ it is reduced by a factor of 2.

The nondimensional latitudinal streamfunction takes the form

$$\bar{\psi}(x, z) = \bar{\psi}_{pr}(x, z) + \bar{\psi}_{bc}(x, z) + \bar{\psi}_{sh}(x, z) \quad (3.1)$$

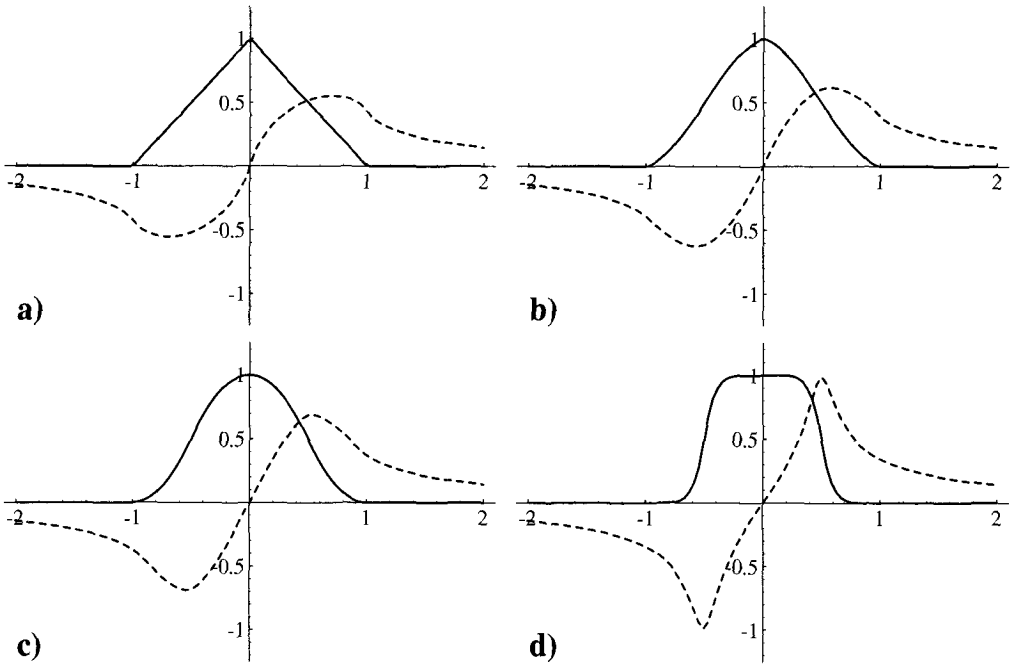


FIG. 3.4: θ -anomaly and velocity for four different values of the shape parameter δ . Shown are potential temperature profiles (solid lines) and velocities (dashed lines) for δ values 1, 1.5, 2 and 6, respectively.

where the different terms on the right-hand side of this equation denote respectively the profile, the baroclinic, and the barotropic shear component of the flow. The profile term $\bar{\psi}_{pr}$ is determined by the surface temperature profile and the conditions $\Delta \bar{\psi}_{pr} = \bar{q}_{pr} = 0$ and $\bar{\psi}_{pr} \rightarrow 0$ for $z \rightarrow \infty$, i.e. its spectral decomposition is given by:

$$\bar{\psi}_{pr}(x, z) = \sum_l C_l e^{-|k_l|z} e^{ik_l x} \quad (3.2)$$

where $k_l = 2\pi l/L$, $L = b - a$, and a, b are the northern, and southern boundary-values of the domain. The coefficients C_l are given by

$$\bar{\Theta}_{pr}(x) = - \sum_l C_l |k_l| e^{ik_l x} = \sum_l \vartheta_l e^{ik_l x} \quad (3.3)$$

where $\bar{\Theta}_{pr}$ captures the L -periodic component of the zonal surface temperature distribution. The baroclinicity is given by

$$\bar{\psi}_{bc}(x, z) = Bxz, \quad (3.4)$$

i.e. B measures the strength of the baroclinicity. $\bar{\psi}_{sh}$ is the part of the streamfunction describing the barotropic shear by

$$\bar{\psi}_{sh}(x, z) = \frac{1}{2} \Lambda x^2. \quad (3.5)$$

The shear can be decomposed into a purely rotation and a purely deformation part (see, e.g., Davies 1994). The flow structure of the shear and its deformation and rotation component are illustrated in Fig. 3.5. Notice that this streamfunction fulfills the condition of uniform potential vorticity $q = \Lambda$, i.e. the potential vorticity has only a contribution from the vorticity field of the shear flow.

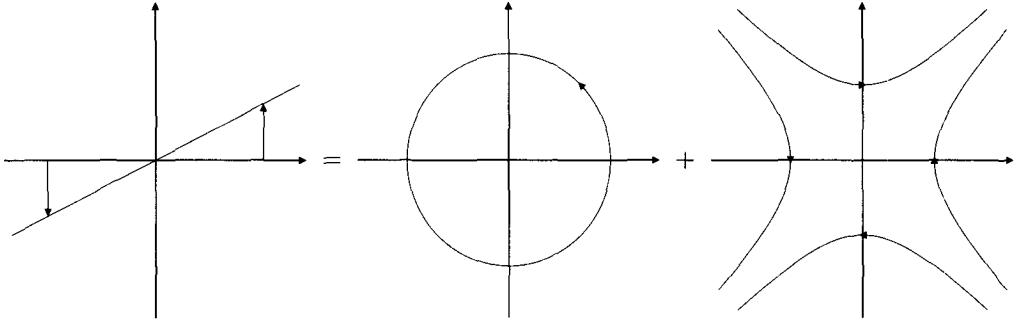


FIG. 3.5: Decomposition of the shear into a purely rotation and purely deformation part. The corresponding deformation and rotation parameters are equal to the shear parameter.

3.3.2 Normal Mode Analysis

To carry out the normal mode analysis we split the flow variables such that

$$\psi(x, y, z, t) = \bar{\psi}(x, z) + \psi'(x, y, z, t) \quad (3.6)$$

where the overbar and the prime symbols refer respectively to the basic state as described in subsection 3.3.1 and the deviation therefrom. The time evolution is given by the linearised version of the thermodynamic equation (2.6):

$$\frac{\partial \Theta'}{\partial t} + u' \frac{\partial \bar{\Theta}}{\partial x} + \bar{v} \frac{\partial \Theta'}{\partial y} = 0. \quad (3.7)$$

In accord with this equation, the different zonal modes do not interact, and thus we can describe the perturbation by a spectral representation in (x, z) coupled with a single fixed wave component in the longitudinal direction and an exponential time-dependency, i.e.

$$\psi'^{(m)}(x, y, z, t) = \sum_l P_l^{(m)} e^{ik_l x} e^{im y} e^{-\mu_{l,m} z} e^{\sigma_m t} \quad (3.8)$$

with $\mu_{l,m} = \sqrt{k_l^2 + m^2}$ (m is the zonal wave-number and is fixed as mentioned above). Notice that this perturbation fulfills $\Delta \psi' = q' = 0$, i.e. the potential vorticity of the total flow remains uniform.

This approach hinges upon the use of periodic boundary conditions in the x -direction. Its validity rests upon the amplitude of the perturbation being small near the boundaries and this is verified a posteriori.

By inserting the spectral representation of both $\bar{\psi}$ and ψ' into the linearised equation (3.7) the stability problem is converted into an algebraic eigenvalue problem. Details of this procedure and the accompanying numerical treatment are discussed in appendix D.

The results reported here have been obtained with a spectral resolution of 186 complex components covering a computational domain $a = -5$ and $b = 5$. The number of grid points along the x -axis to calculate the Fourier components has been 1024, i.e. much more than the dimension of the truncated eigenproblem matrix. In Appendix D.2 consideration is given to the sensitivity of the results with respect to these values.

3.3.3 Mathematical Symmetries

Symmetries in quasi-geostrophic (or in geostrophic space of semi-geostrophic) normal mode analysis for symmetric basic states can survive the nonlinear phase of the development. The symmetry, which represents a generic trajectory in the phase space of these models, can be broken in various ways, e.g. by superimposing an asymmetric component (such as barotropic shear) on the basic state (Davies et al. 1991), by internal PV gradients, by introducing a different geometry (β -effect or spherical geometry), or by the dynamical framework (PE vs. SG) (Snyder et al. 1991)³.

Here the temperature bands are chosen to be symmetric. Therefore a transformation of the axes $(x, y) \rightarrow (-x, -y)$ and simultaneously $B \rightarrow -B$ does not change the instability characteristics. This transformation corresponds merely to x (y) pointing to the north (west) and the north (south) is in the transformed space the warm (cold) area. We therefore restrict in what follows on $B \geq 0$.

A second symmetry has been shown to hold for any two-dimensional basic state that is symmetric (Davies et al. 1991), i.e. here if $B = 0$. In this case the perturbation streamfunction fulfills

$$\psi'(x, y, z, t) = -\psi'(-x, y - \lambda/2, z, t)$$

where λ is the wave length of the mode.

3.3.4 Growth Rates, Wave Lengths, and Structures of the Normal Modes

The analogue of the Charney and Stern (1962) instability criterion for SQG states that an initial zonal state, characterised by a surface temperature distribution $\bar{\Theta}$, is stable unless

$$\int \frac{\partial \bar{\Theta}(x)}{\partial x} (\eta'(x, y))^2 dx dy = 0$$

where $\eta'(x, y)$ stands for the north-south parcel displacement (Eliassen 1983, Schär and Davies 1990). For the reference temperature states characterised in subsection 3.3.1 by the baroclinicity B and the profile parameter δ we have that $\partial_x \bar{\Theta}(x) = B$ outside of the band,

³It has been demonstrated that for broken symmetry SG and PE capture basically the same dynamical features for a frictionless fluid of uniform quasi-geostrophic potential vorticity on an f -plane (Wernli et al. 1997).

i.e. for $x \notin [-1, 1]$. It follows that the north-south displacement and therefore the amplitude of the normal mode can only have a significant amplitude over a limited area (for $B \neq 0$)⁴. Furthermore if $B > \delta > 1$, then $\partial_x \bar{\Theta}(x) > 0, \forall x$ and the basic state is stable for such a configuration.

The analysed parameter range has been chosen to be $\{0 \leq B \leq 3\}$, $\{1 \leq \delta \leq 4\}$, and $\{-1/2 \leq \Lambda \leq 3/2\}$. In the two settings given in Table 3.1 a baroclinicity value of $B = 1$ corresponds to a temperature contrast for the two settings of 3.4 K (I) resp. 10.2 K (II) over the half-width of the band which is 250 km (I) resp. 500 km (II). Likewise a shear value $\Lambda = 1$ corresponds to velocity field contrast over the half-width of the band of 10 m s^{-1} (I) resp. 30 m s^{-1} (II).

A detailed analysis is now provided of the growth rate and wave length in the three-dimensional parameter space (B, Λ, δ) . In Figs. 3.6, 3.7, and 3.8 two of the parameters are fixed and the growth rate is plotted against the wave number and the third parameter.

Dependence on the barotropic shear

In Fig. 3.6 baroclinicity and the profile parameter are fixed. The baroclinicity increases from upper to lower panels and vanishes in the upper panels. The left panels are derived for a triangular θ -distribution, and the profile parameter increases from left to right.

In general a cyclonic shear (i.e. $\Lambda > 0$) results in an increase of the wave length of the most unstable mode. Except for very small profile parameters δ (e.g. $\delta = 1$) anti-cyclonic shear stabilises the θ -band, cf. stabilisation by adverse shear for the case of a pure vorticity strip (Dritschel 1989b).

Note that for vanishing baroclinicity the triangular profile is more unstable than the smoother counterpart, and the unstable modes are less confined to a specific wave number window. For $B = \delta$ which marks the critical value of the instability criterion the growth rate is significantly smaller than in the cases where $B < \delta$. Furthermore for the setting $B = 1$, there is besides the cyclonic unstable mode, an anti-cyclonic unstable mode with a growth rate that is even larger than the growth rate of the cyclonic mode, i.e. a shear line with a baroclinic background is not necessarily stabilised by adverse shear.

Dependence on the baroclinicity

Fig. 3.7 shows the instability characteristics for fixed values of the barotropic shear and the profile parameter. The upper panels correspond to anticyclonic shear, the middle panels to the unsheared case and the lower panels to cyclonic shear. The profile parameter increases from left to right panels.

The results are again consistent with the instability criterion, i.e. the basic state is stable for $B > \delta$. As a consequence for small profile parameters a superimposed baroclinicity stabilises the band. For profile parameters $\delta > 2$ the addition of a baroclinic background can destabilise the θ -anomaly. The wave length of the most unstable mode is in general reduced

⁴This comment provides even an a priori justification for the use of periodic boundary conditions in the x -direction. A further a posteriori justification follows from an inspection of the structures of the normal modes (see Fig. 3.9).

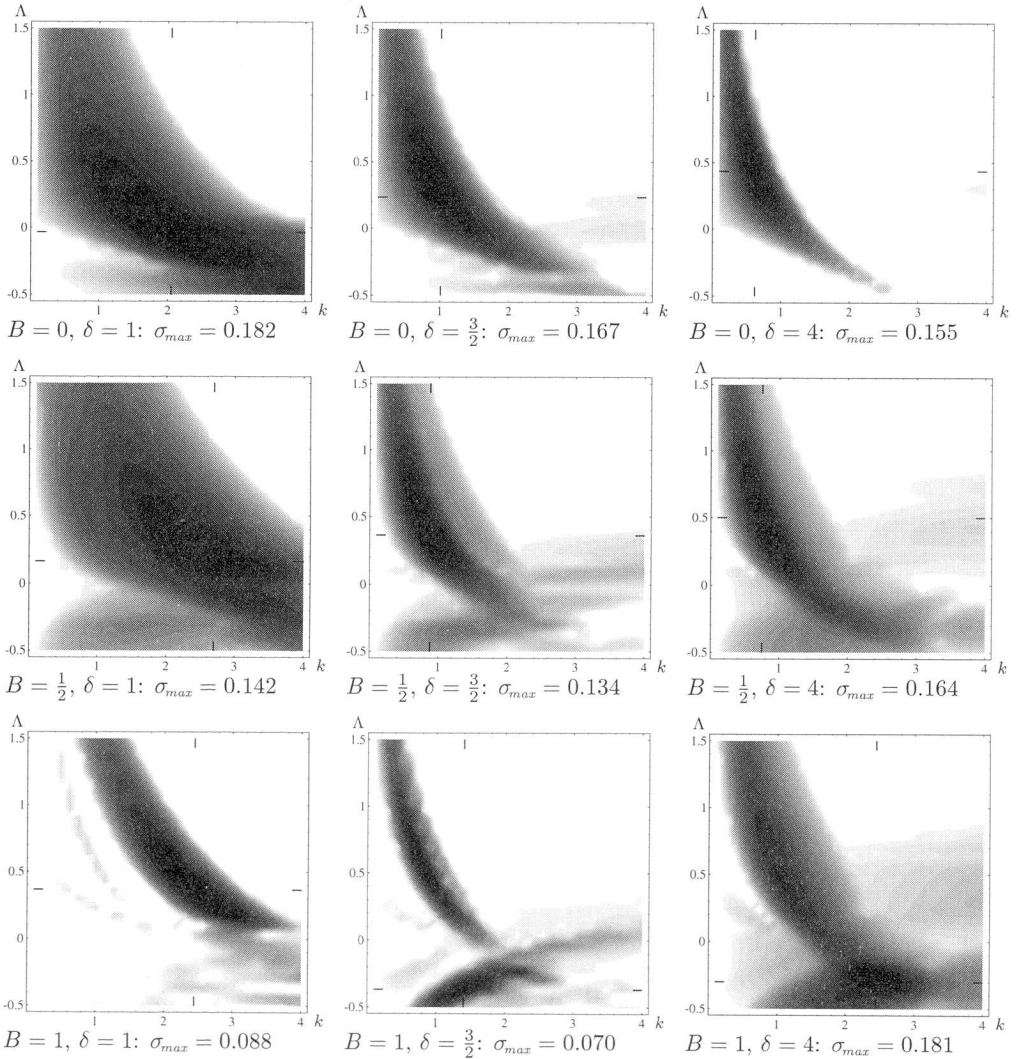


FIG. 3.6: Dependence of the growth rate on the wavenumber k and the shear parameter Λ for various values of the baroclinicity B and the profile parameter δ . The ticks indicate the wave number and the shear of the most unstable mode.

by the baroclinicity.

Dependence on the profile

In Fig. 3.8 the barotropic shear and the baroclinicity are fixed. The barotropic shear varies from upper to lower panels as in Fig. 3.7, and baroclinicity increases from left to right. For

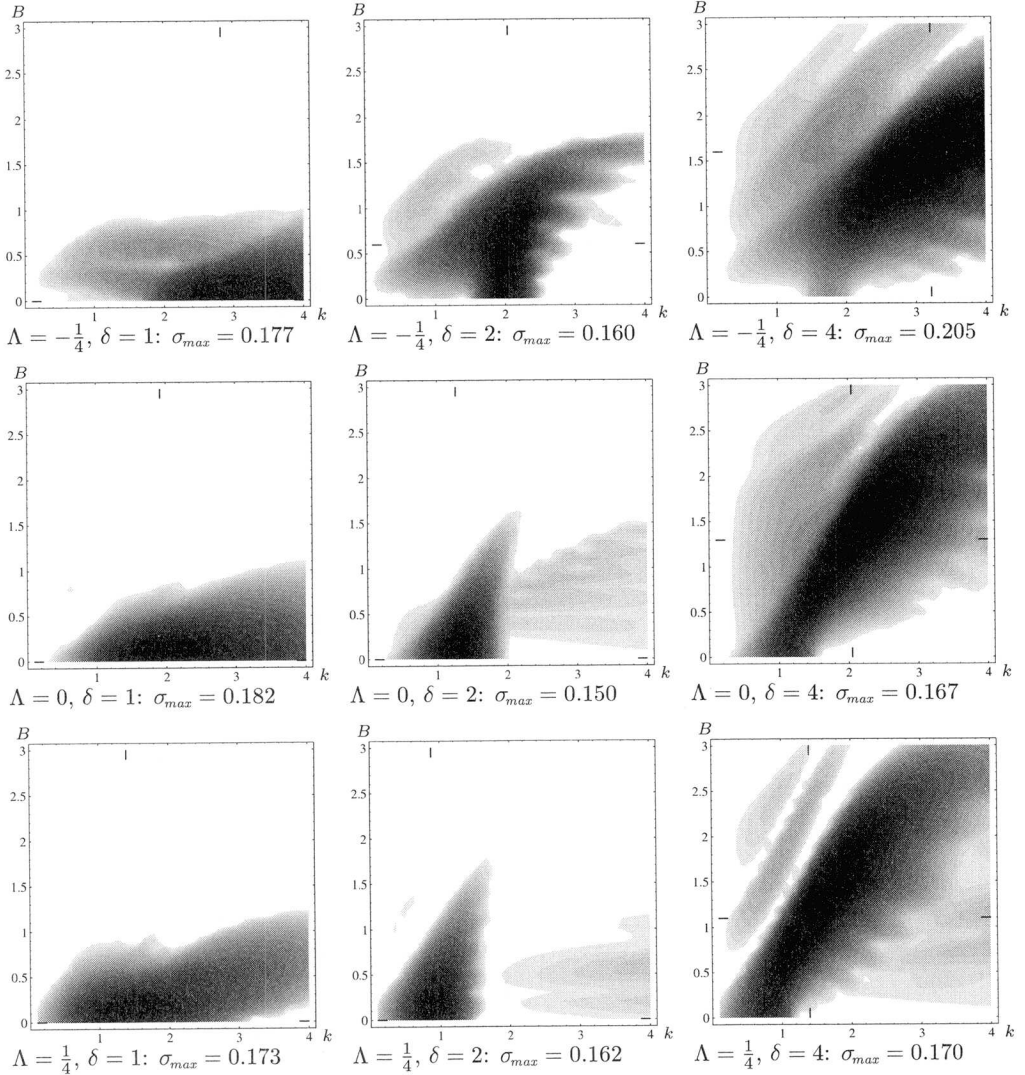


FIG. 3.7: Dependence of the growth rate on the wavenumber k and the baroclinicity B for various values of the shear parameter Λ and the profile parameter δ . The ticks indicate the wave number and the baroclinicity of the most unstable mode.

vanishing baroclinicity, stronger temperature gradients at the edges of the band result in a stabilisation and an increase of the wave length. Strong dependence of the wave length and the growth rate occurs for profiles close to the triangular case.

Again, in line with the instability criterion, the triangular configuration is stable for $B > 1$ (see right panels). For a baroclinic background, θ -strips with a stronger gradient at

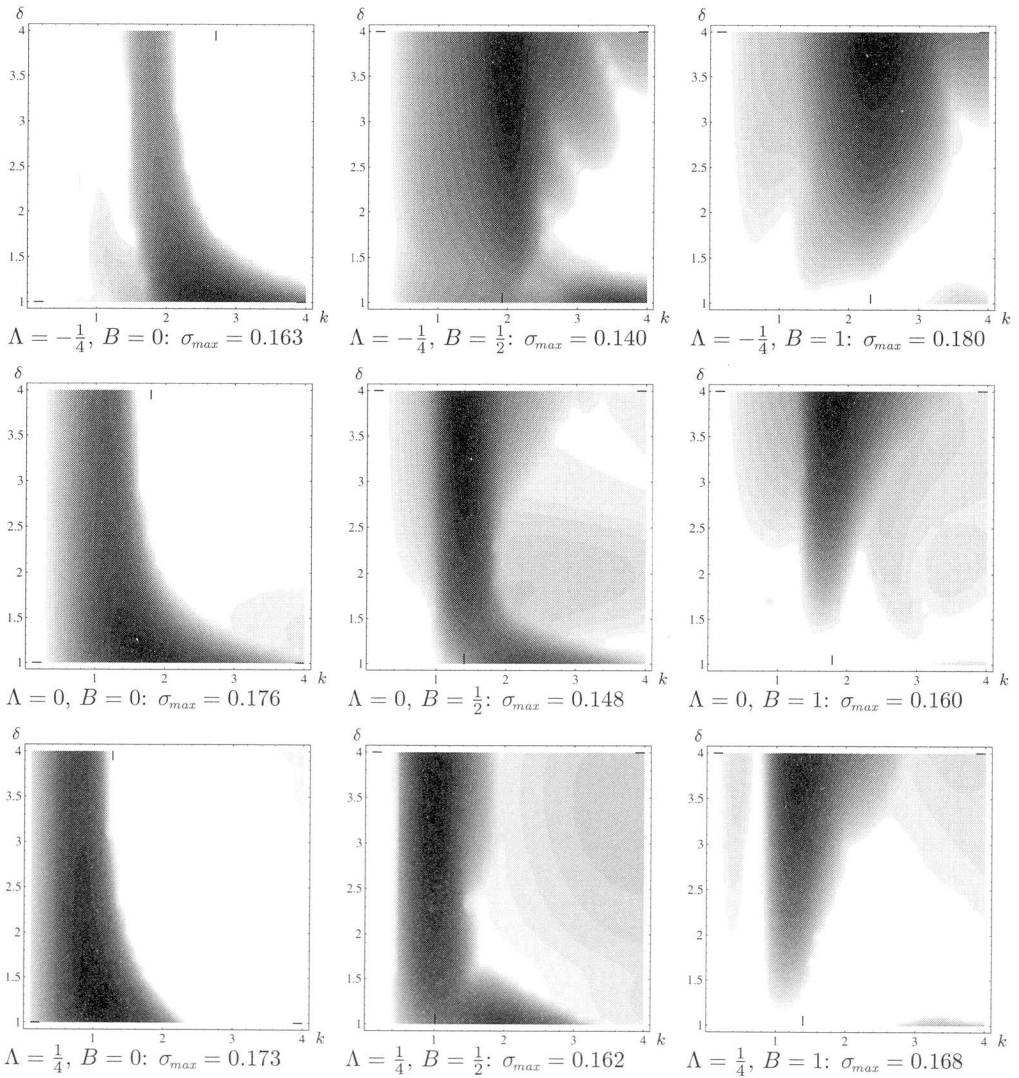


FIG. 3.8: Dependence of the growth rate on the wavenumber k and the profile parameter δ for various values of the shear parameter Λ and the baroclinicity B . The ticks indicate the wave number and the profile of the most unstable mode.

the edges become more unstable, and their wave length is almost independent of the profile parameter.

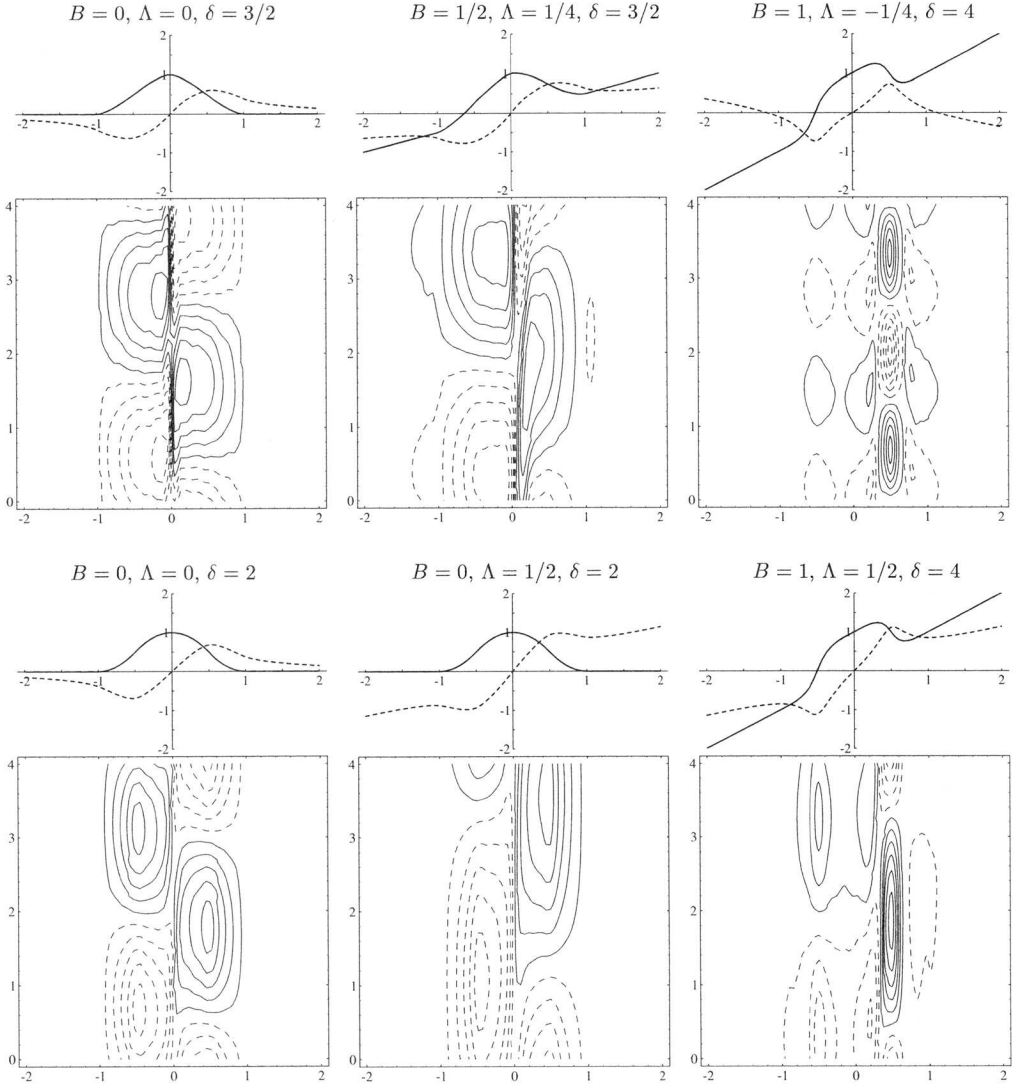


FIG. 3.9: The structure of the most unstable eigenmodes for selected baroclinicity, shear, and profile values. Shown is the temperature profile (solid line) and the velocity field (dashed line) at the surface, and the potential temperature perturbation at the surface.

The normal modes

Out of the palette of unstable modes we select for display purposes some characteristic values of the baroclinicity, the background shear and the profile parameter. The horizontal structure of the corresponding normal modes are depicted in Fig. 3.9. The selected parameters

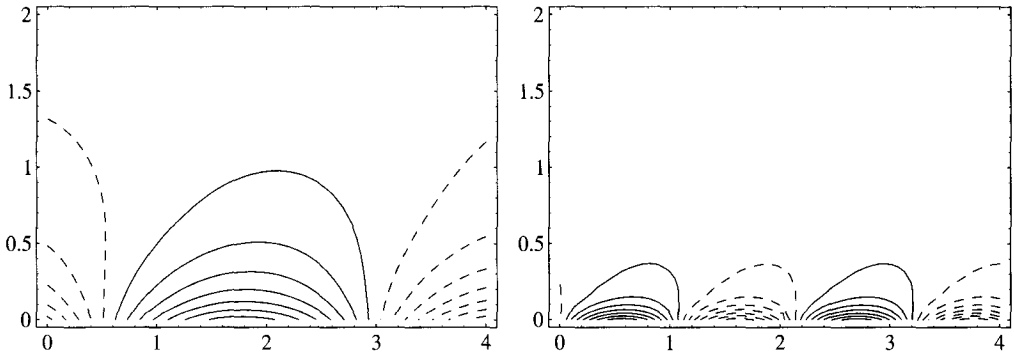


FIG. 3.10: The vertical structure of the most unstable eigenmodes for the two parameter sets ($B = 0, \Lambda = 0, \delta = 2$) and ($B = 1, \Lambda = -1/4, \delta = 4$). Along-band sections are shown for $x = 1/2$.

are:

($B = 0, \Lambda = 0, \delta = 3/2$ or $\delta = 2$): The modes exhibit the symmetry described in subsection 3.3.3. For the profile that is closer to the triangular case, the maximal negative and positive amplitudes are close to the center of the temperature strip. For the basic state with larger profile parameter the maxima are co-located with the maximum of the gradient of the θ -distribution. It could therefore be argued that smaller profile parameters favour the interaction of the waves at the edges of the strip and this could explain the dependence of the growth rate on the profile (see left panels on Fig. 3.8).

($B = 1/2, \Lambda = 1/4, \delta = 3/2$): Addition of baroclinicity results in a basic state configuration of a surface temperature band in a baroclinic environment. This is an idealised version of the configuration analysed by Schär and Davies (1990). The structure of their normal mode and of the present mode is very similar. We have on the warm and on the cold side of the band an amplitude of similar strength. The asymmetry with respect to the center of the band is directly linked to the relative difference in scale and strength of the local thermal gradients on either side of the shear line.

($B = 0, \Lambda = 1/2, \delta = 2$): This mode should be compared to the analogue unsheared mode. It indicates that the mathematical symmetry of subsection 3.3.3 still holds in the sheared case, and the increase of the wave-length due to cyclonic shear.

($B = 1, \Lambda = -1/4$ or $\Lambda = 1/2, \delta = 4$): These two modes correspond to the two branches of unstable modes as seen in the lower right panel of Fig. 3.6. For both modes we have a significant amplitude only on the warm side of the θ -band where the velocity field has a maximum. On the cold side there are two, and on the warm side one, weak satellite. Note the difference in the phase shift of these satellites for the cyclonic and anti-cyclonic case.

Fig. 3.10 depicts the vertical structure of two modes with significant different wave lengths. It demonstrates that the perturbation temperature is confined to the lowest few kilometers and is directly related to the wave length of the mode, and the downstream phase shift in the vertical becomes evident.

Table 3.2 records the wave lengths and growth rates for the two dimensional settings

	Setting	$B = 0$	$B = 0$	$B = 1/2$	$B = 0$	$B = 1$	$B = 1$
		$\Lambda = 0$ $\delta = 3/2$	$\Lambda = 0$ $\delta = 2$	$\Lambda = 1/4$ $\delta = 3/2$	$\Lambda = 1/2$ $\delta = 2$	$\Lambda = -1/4$ $\delta = 4$	$\Lambda = 1/2$ $\delta = 4$
doubling time (h)	I	30.2	32.4	36.7	30.1	26.1	28.3
	II	19.9	21.3	24.1	19.8	17.2	18.6
wave length (km)	I	1100	1225	1515	2285	665	1490
	II	2200	2450	3030	4570	1330	2980

TABLE 3.2: Wave length and doubling time for the same specific values of the baroclinicity, the barotropic shear, and the profile as in Fig. 3.9.

introduced in Table 3.1. Note the enormous range of unstable wave lengths and the comparatively small variability in the doubling times.

A comment on the phase speed

From symmetry considerations it is straightforward to infer that for $B = 0$ either the most unstable mode is degenerate and occurs in pairs with opposite phase velocities or that the phase velocities vanish. From the numerical results we infer that the phase velocities vanish for the most unstable mode but there are weaker branches of unstable modes that are in fact degenerated. The corresponding growth rates of these modes are at least a factor of 10 smaller than the most unstable mode, and are not discussed further. For a baroclinic background the modes have a non-trivial phase speed which depends on the thermal wind related to the baroclinicity.

3.4 Nonlinear QG-Simulations

In this section we study the nonlinear evolution of: – (i) modal perturbations of infinite thermal bands; and (ii) temperature strips of finite length. We compare aspects of the nonlinear evolution with the results of linear theory, i.e. we study the influence of the background shear, the baroclinicity, and the shape parameter on the nonlinear evolution.

The equations are integrated on a doubly periodic domain. The width of the numerical domain has been chosen to be 8 in dimensionless units (– corresponding to 8 times the half-width of the shear line). The length is given by the wave length of the mode. The resolution for the numerical integration is 512×256 for the modal perturbations and 512×512 spectral components for the anomalies that are finite in length. In the latter case the integration domain is 8×8 for “short” anomalies and 16×16 for “long” ones.

There is, on the one hand, the need to have a large enough domain, such that the neighbouring vortices do not interact, and on the other hand it is appropriate to have a highest possible resolution to ensure that the numerical solution captures the basic features of the dynamics. The chosen domain is a compromise between these two contradicting requirements. In appendix E we discuss the influence of the domain size and the resolution on the evolution.

3.4.1 Infinite Band, Normal Mode Initial Conditions

The nonlinear evolution of an infinite band of a temperature anomaly in a barotropic un-sheared environment has been discussed by Held et al. (1995) and Jukes (1995). They pointed out the distinction from the BQG model at later times of the evolution. In the SQG dynamical framework there is, on the thin filaments joining the chain of evolving vortices, a secondary instability that forms a smaller-scale family of vortices. Here we illustrate the nonlinear evolution of some representative solutions of the palette of unstable modes.

The experiments were initialised by adding the normal mode with an amplitude of 10% of the amplitude of the zonal temperature profile.

Baroclinic modes

We start with the mode which exhibits a close resemblance to that found in Schär and Davies (1990), i.e. the ambient flow and the profile parameter are $B = 1/2$, $\Lambda = 1/4$, and $\delta = 3/2$. Fig. 3.11 shows the potential temperature at the surface at $t = 25$ and $t = 45$. (Note that for

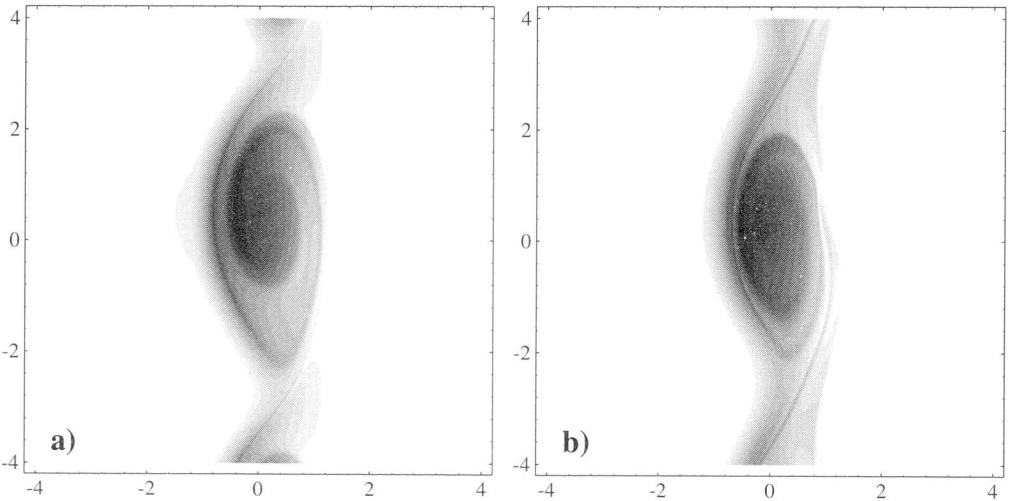


FIG. 3.11: Nonlinear evolution of the normal mode for $B = 1/2$, $\Lambda = 1/4$, and $\delta = 3/2$ at $t = 25$ (panel a) and at $t = 45$ (panel b). Shown is the potential temperature at the surface where we subtracted the uniform baroclinic component.

the display we subtracted the uniform baroclinic component). Both, the normal mode and the nonlinear development are very close to what has been obtained by Schär and Davies (1990). Equilibration occurs and the system reaches a quasi-steady, stable configuration. The individual vortices are kept in position by the action of their neighbours.

This demonstrates that our highly idealised ambient flow characterised by a uniform baroclinicity exhibits already the main ingredients for the interaction of the local anomaly with the environmental flow.

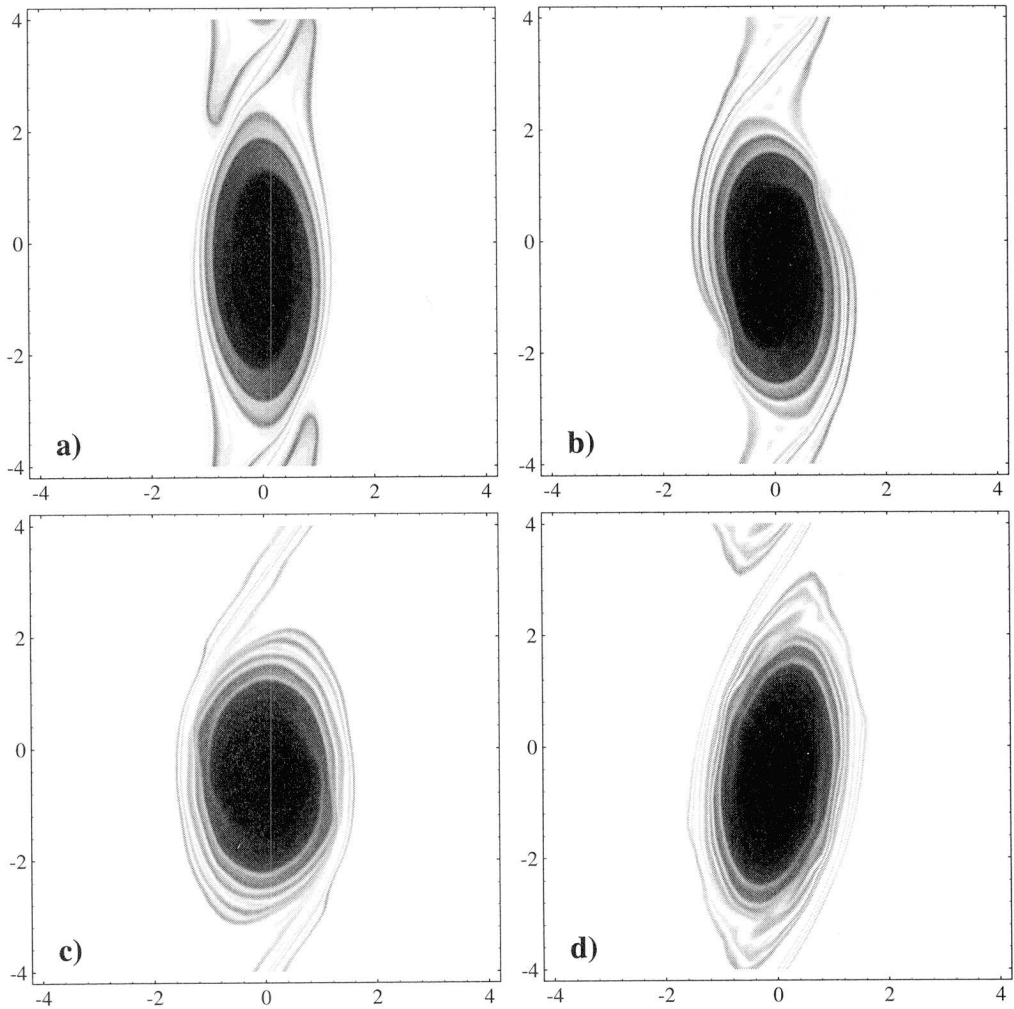


FIG. 3.12: Nonlinear evolution of the normal mode for $B = 0$, $\Lambda = 1/4$, and $\delta = 2$ at $t = 35, 40, 45$ and 50 (panels a–d). Shown is the potential temperature at the surface.

Similar simulations (not shown) have also been performed for the other baroclinic modes of Table 3.2. Equilibration is reached even on shorter time scales for the more unstable modes, e.g. for $B = 1$, $\Lambda = -1/4$, $\delta = 4$ and for $B = 1$, $\Lambda = 1/2$, $\delta = 4$.

Cyclonically sheared modes

Here the shear parameter is chosen to be $\Lambda = 1/4$. For $\delta = 2$ this corresponds to the shear value for maximum growth rate, and $\delta = 4$ corresponds to a value slightly weaker than would lead to maximum growth rate. The nonlinear development is shown in Fig. 3.12. Elliptical

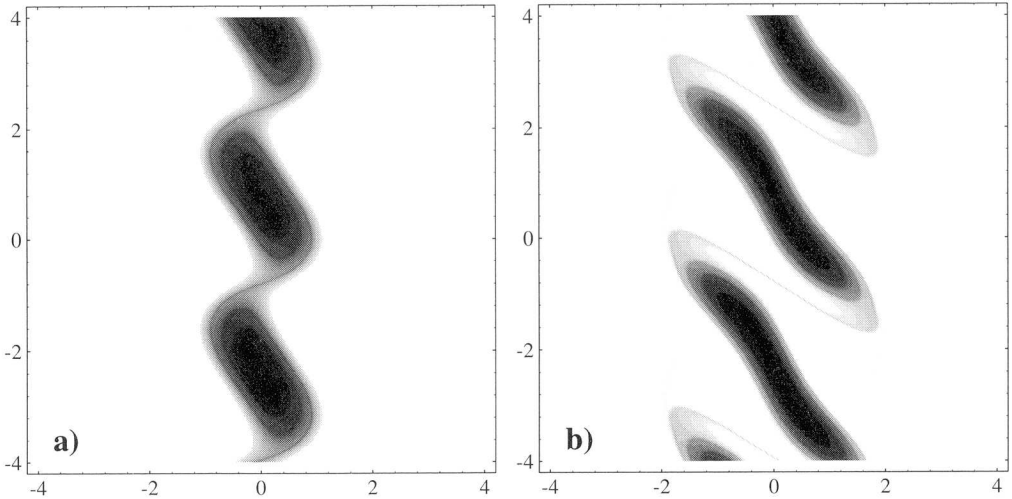


FIG. 3.13: Nonlinear evolution of the normal mode for $B = 0$, $\Lambda = -1/4$, and $\delta = 2$ at $t = 20$ (panel a) and at $t = 30$ (panel b). Shown is the potential temperature at the surface.

vortices form with a length to width of $\sim 4 : 1$ and they are joined by thin filaments. In turn these filaments wind up around the vortex forming a boundary of alternating high and low temperature values. (Compare the structure of the vortex depicted in panel c) with that of the observed vortex in the WV satellite image of Fig. 3.1).

The cascade to small scales represents an irreversible process. It has been suggested that this may have some relevance concerning the exchange of stratospheric and tropospheric air (e.g. Appenzeller 1994, Wirth 1996).

Anti-cyclonically sheared modes

Here the shear parameter is set to $\Lambda = -1/4$. Larger anti-cyclonic shear would stabilise the PV-band. The nonlinear evolution of the band is starkly different to that of the cyclonic sheared case (Fig. 3.13). The band breaks into individual elongated vortices that rotate counter clock-wise, in concert with the barotropic shear (cf. the image Fig. 3.5), acts to stretch the vortices such that their length increases on a small time-scale by a factor of two. This in turn enables a second instability to evolve on the elongated individual anomalies. In the further development these elongated anomalies collide (not shown).

Unsheared modes

The nonlinear development for a temperature strip in a barotropically unsheared environment is shown in Fig. 3.14 for $\delta = 2$ and in Fig. 3.15 for $\delta = 4$. A striking feature is the formation of a secondary instability as already noted by e.g. Held et al. (1995). However contrary to their results, the secondary instability on the thin filaments is only observed to occur in the direction of the small semi-axes of the vortex when the filament starts to

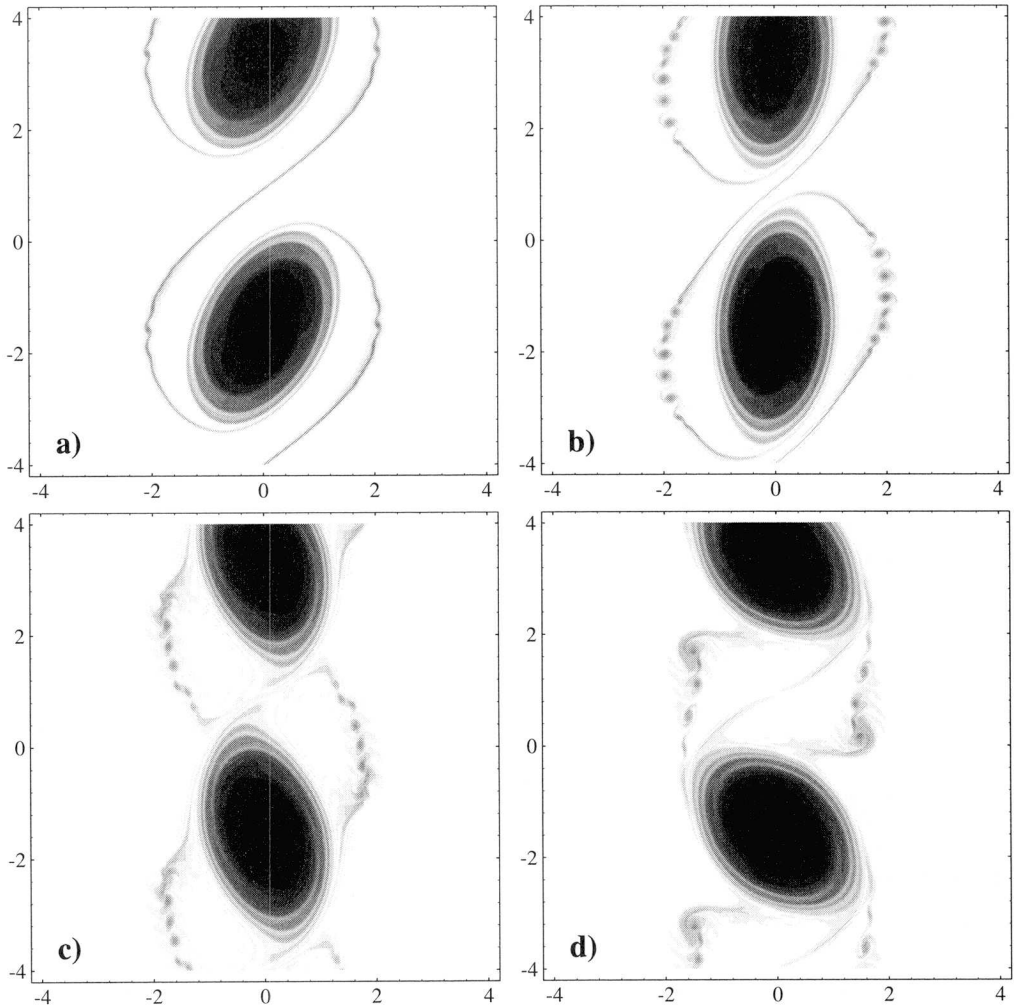


FIG. 3.14: Nonlinear evolution of the normal mode for $B = 0$, $\Lambda = 0$, and $\delta = 2$ at $t = 35, 40, 45$ and 50 (panels a–d). Shown is the potential temperature at the surface.

wind up around the vortex and comes close to it. Held et al. (1995) found such a secondary instability not only on the whole length of the filament, but also on the boundary of the vortex. As a caveat it has to be noted, as mentioned in the introduction, that the scales corresponding to the secondary instability are such that SQG may no longer be applicable.

The number of the small scale vortices that develop on the filament differ between the $\delta = 2$ and $\delta = 4$ case, and may be linked to the larger wave length of the $\delta = 4$ mode, and that therefore the filament parallels on a larger scale the elliptical vortex.

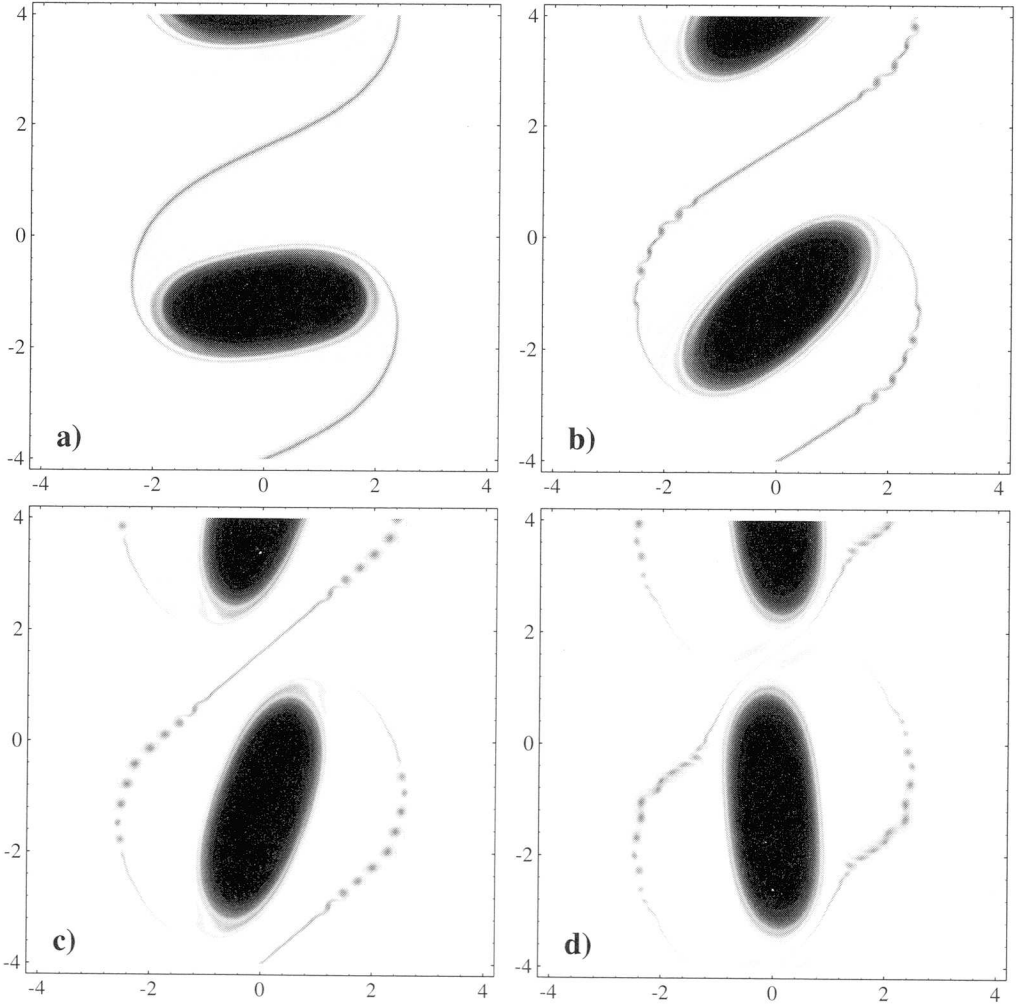


FIG. 3.15: Nonlinear evolution of the normal mode for $B = 0$, $\Lambda = 0$, and $\delta = 4$ at $t = 35$, 40, 45 and 50 (panels a-d). Shown is the potential temperature at the surface.

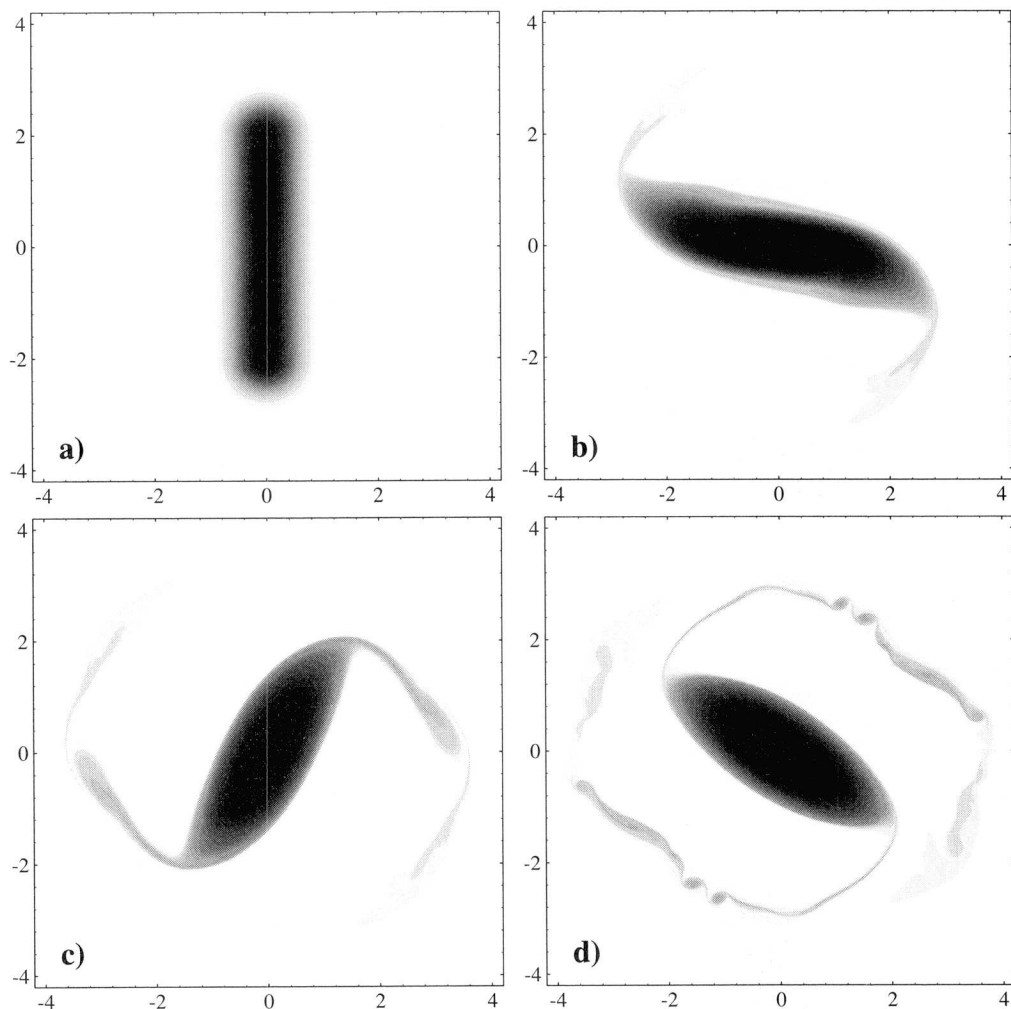


FIG. 3.16: Nonlinear evolution of a finite strip for $\delta = 2$ at $t = 0, 20, 35,$ and 50 (panels a-d). Shown is the potential temperature at the surface.

3.4.2 Finite Strips

Finiteness of bands can also act to excite instability. Here we compare the evolution of such bands with the nonlinear development of the normal modes. Simulations are performed for strips with a length that is comparable to the length of the analogue most unstable normal mode (“short” strips) and for strips that are twice as long (“long” strips).

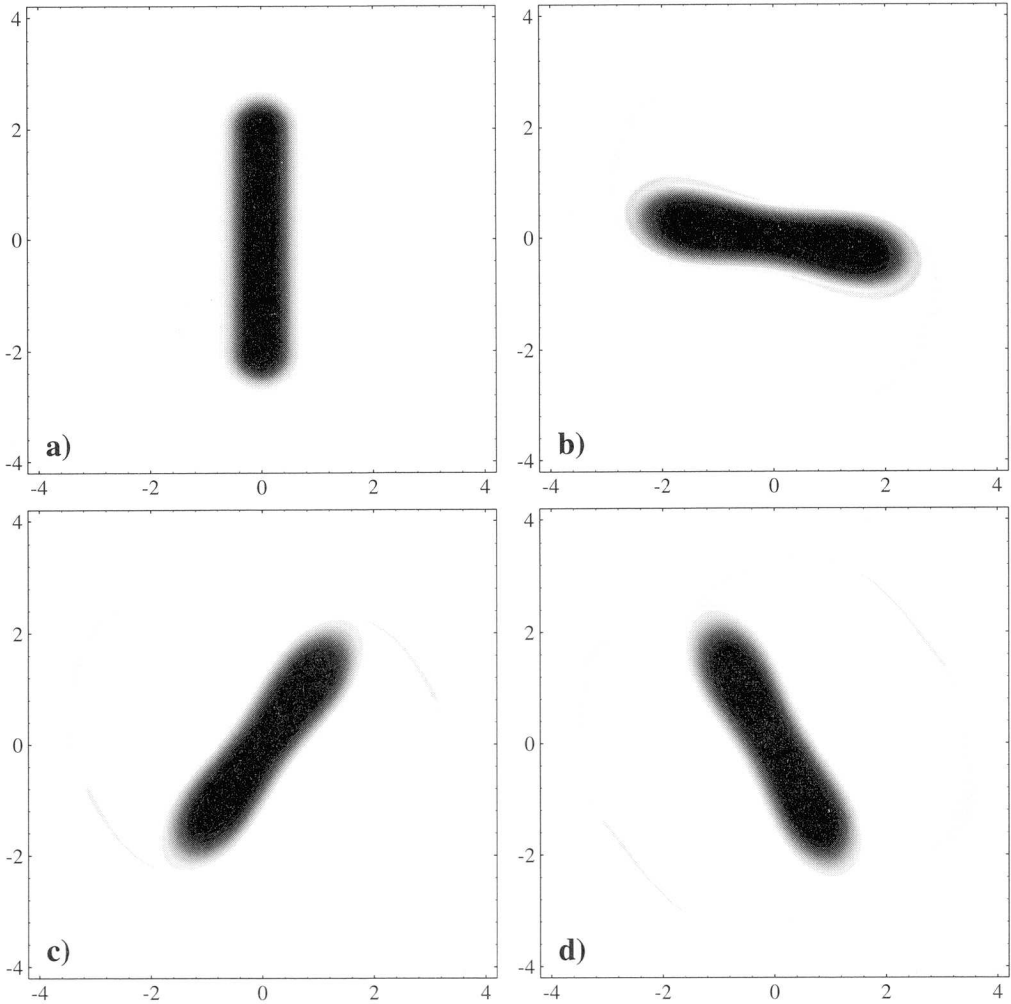


FIG. 3.17: Nonlinear evolution of a finite strip at $\delta = 4$ at $t = 0, 20, 35,$ and 50 (panels a-d). Shown is the potential temperature at the surface.

“Short” strips

Figs. 3.16 and 3.17 show the evolution of a strip of finite length with a length to width ratio of $5 : 1$ for $\delta = 2$ and $\delta = 4$. For $\delta = 2$ there is a process of axisymmetrisation and filamentation. The length to width ratio is thereby reduced to $\sim 4 : 1$. This has been recognised as a process which can for example stabilise elliptical vortices in the nonlinear regime (Melander et al. 1987). Note that from the linear analysis the wave length of the most unstable mode for the analogue infinite θ -strip would be 5, i.e. of the same length as the strip. Again in a late phase of the development, a secondary instability occurs on the

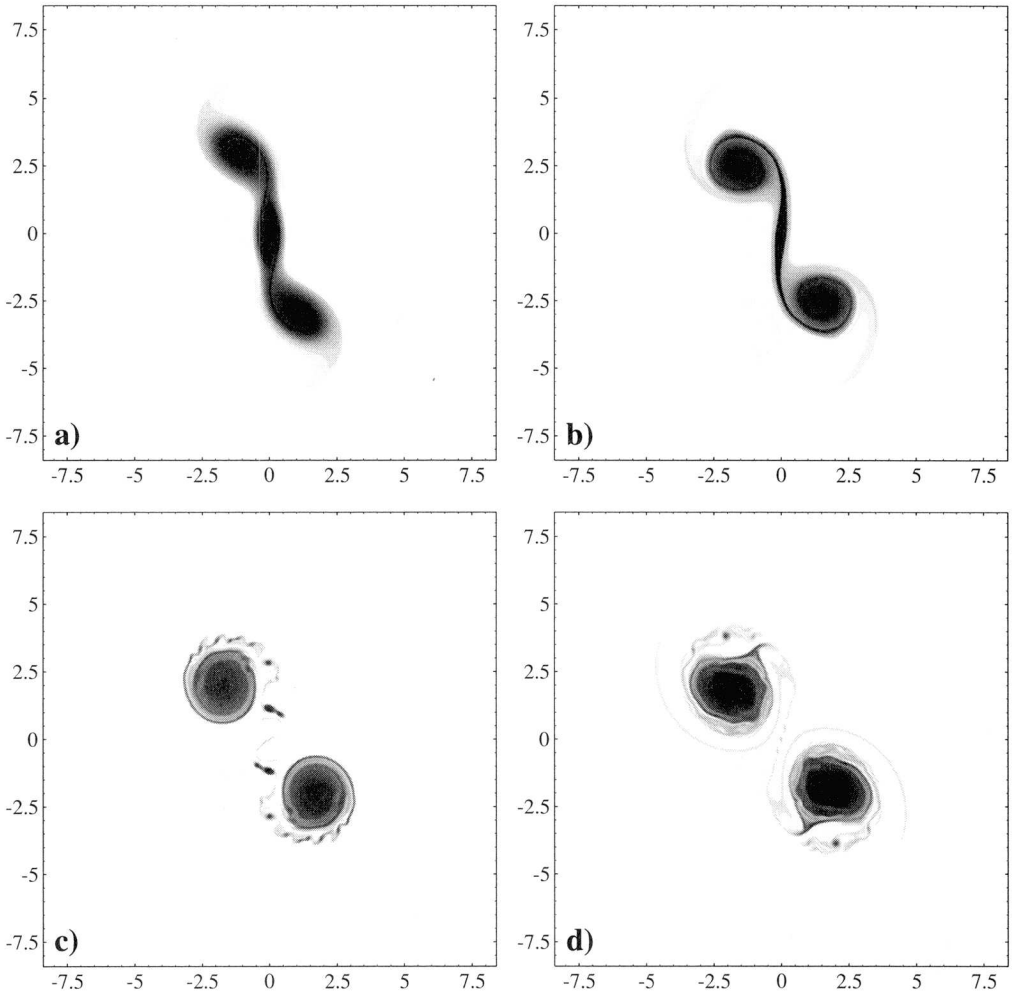


FIG. 3.18: Nonlinear evolution of a finite strip for $\delta = 2$ at $t = 15, 25, 40,$ and 50 (panels a-d). Shown is the potential temperature at the surface.

extruded streamers.

The analogue simulation with profile parameter $\delta = 4$ is distinctively different. Here the wave length of the most unstable mode is 5.5, i.e. the strip is again shorter than the wave length of the unstable mode. Small filaments form at the tips of the strip, and the strip itself first develops an instability-like character. However this instability doesn't develop further, and the strip rotates without significant change of shape.

The instability analysis would favour the $\delta = 2$ strip to exhibit an evolving instability rather than the $\delta = 4$ strip.

“Long” strips

In Fig. 3.18 the nonlinear development of a strip with $\delta = 2$ and a length to width of 10 : 1 in an unsheared environment is shown. The length of this strip is slightly shorter than twice the wave length of the most unstable mode. In a first phase of the development the strip starts to form three vortex like structures. The vortex in the center is then stretched and thinned by the flow field of the two vortices at the tip of the strip. On the resulting filament again secondary vortices are formed. Note that these vortices are much stronger than the analogue secondary vortices in the case of an infinite strip. The secondary processes survive the further evolution and are linked to the “erosion process” at the periphery of the two vortices.

3.5 PE Simulations of Interior PV Anomalies

PE simulations of interior PV anomalies in a barotropic unsheared atmosphere performed with an f -plane version of the EM are presented. The model is initialised with fields generated by a quasi-geostrophic inversion of the PV structures. The characteristics of the reference state is given by a squared Brunt-Väisälä frequency of $N_0^2 = 1 \cdot 10^{-4} \text{ s}^{-2}$ in the troposphere, i.e. below an altitude of 10 km, and $N_0^2 = 5 \cdot 10^{-4} \text{ s}^{-2}$ above 10 km with a smooth transition over a layer of 1 km. Other characteristic values are $f = 10^{-4} \text{ s}^{-1}$ for the Coriolis parameter, 1000 hPa and 290 K for the reference pressure and potential temperature at the surface.

The lateral boundary conditions for the inversion are such that the tangent component of the velocity field vanishes. Two successive simulations are therefore performed. The first on a large domain and with constant boundary conditions in time, and a second nested simulation now with time depending fields at the boundary given by the first simulation. The resolution of the second simulation is 0.2° ($\sim 22 \text{ km}$) for the low-level PV anomaly and 0.33° ($\sim 37 \text{ km}$) for the upper-level intrusion.

3.5.1 Low-Level PV-Bands

The evolution of a finite low-level PV strip of $\sim 1500 \text{ km}$ length and $\sim 125 \text{ km}$ width confined between 900 and 700 hPa is shown in Fig. 3.19. The amplitude of the anomaly is $\sim 3 \text{ pvu}$ compared with a value of $\sim 0.4 \text{ pvu}$ of the ambient flow. Shown are the initial configuration and the evolution after 1, 2 and 3 days. The strip rotates and breaks into two vortices in a process similar to that observed for surface warm anomalies in the SQG framework.

In relation with diabatical processes the vertical velocity field is of interest. Initially the flow field generated by the quasi-geostrophic inversion is divergence free, and therefore the vertical velocity vanishes. In the development of the PV band, the vertical velocity pattern is linked to the two vortices which are formed by the instability process. At the leading edge of the strip downward vertical velocity is observed, and upward motion occurs on the backside of the rotating strip. Sections through the maxima of the upward motion are shown in Fig. 3.20. The vertical velocity distribution forms a coherent structure, e.g. at the leading edge of the anomaly upward motion occurs throughout the troposphere. Note

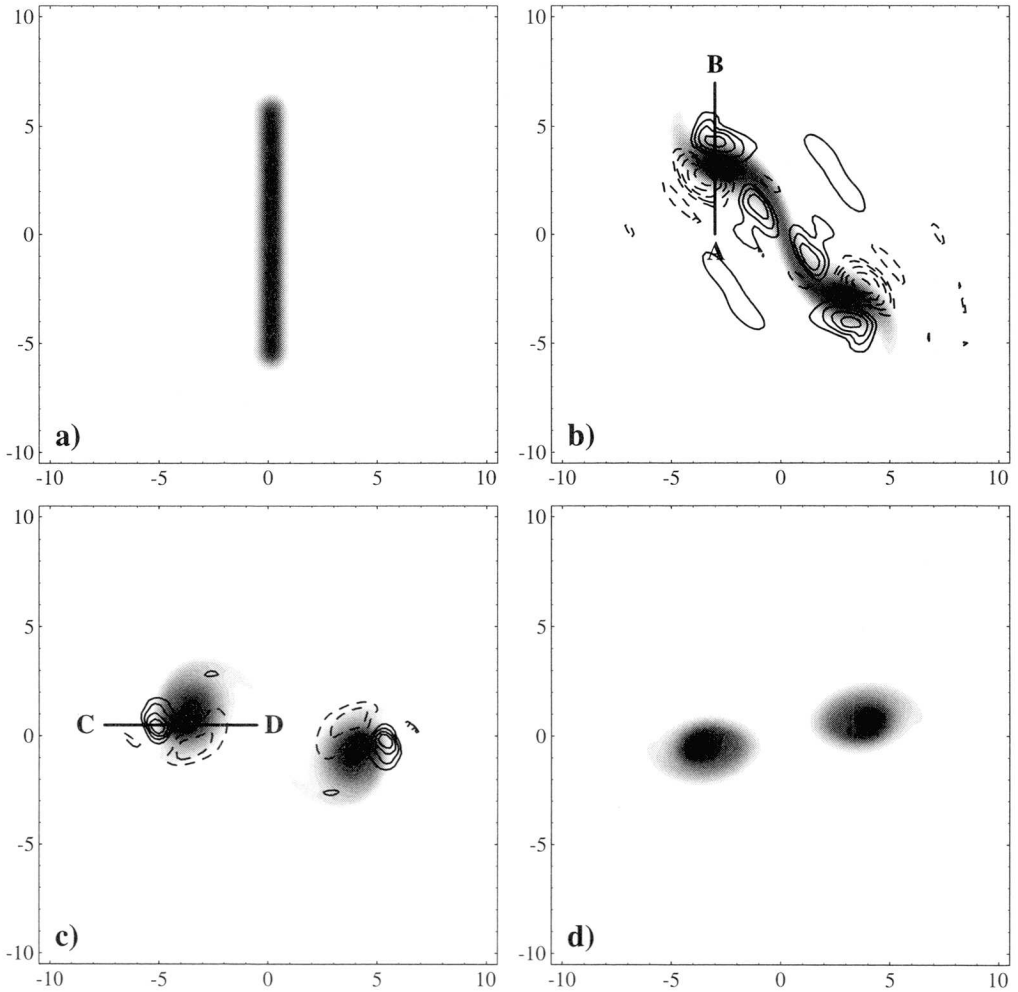


FIG. 3.19: Nonlinear evolution of a finite low-level PV strip with PE dynamics on an f -plane. The maximal amplitude of the strip is about 3 pvu, the length is ~ 1500 km and the width ~ 125 km. Shown is the evolution after 24 (panel b), 48 (panel c), and 72 hours of integration (panel d). Displayed is PV (shaded) on 800 hPa and the vertical velocity ω (solid lines indicate upward motion, dashed lines downward motion, spacing 1 hPa h^{-1} , zero line omitted).

that the vertical motion in this idealised simulation is comparatively weak (see, e.g., real data values for the frontal wave case of the next chapter), the maximum is $\sim 4 \text{ hPa h}^{-1}$. One expects that condensational heating would induce positive heating rates in the ascent regions. This in turn gives rise to positive (negative) PV rates below (above) the heating maxima, i.e. we expect PV generation on the backside of the rotating strip.

One difference between the PE simulation of the interior PV strip and the analogue

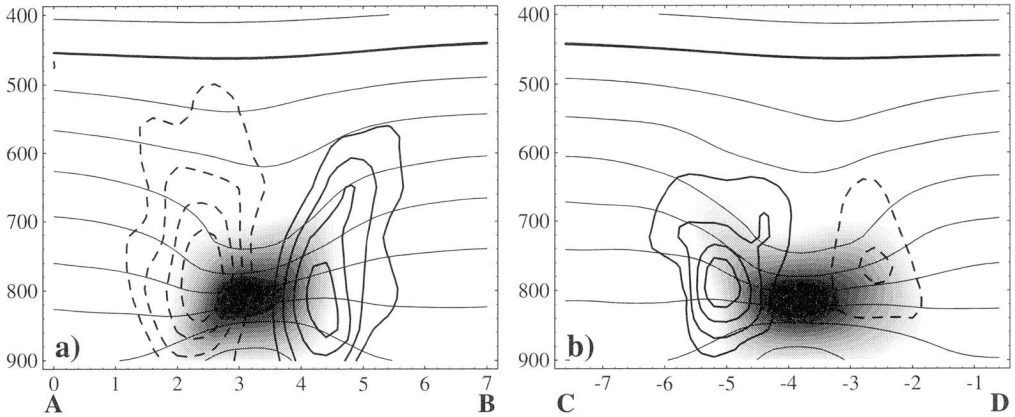


FIG. 3.20: Cross sections along the lines as indicated in Fig. 3.19b and 3.19c. Shown is PV (shaded), ω (spacing as in Fig. 3.19), and potential temperature (thin lines, spacing 2.5 K, bold line indicates 310 K).

temperature anomaly are the missing of secondary instabilities. Here it has to be noted that the effective horizontal resolution in the PE simulation is reduced by a factor of about 5 compared with the SQG analogue.

3.5.2 Upper-Level Intrusions

The evolution of a finite upper-level PV intrusion of ~ 3000 km length and ~ 250 km width is shown in Fig. 3.21. Shown are the initial configuration and the evolution after 2, 3 and 4 days. In the vertical the PV strip is characterised by stratospheric PV values that come down to about the 400 hPa level compared with a tropopause level of the ambient flow at ~ 300 hPa (see Fig. 3.23a). Again the strip rotates and breaks into two vortices.

Water vapour images of stratospheric vortices exhibit often additional small scale structures (see, e.g., Appenzeller and Davies 1992, Appenzeller 1994, Wirth et al. 1997, or see again Fig. 3.1). For example a common feature is a white spot, i.e. a moist structure, in the center of the vortex, or white filaments next to the dark filaments that connect individual vortices. In addition in Fig. 3.1 there are also two darker small scale anomalies of high radiance west and east of the white vortex center. In the SQG and the PE simulations the center of the vortex is characterised merely by high θ or PV values exhibiting little structure in the interior.

Wirth et al. (1997) studied the additional small scale structures in the observational data by simulating the evolution of a finite temperature anomaly with a quasi-geostrophic model akin to the simulations presented in section 3.4. They calculated the ageostrophic vertical wind and used it to simulate water vapour images. They argue that water vapour images represent a combination of the horizontal advection of initial moisture anomalies and the creation of additional moisture anomalies which are generated by the vertical motion at the tropopause level. Their analysis shows that smaller scale structures can be linked to the

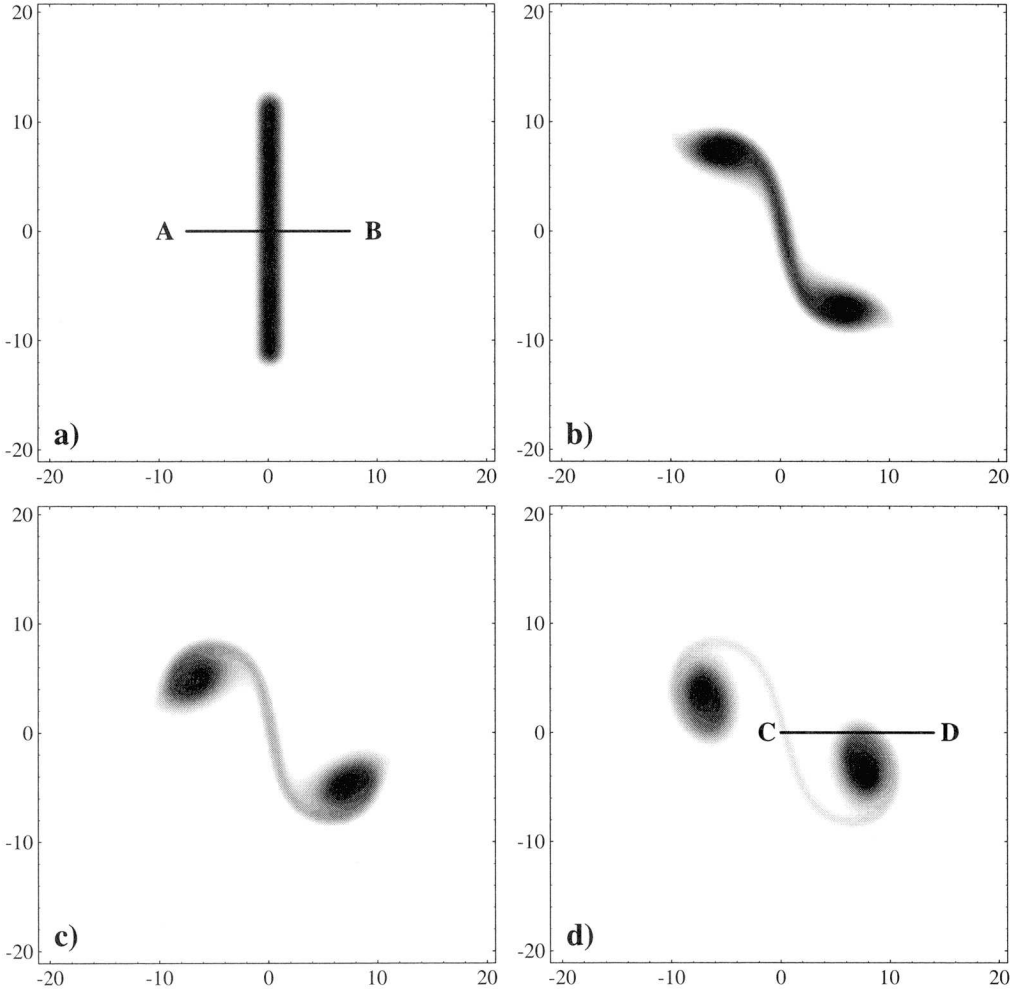


FIG. 3.21: Nonlinear evolution of a finite PV intrusion with PE dynamics on an f -plane. The length of the anomaly is ~ 3000 km and the width ~ 250 km. The evolution corresponds to 2 (panel b), 3 (panel c), and 4 days of integration (panel d). Displayed is PV on the 315 K isentrope.

vertical motion.

Here the PV structure at different levels is of interest. It can be argued that the flow is quasi two-dimensional and this accounts for the high correspondence between the SQG and PE simulations. The dynamically dominant part is captured by the upper high PV values, and at lower levels it is supposed that the structures are “passively advected” by the wind field of the main PV portion of the anomaly. In Fig. 3.22 the PV distributions at 300 (panel a) and at 400 hPa (panel b) are compared. The distribution at higher levels exhibits similar structures as the SQG analogue, the PV distribution at the lower edge of

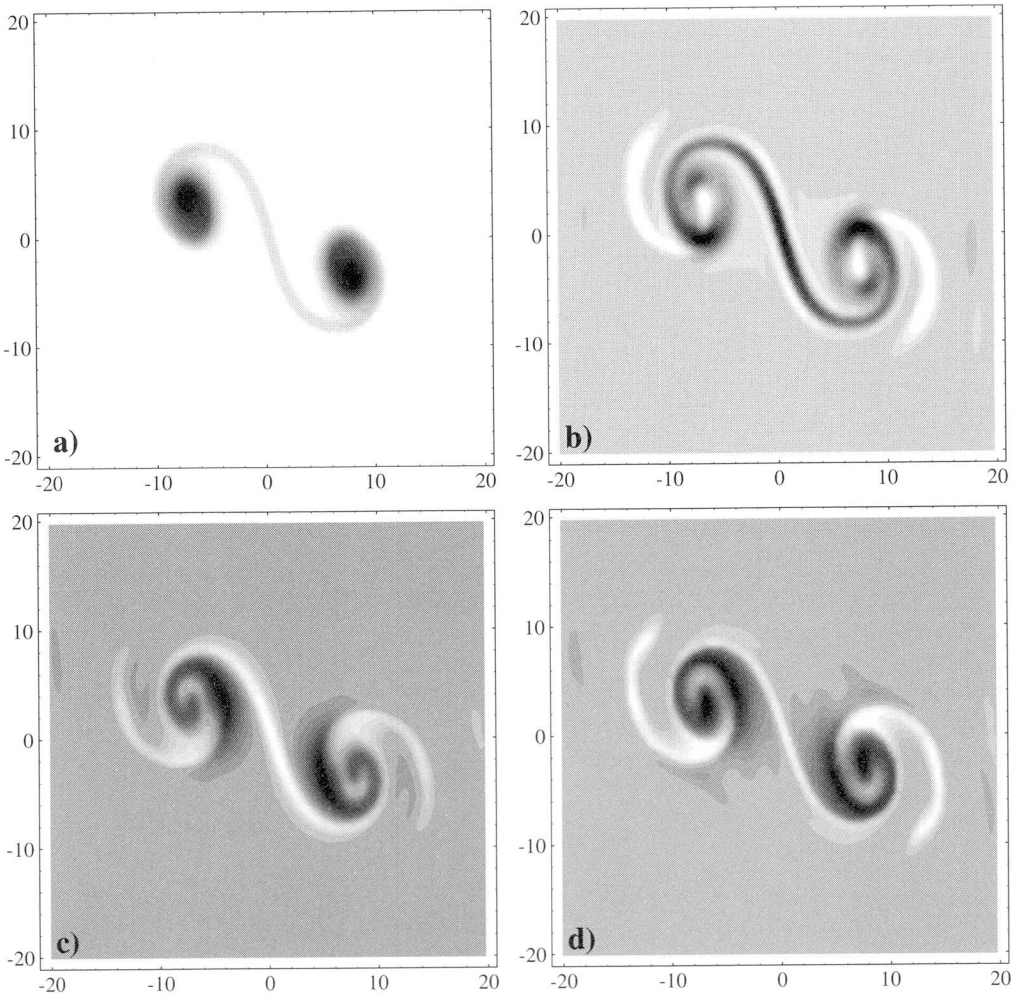


FIG. 3.22: Structure of a stratospheric intrusion after 4 days of integration. Shown is PV on the 300 hPa (panel a) and 400 hPa (panel b) level. In the lower panels the vertical displacement on 400 hPa (see text) is displayed for 48 (panel c) and 72 hours (panel d). Dark regions correspond to ascending, bright regions to descending air.

the anomaly exhibits much fine scale structures. Here the thin filament of stratospheric air (high PV values) is rolled-up around the vortex core. This results in reduced PV values in the center of the vortex, and two distinct small-scale PV anomalies right next to the center. These features are very similar to the observed ones (see again the water vapour image at the beginning of this chapter, Fig. 3.1). Note also the white thin filaments on each side of the high PV filament connecting the two vortices.

The occurrence of small scale structures induced by vertical motion is demonstrated by a

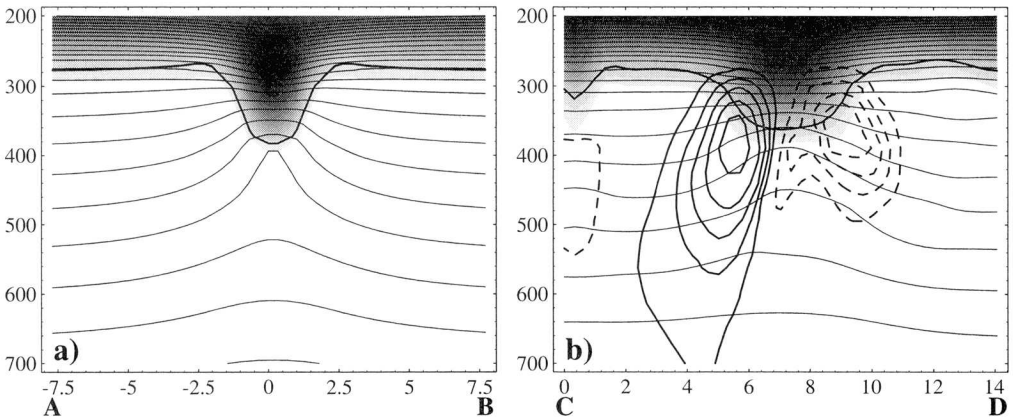


FIG. 3.23: Section for the initial PV configuration (panel a) and after 4 days as indicated by the line in Fig. 3.21. Displayed are PV (shaded) and potential temperature (thin lines, spacing 2.5 K). In b) the vertical velocity is overlaid (spacing 25 Pa h^{-1} , dashed lines for downward motion).

calculation of the “vertical displacement”: The origin of each air parcel is calculated with a Lagrangian method, and the vertical displacement over a specific time interval is displayed. Air parcels that have been ascending or descending over a certain time interval, i.e. which are more likely of tropospheric or stratospheric origin can be identified. In the lower panels of Fig. 3.22 the displacement field on 400 hPa is shown. Dark regions correspond to ascending, bright regions to descending air. In panel c) (panel d) the integration interval is 48 hours (72 hours), maxima in ascend and descend are 33 (33) and 47 hPa (56 hPa), respectively. In agreement with the PV distribution the center of the vortex corresponds to ascending air. Note also that the connecting filament between the two vortices is a region of descending air.

3.6 Discussion

The comparison of the nonlinear evolution of interior PV-bands and surface θ -bands indicates that the major dynamical characteristics of PV bands are already captured by the analogous temperature anomalies. The instability of the latter anomalies is strongly influenced by the ambient flow (barotropic and baroclinic shear) and by the shape of the anomaly itself. It has to be noted that for example during a frontal wave development these parameters can significantly change in time and are not fixed as in the present linear instability analysis.

The shape of the anomaly has as well a significant influence on the nonlinear phase of the development. For example the nonlinear development of a θ -band within a barotropic, unshered ambient flow indicates that irreversible processes take place at the boundary of the forming vortices. These irreversible processes are manifested by alternating high and low temperature values, and the mixing of high and low θ air is stronger for a temperature anomaly with a weak temperature gradient (compare Fig. 3.14 with Fig. 3.15).

PE simulations of interior PV anomalies indicate that the flow field associated with

the major part of the anomaly results in an instability process akin to the two-dimensional analogue. The development of the PV structure at the vertical boundary of the anomaly can be understood as passively advected by the flow field corresponding to the large amplitude values of the anomaly. Consequences are small-scale structures at the vertical boundary of the anomaly which exhibit a high resemblance to the observed structures in the water vapour images.

Leer - Vide - Empty

Chapter 4

Case Study of a Frontal Wave Cyclone

4.1 Introduction

In recent years much research effort has been invested in the study of midlatitude cyclogenesis, and in particular in examining rapid developing cyclones (Orlanski 1968, Sinton and Mechoso 1984, Moore and Peltier 1987, Kuo and Reed 1988, Reed et al. 1988, Whitaker et al. 1988, Thorncroft and Hoskins 1990, Joly and Thorpe 1990a, Joly and Thorpe 1990b, Schär and Davies 1990, Uccellini 1990, Reed et al. 1992, Malardel et al. 1993, Polavarapu and Peltier 1993, Bishop and Thorpe 1994a, Bishop and Thorpe 1994b, Appenzeller and Davies 1996, Bishop 1996a, Bishop 1996b). The approaches used to develop our understanding of these atmospheric phenomena include undertaking both idealised and case studies, and the latter can be divided into observational and simulation studies. These approaches have influenced each other constructively. For example the case study approach has been the starting point for further idealised investigations, and the development of theories has prompted verification studies by diagnosis with observed data. A major difference in these approaches lies in the fact that in idealised studies of extratropical cyclogenesis the baroclinic instability of a basic state has often been studied, whereas in a case study approach initial structures and disturbances, their development and contribution to the dynamics have been of central interest. In general the initial disturbances are large amplitude and one focus has been the quantitative evaluation of their effects upon one another via vertical and/or lateral interaction.

The PV perspective provides a framework for relating the two approaches. Here we undertake a case study of a frontal wave event from this perspective and examine a hypothesis for its formation. Secondary frontal cyclones are an important forecasting problem, especially as they occasionally deepen explosively into full blown storms. A summary of several possible dynamical mechanisms involved in such a cyclogenetic event can be found in Appenzeller and Davies (1996). These mechanisms include (i) in situ development of the surface front, (ii) the instability of a low-level PV band or surface θ -band (via the interaction of two wave trains at the edges of the band, see also chapter 3), (iii) an upper-level PV anomaly overtaking the surface zone of enhanced baroclinicity and (iv) specific interactions of these anomalies, e.g. the interaction of two vertically aligned wave trains. These dynamical processes can, and are, also altered and complicated by the release of latent heat of condensation. The

diabatic processes can generate and annihilate major portions of PV and these diabatic PV changes¹ in turn have an effect on the wind and temperature distribution via the invertibility property and can thereby be important for the interaction with other PV structures and/or these diabatically produced PV may significantly contribute to the total circulation.

Contributions to the study of these various mechanisms related to the development of frontal waves using the idealised or the case study approach come from e.g. Schär and Davies (1990) where the instability of a surface warm band on the warm side of a baroclinic zone has been investigated and studies of the instability as a self-development of low-level PV-bands (shear-lines) e.g. Joly and Thorpe (1990a) and Malardel et al. (1993). The prefrontal low-level band of enhanced PV can be viewed as being induced by condensation in the frontal ascent region. The corresponding shear lines are unstable to barotropic or internal baroclinic instabilities via the Charney and Stern (1962) instability criterion on length scales and time scales comparable with the observed ones. Other studies focus on the interaction of upper and lower PV structures (Hoskins et al. 1985), and consider a mechanism whereby an isolated upper-level anomaly induces a localised wave-like perturbation near the surface, and the further interaction of these anomalies. It has been demonstrated (Uccellini et al. 1985, Mattocks and Bleck 1986, Berrisford 1988, Whitaker et al. 1988, Bleck 1990, Davis and Emanuel 1991, Reed et al. 1992) that this mechanism is in fact very often an important factor of cyclogenesis. A related study is that of Davies and Bishop (1994), who considered the vertical interaction and in phase development of two Eady edge waves. It has been noted (Appenzeller and Davies 1996) that the aforementioned mechanisms have not to be exclusive and in fact it is often a combination of these mechanisms, or their sequential contribution that accounts for the development.

Many investigators have studied the influence of moisture on the intensity of the mature cyclone² (Boyle and Bosart 1986, Whitaker et al. 1988, Kuo and Reed 1988, Reed et al. 1992, Davis et al. 1993, Rossa 1995). For diabatic processes it is important to understand the evolution of the vertical motion field during the life cycle of cyclones. Wernli (1997) studied trajectories to identify flow structures with certain vertical motion characteristics. He applied an objective selection criterion on a large ensemble of trajectories and thereby identified coherent ensembles of trajectories (so called CETs) that correspond to prefrontal moist ascending air, cf. the warm conveyor belt. Another study based on trajectory calculations is that of Rossa (1995). He performed a PV-tower analysis to study the origins of the high PV values in a vertically coherent cyclone.

In the PV framework a study of the contribution of the different PV elements to the frontal wave development should include a description of the key PV structures that are involved in the development and a quantitative diagnosis of both the generation mechanisms of PV disturbances and the cause effects of isolated portions of PV structures. Here partial attempt is made for one case study using various diagnostic tools.

The chapter is organised as follows: In section 4.2 the structure of the PV elements is compared for both the analysis fields and a simulation of the event with the EM. A \mathbf{Q} -vector

¹Haynes and McIntyre (1987) have shown that any diabatic heating away from boundaries simply acts to rearrange PV, preserving its mass-weighted volume integral.

²In fact in the last century, based on the work of Espy, it was believed that cyclones grow to a large degree due to release of latent heat near the cyclone.

diagnosis is applied to the observational data set in section 4.3. Also in this section we study the contribution of latent heat release to the low-level PV band. Diabatic processes contributing to the dynamics are further studied by a comparison of the moist simulation with dry simulations (section 4.4). In section 4.5 a method is presented to compare the time scale of the diabatic PV rate with the time scale of the adjustment to a balanced flow. Key PV elements are defined in section 4.6 and we estimate their contribution to the dynamics with the inversion technique. Sensitivity studies starting with various upper-level PV distributions are presented in section 4.7. Such an investigation can further help elucidate the role of the sub-synoptic PV elements on the dynamics and point to the possible interaction mechanism of upper and lower structures. The results are discussed in section 4.8 with a special emphasis on the results of the idealised studies of the last chapter.

4.2 PV Structures of a Frontal Cyclogenesis Event

The case considered here is that of a rapid cyclogenesis that occurred in October 1989. The PV morphology of this case has been described in detail by Appenzeller and Davies (1996) using the initialised analysis data from the ECMWF. They examined the relationship of the PV structures to existing hypothesis for the genesis of a frontal cyclone. It was noted that the synoptic evolution could be split into two phases. Phase I (until 00 UTC on 21 October) is characterised by a quasi-stationary parent low (L_M) situated south of Iceland and a formation of an undulation (L_S) on the associated cold front (Fig. 4.1). In the second phase two waves (L_{S1} and L_{S2}) develop, and L_{S1} matured rapidly to form a sub-synoptic cyclone centered off the Norwegian coast.

From a PV perspective the first phase is characterised by an evolution of an elongated prefrontal structure of enhanced PV value (maximal amplitude ~ 1.5 pvu) out into the Atlantic. This anomaly intensified in the second phase into a richly structured PV band with a length of ~ 2000 km and a width of ~ 400 km. Its eastern tip rolled-up and cut-off yielding a shallow PV anomaly at the secondary cyclone and became vertically aligned with the upper-level anomaly P_{S2} . A comparison of the hand analysed surface charts with the front position from the weather services and the low-level PV structures of the ECMWF locates the frontal waves at the PV maxima.

The upper-level development is dominated by a large-scale trough, and the PV anomaly has distinctive sub-synoptic features, see Fig. 4.2. These structures can be tracked with a trajectory calculation. Fig. 4.3 shows the envelopes of the anomalies P_{S1} and P_{S2} traced back from 12 UTC on the 21 October to 18 UTC on the 20th (panel b) and than further back by another 18 hours (panel a). It demonstrates that P_S breaks into P_{S1} and P_{S2} separated by some ~ 1500 km at 18 UTC on the 20th, and in the following development the two elements can be observed to merge.

There was an in phase development of the upper structures with the low-level flow. For example at the mature phase of the frontal wave cyclone the sub-synoptic upper-level anomaly labeled with P_{S2} is collocated with the secondary surface cyclone.

For this case several simulations were performed with the mesoscale model, and the simulations are compared with the ECMWF initialised analysis fields. Note that the operational

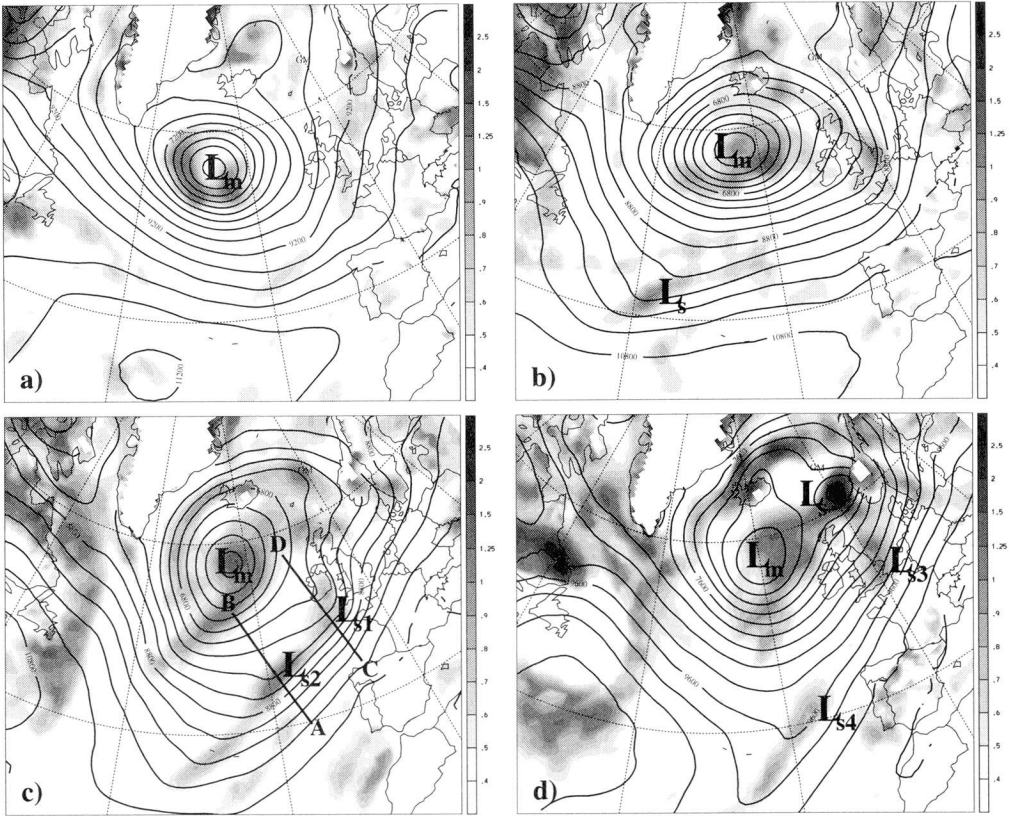


FIG. 4.1: ECMWF initialised analysis of a frontal wave development over the Atlantic for 06 UTC 19 October (panel a), 00 UTC 20 October (panel b), 18 UTC 20 October (panel c), and 12 UTC 21 October (panel d). The displayed fields are potential vorticity at 850 hPa (shaded, irregular spacing) and geopotential at 900 hPa (spacing $400 \text{ m}^2 \text{ s}^{-2}$).

version of the global model at that time was the T106/L19 version with a horizontal resolution of $\sim 150 \text{ km}$ in midlatitudes and the resolution of the EM is about 56 km in the same region.

The simulated 54 hour fields, starting at 06 UTC on the 19th are shown in Fig. 4.4 and Fig. 4.5. The main differences between the simulation and the ECMWF-analysed pattern are (at lower levels) (i) a reduced width of the low-level PV band in the EM simulation, (ii) higher maximum PV values for the simulated PV anomaly, and therefore (iii) stronger PV gradients at the lateral boundaries of the PV band, (and at upper levels) (iv) finer scale structures, (v) more coherent vertical structure of the mother cyclone during the whole development (vi) a structure that corresponds even closer to the “cyclonic” life cycle simulation of Thorncroft et al. (1993), and (vii) at the time when the secondary cyclone reached maturity a strong elongated PV anomaly aloft aligned parallel to the surface front.

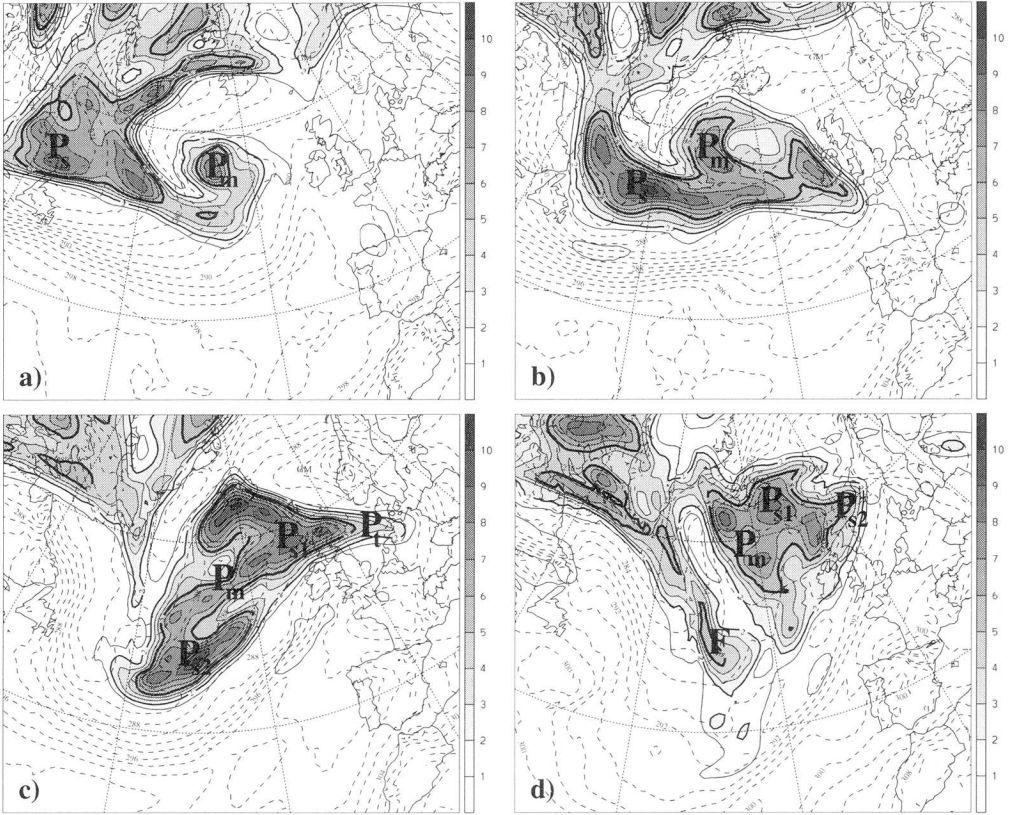


FIG. 4.2: ECMWF initialised analysis for the same time sequence as in Fig. 4.1. The displayed fields are potential temperature field at 850 hPa (dashed lines), and potential vorticity on the 310 K isentropic surface (shaded). Contour spacing is 2 K for potential temperature and 1 pvu for potential vorticity. (The thick line corresponds to the 2 pvu and the bold to the 5 pvu isoline.)

The differences stem in part from the different resolutions of the two models. This can be further illustrated using a passive advection of the upper-level PV structure of the ECMWF with the wind fields of the ECMWF but on the grid of the mesoscale weather prediction model³ (see Fig. 4.6). In such an experiment the advected PV distribution exhibits similar small scale structures as in the simulation.

Now consider the sensitivity of short range forecasts to the upper-level PV pattern and whether there is strong interaction of the sub-synoptic upper-level and low-level features. To this end simulations starting at later times than the reference simulation were performed.

³An other technique which has been used to advect PV structures is passive contour dynamics on isentropic surfaces (e.g. Norton 1994). There it can be observed that especially in PV streamers or cut-off systems very small-scaled structures may evolve. Here such smaller scaled structures can only be resolved down to the resolution of the mesoscale model.

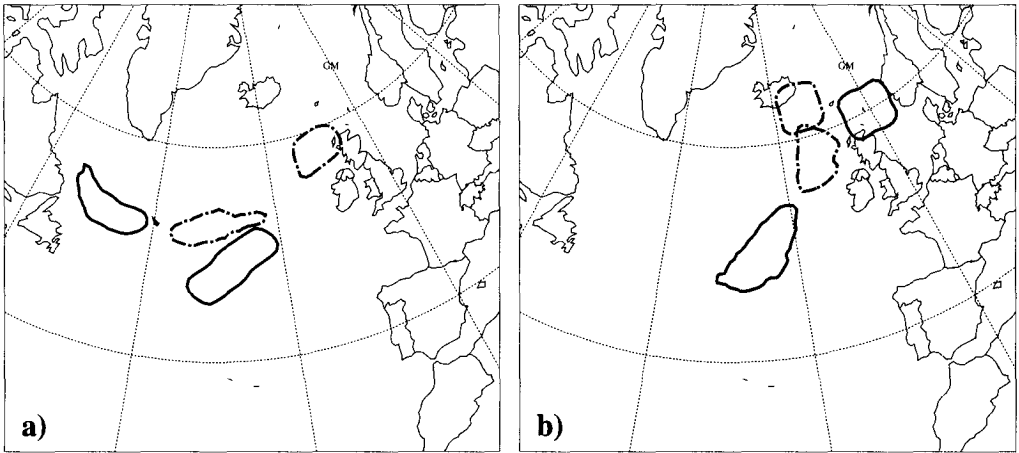


FIG. 4.3: The 18 hour backward traced envelope of the upper-level PV-anomaly labeled P_{s1} and P_{s2} in Fig. 4.2 from 18 UTC to 00 UTC on October 20 (panel a) and from 12 UTC October 21 to 18 UTC October 20 (panel b). The envelope of P_{s1} is indicated by a dashed-dotted line and P_{s2} by a continuous line.

There was no major difference in the forecast of the secondary cyclone.

Table 4.1 gives the central pressure value and the location of the cyclone at 12 UTC on the 21 October for the various simulations and the observation. It demonstrates that in the simulations the secondary cyclone is located further north-east.

We conclude that the limited area model can produce smaller scale structures, and that the prediction of this particular event was accurate. The reduced width of the low-level PV band is related to the increase in the resolution in the simulation. The baroclinicity is in both cases about the same, i.e. a scale contraction as observed in the PV distribution is not present in the potential temperature field. The upper-level structures exhibit some differences between the simulation and the analysis but the structures which are probably most important for the low-level dynamics are well represented in the simulation. The forecast secondary cyclone has been remarkably well predicted in location and amplitude and therefore sensitivity tests may be meaningful.

		observation	18 h forecast	36 h forecast	54 h forecast
secondary cyclone	p	968 hPa	967 hPa	970 hPa	965 hPa
	long	1.0°E	3.5°E	2.5°E	3.5°E
	lat	61.5°N	60.5°N	61.5°N	62.5°N
mother cyclone	p	965 hPa	965 hPa	960 hPa	960 hPa
	long	19.5°W	19.5°W	18.5°W	16.5°W
	lat	57.5°N	58.0°N	58.5°N	59.0°N

TABLE 4.1: Central pressure and location of the secondary surface and mother cyclone at 12 UTC on 21 October for the observation, a 18, 36 and 54 hours integration.

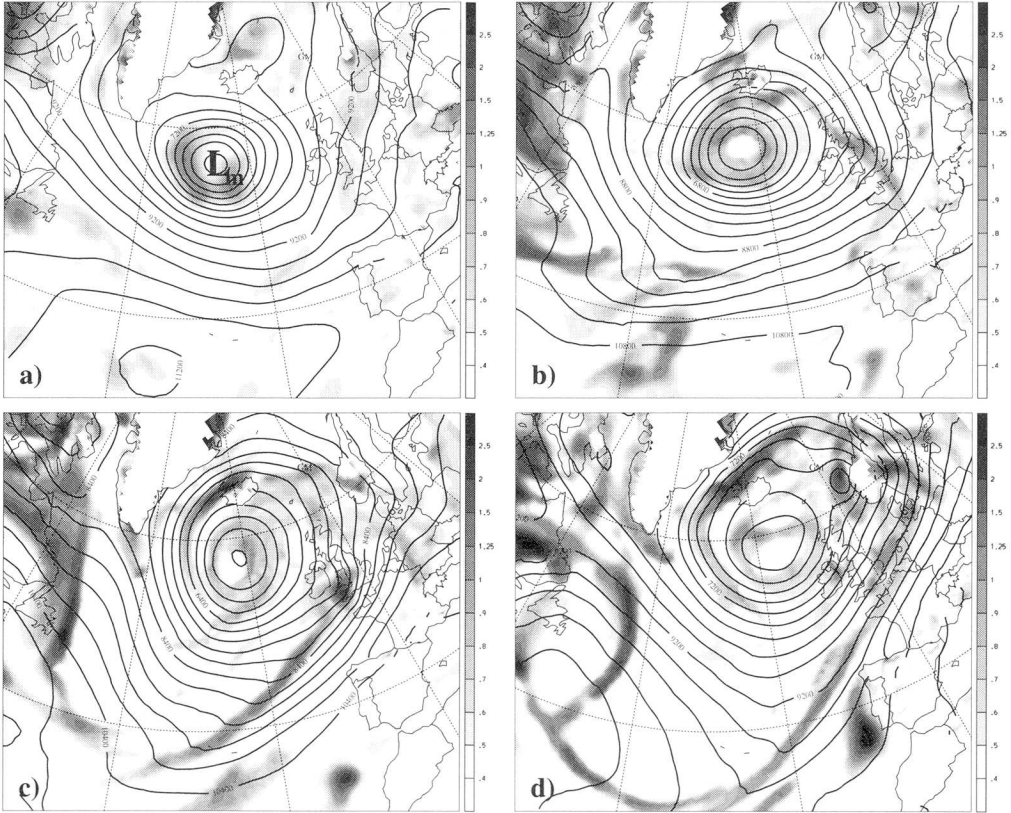


FIG. 4.4: The analogue of Fig. 4.1 but now derived from the 54 hour forecast with the EM started at 06 UTC on 19 October.

4.3 Diabatic Processes and the Generation of the Low-Level PV Anomaly

4.3.1 Model Derived Precipitation

The high PV values of the prefrontal anomaly are linked with a region of high values of relative humidity and vertical velocities, see Fig. 4.7. The relative humidity pattern at 18 UTC consists of an elongated band of intense moisture near the front, and strong upward velocities $\sim 20 \text{ hPa h}^{-1}$ with a maximum of $\sim 50 \text{ hPa h}^{-1}$ at the eastern tip of the band.

The precipitation associated with this band is shown in Fig. 4.8. Displayed are the six hourly accumulated precipitation valid for 18 UTC on October 20 (panel a) and 12 UTC on October 21 (panel b). During the development there were maximum values of $\sim 25 \text{ mm}(6\text{h})^{-1}$ along the surface front. At 18 UTC on October 20 the maximum precipitation occurs in the south western part of the band. The precipitation near the undulation L_{S1} which developed

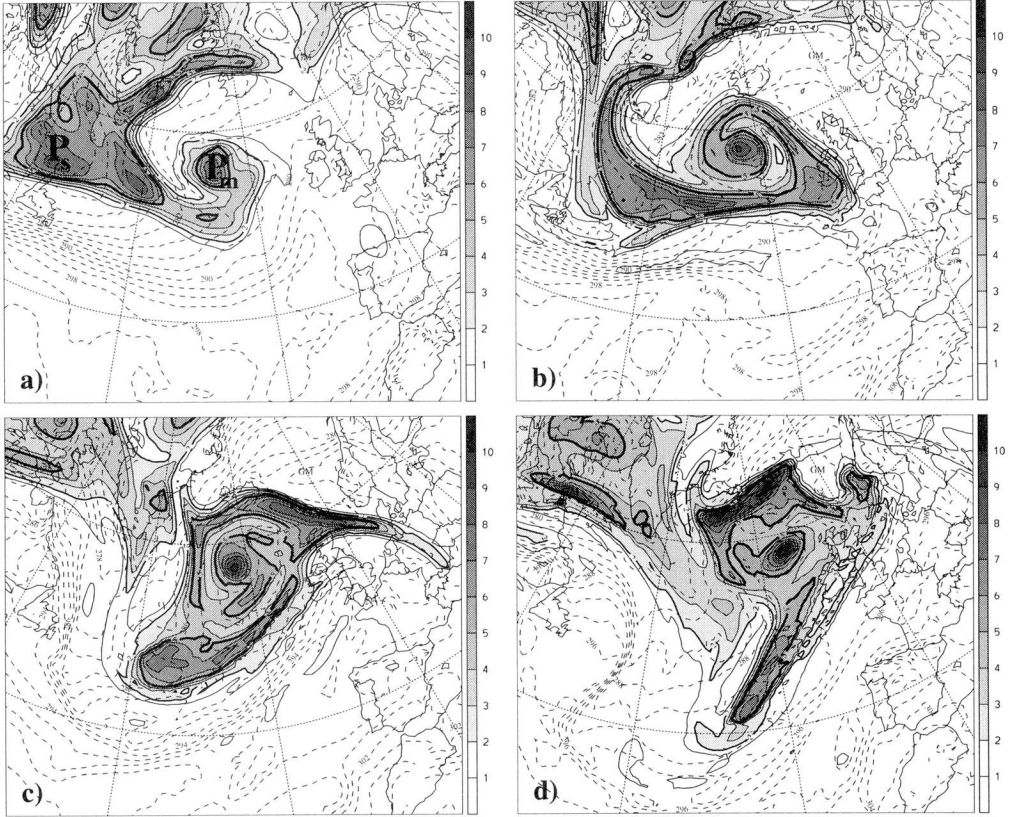


FIG. 4.5: The analogue of Fig. 4.2 but now derived from the 54 hour forecast with the EM started at 06 UTC on 19 October.

into the secondary cyclone was weaker.

4.3.2 Q -Vector Analysis

The Q -vector pattern on 850 hPa is displayed in Fig. 4.9, superimposed is the potential temperature. At 18 UTC 20 October there are two identifiable frontogenous regions along the cold front. One coincides with the region of the undulation L_{S2} , and the other is further south-west. Also the Q -vectors are strongly divergent near the undulation L_{S1} – indicative of the dynamical forcing of vertical velocity. At 12 UTC 12 October there is again Q -vector forcing near the undulations L_{S3} , L_{S4} , and L_S .

4.3.3 Diabatic Heating and PV Rates

The results of the two previous subsections indicate that strong diabatic processes occurred along the front system in the vicinity of the PV band. Here we examine the impact of

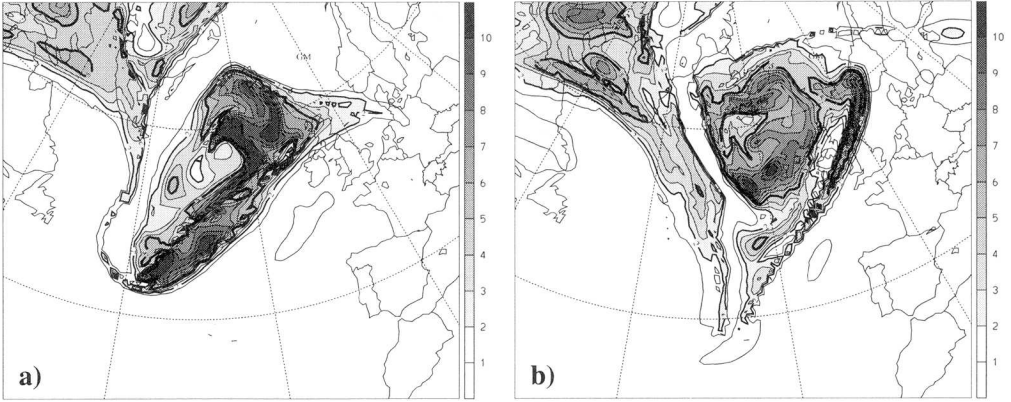


FIG. 4.6: Passively forward advected PV distribution on the 310 K isentropic surface by 18 hours with the analysis wind fields valid for 18 UTC October 20 (panel a) and 12 UTC October 21 (panel b).

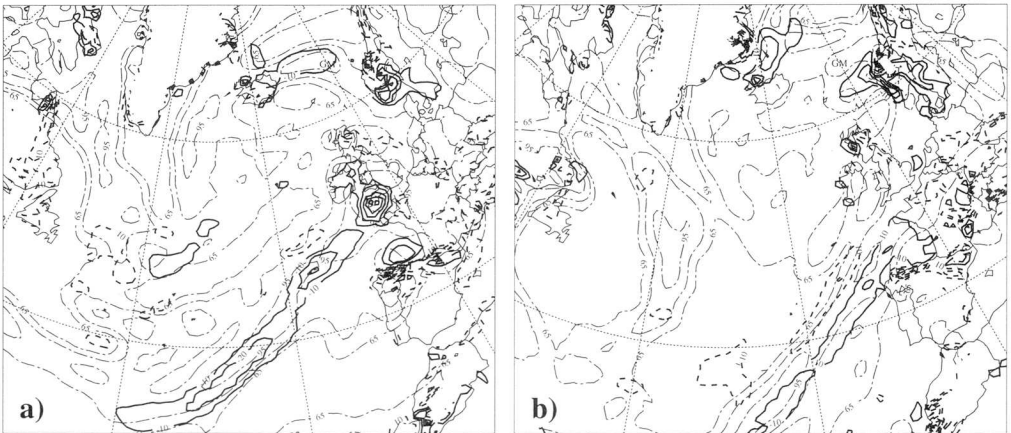


FIG. 4.7: Vertical velocity (spacing 10 hPa h^{-1} , upward motion continues lines, downward motion dashed lines) and relative humidity (shaded for values $\geq 80\%$, dashed-dotted contours for 65, 80 and 95%) on 850 hPa valid for 18 UTC October 20 (panel a) and 12 UTC October 21 (panel b).

the condensational heating on the development of the PV structures and the frontal-wave. Diagnostic calculations of the latent heating rate and the PV tendency due to condensation based on equation (2.7) and (2.8) prove helpful in linking the diabatical condensation to the dynamics. Fig. 4.10 shows cross-sections along the two lines indicated in Fig. 4.1. The displayed fields are the condensational heating and PV rate (upper panels) and the relative humidity, the PV and the potential temperature (lower panels) calculated from the ECMWF analysis fields. At the south-western section maximal heating values are $\sim 1 \text{ K h}^{-1}$ and the region where significant heating occurs extends from 900 to 550 hPa. The heating region

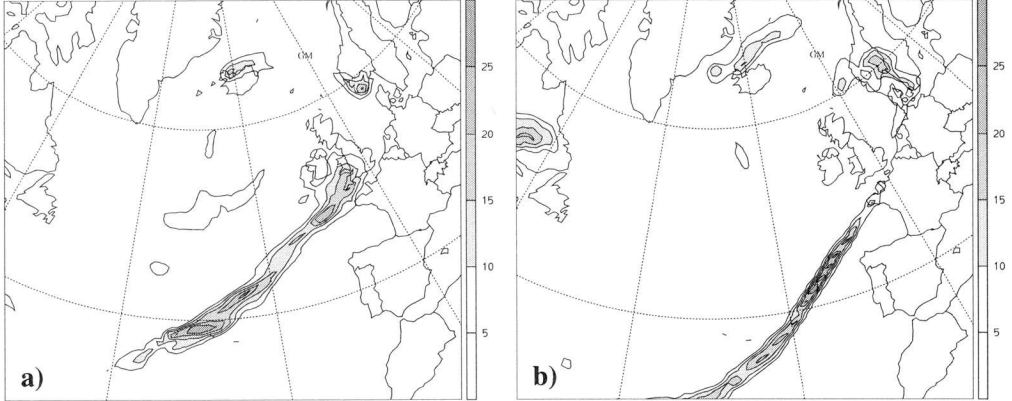


FIG. 4.8: Six hour accumulated resolved-scale precipitation for a simulation with the EM (spacing is $5 \text{ mm}(6\text{h})^{-1}$) valid for 18 UTC October 20 (panel a) and 21 UTC October 21 (panel b).

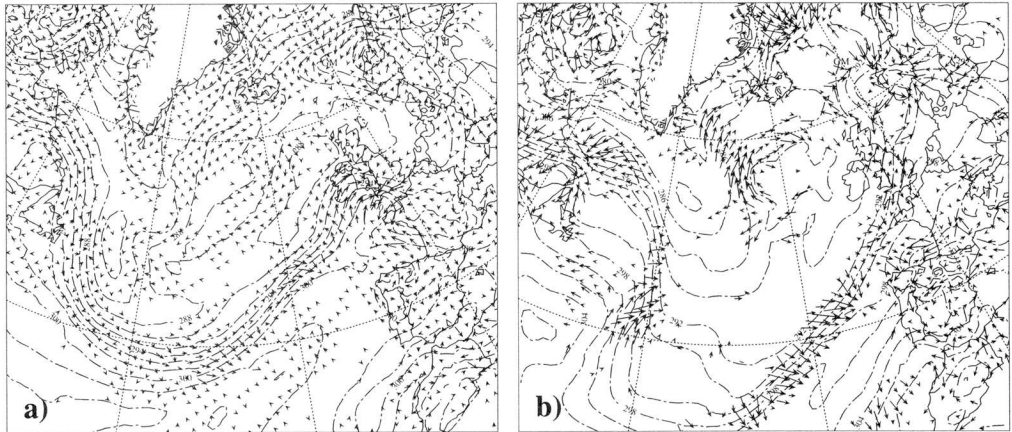


FIG. 4.9: Potential temperature and \mathbf{Q} -vector fields at 800 hPa derived from ECMWF analysis data, valid for 18 UTC October 20 (panel a) and 21 UTC October 21 (panel b). Dash-dotted lines denote potential temperature (contour interval 2 K). \mathbf{Q} -vectors are shown only if their length exceeds a threshold value.

coincides with the location of the low-level PV band. The resulting PV rates show (as expected) a dipolar structure with a positive maximal amplitude of 0.2 pvu h^{-1} at 950 hPa and a negative amplitude of 0.15 pvu h^{-1} at ~ 600 hPa. The eastern section is markedly different. The center of the PV band can be found at 700 hPa. It is connected with a PV anomaly close to the surface. Here there are two heating centers to the north and south of the PV band. Both exhibit much weaker heating values ($\sim 0.6 \text{ K h}^{-1}$) and PV rates ($\sim 0.05 \text{ pvu h}^{-1}$) than those values near the undulation L_{S2} . This smaller diabatical heating values correspond well with the model precipitation pattern.

From these considerations we expect that the PV band is only seemingly stationary at

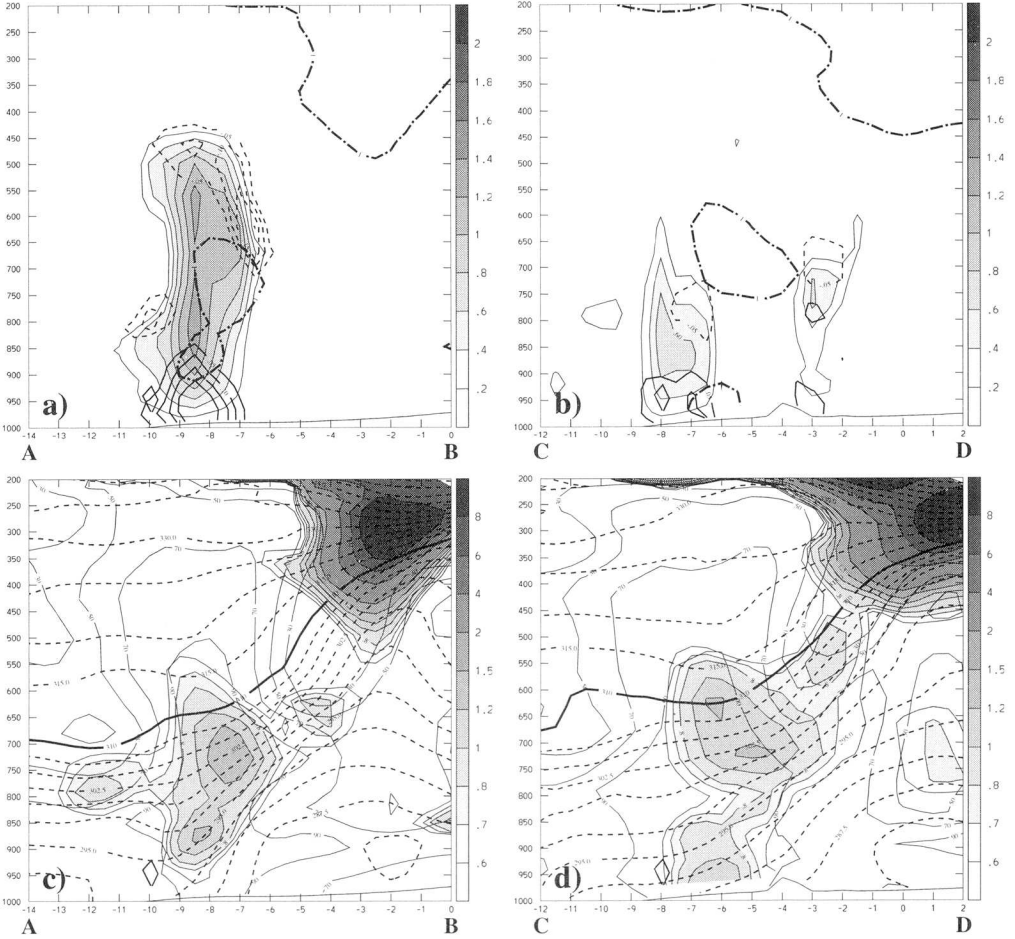


FIG. 4.10: Cross sections at 18 UTC 20 October along the lines indicated in Fig. 4.1. The displayed fields are (in the upper panels) diabatic heating rate (shaded, spacing 0.2 K h^{-1}), diabatic PV-rate (positive values solid lines, negative values dashed lines, spacing 0.05 pvu h^{-1} , zero line omitted) and superimposed is the 1 pvu isoline, and (in the lower panels) potential vorticity (shaded, irregular spacing), potential temperature (dashed lines, spacing 2.5 K for values $\leq 310 \text{ K}$, 5 K for values $\geq 310 \text{ K}$, and thick line indicates the 310 K isoline) and relative humidity (thin lines, spacing 20%).

$\sim 750 \text{ hPa}$. It is continuously destroyed at the top of the band and generated from below. It is a combination of PV generation and destruction with a vertical circulation near the front which gives rise to this PV structure which is present for more than two days at a specific level. This aspect is further highlighted in the next subsection.

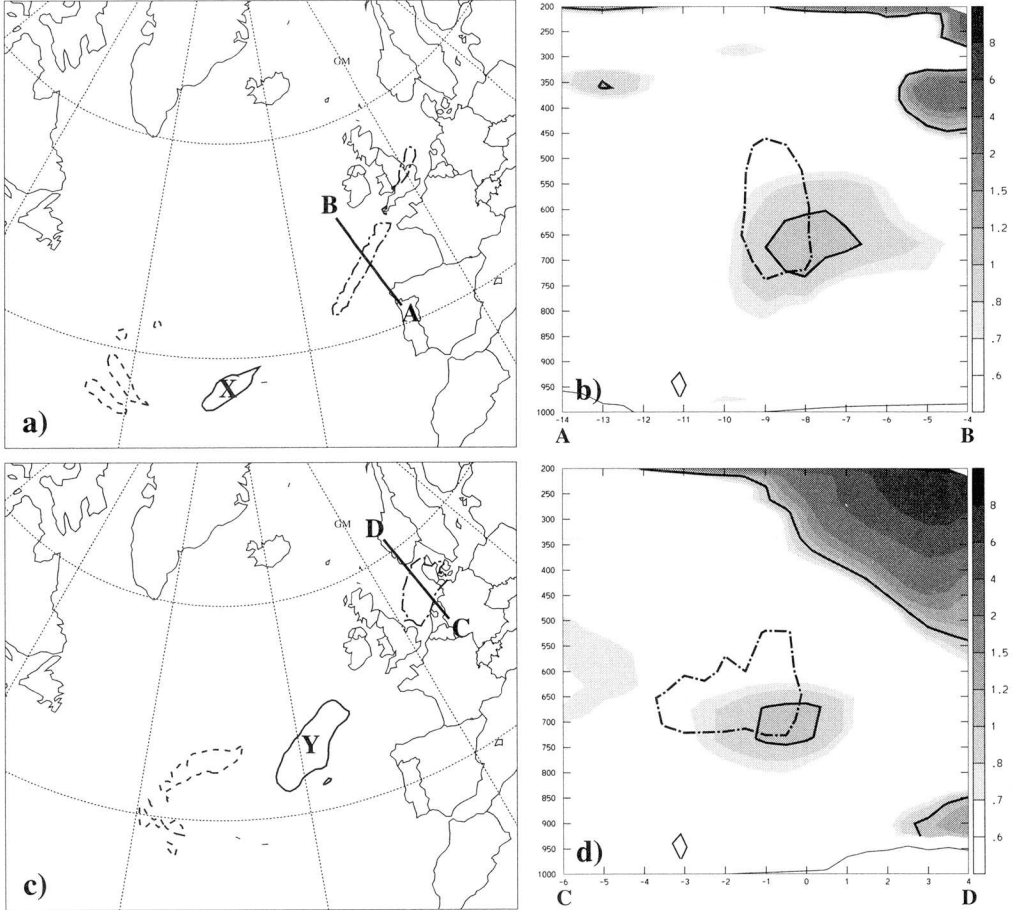


FIG. 4.11: Trajectory analysis of the low-level PV band. Displayed are the envelopes of the ensembles for the three regions **X**, **Y** and **Z** (left panels) and in sections (right panels) PV (shaded, 1 pvu isoline overlaid) at the end time of the trajectory calculation and superimposed the forward advected regions (dash-dotted).

4.3.4 Lagrangian Trajectory Analysis of the Low-Level PV-Band

Here a kinematic analysis is provided of the PV-band. Air parcels are traced forward and backward in time, from 18 UTC on October 20, i.e. the time before maximum intensification of the surface cyclone. The PV anomaly itself is segmented into three regions, each containing a local PV maximum. From the ensemble of trajectories we select those which had initially (i.e. at the starting time of the forward and backward trajectory calculation) PV values that exceed 0.75 pvu. This threshold value is well above the typical PV value for the lower troposphere. For each segment this criterion defines portions of the PV band at 18 UTC October 20 that are labeled with **X**, **Y**, and **Z** from south-west to north-east.

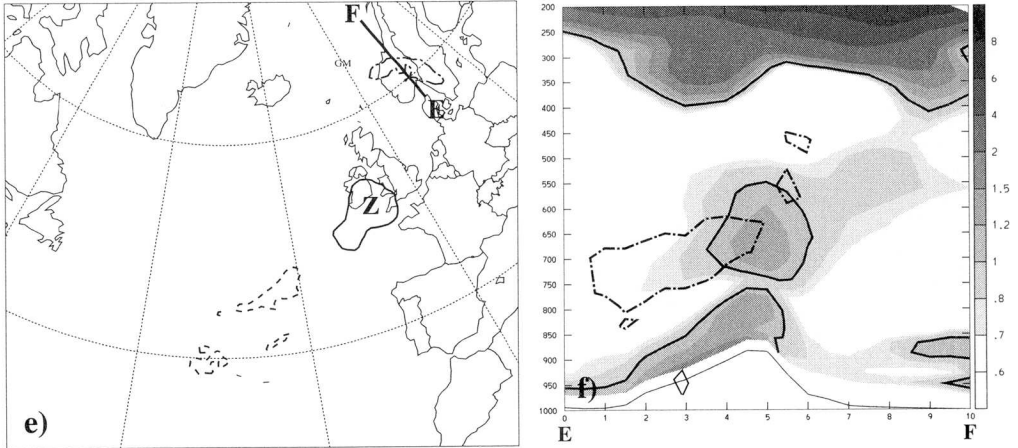


FIG. 4.11 (cont.)

In Fig. 4.11 the envelopes of the so defined ensembles are displayed. Also shown are sections through the forward traced envelopes of **X**, **Y**, and **Z** superimposed on the observed PV distribution at 12 UTC on October 21.

In the horizontal the location of the forward advected region corresponds well with the observed PV distribution (except of the western part of the low-level PV band). An envelope of the central, the backward and forward points for the western most part of the band, **X**, is shown in panel a. In the second phase the envelope becomes more elongated demonstrating the deformation acting to increase the strength of the front at this stage of the development. The length to width of the other two regions, **Y** and **Z** (panel c and e), remains more or less constant. Note that the PV anomaly at 12 UTC 21 October near the undulation labeled with L_{S4} in Fig. 4.1d does not correspond to the 18 hour forward advected anomaly **X**, i.e. this undulation is linked to a PV anomaly that has been generated by diabatical processes and the advective component of this low-level PV structure is marginal. These diabatical processes in turn can be linked to the strong precipitation as depicted in Fig. 4.8. Vertically the air parcels are advected to higher altitudes than the observed PV structures at the later time by about 100 hPa in 18 hours (panels b, d, and f). This is further demonstrated by a calculation of the ensemble mean of some characteristic quantities (see Table 4.2).

From 18 UTC 20 October until 12 UTC 21 October the air parcels of the ensembles rise 100 – 200 hPa, the mean potential temperature rises by 4 – 8 K and water vapour reduces by 3 – 4.5 g kg^{-1} . Again strongest diabatic effects occur over the western part of the front.

4.4 Dry Simulations

It has been demonstrated that moist processes exerted a substantial influence upon the low-level PV structures. The latter have been presumed to be pivotal to frontal wave instability and the genesis of the sub-synoptic surface cyclone. To further address to this question dry

region X

t [h]	centre			mean and standard deviation of					
	long	lat	p [hPa]	θ [K]		Q [pvu]		q [g/kg]	
-18	-42.8	39.4	874 \pm 134	298.6	\pm 3.9	0.37	\pm 0.3	10.3	\pm 5.0
-12	-38.2	39.2	864 \pm 122	299.2	\pm 4.3	0.59	\pm 0.3	9.6	\pm 4.4
-6	-33.3	38.8	842 \pm 108	300.5	\pm 4.4	0.60	\pm 0.2	9.1	\pm 4.4
0	-28.1	38.9	794 \pm 94	301.3	\pm 4.5	0.85	\pm 0.1	7.9	\pm 3.2
6	-22.6	40.2	727 \pm 75	304.5	\pm 3.9	0.64	\pm 0.1	6.9	\pm 2.3
12	-16.7	43.0	660 \pm 58	307.1	\pm 3.7	0.53	\pm 0.2	5.3	\pm 1.5
18	-9.5	46.9	601 \pm 60	309.3	\pm 4.9	0.73	\pm 0.3	3.2	\pm 0.7

region Y

t [h]	centre			mean and standard deviation of					
	long	lat	p [hPa]	θ [K]		Q [pvu]		q [g/kg]	
-18	-34.6	42.3	898 \pm 82	292.6	\pm 5.4	0.33	\pm 0.4	8.3	\pm 3.3
-12	-30.2	42.9	869 \pm 89	295.2	\pm 5.4	0.52	\pm 0.2	8.3	\pm 2.8
-6	-24.8	43.6	825 \pm 99	298.0	\pm 5.8	0.80	\pm 0.3	7.7	\pm 2.3
0	-18.2	45.4	767 \pm 104	300.3	\pm 6.4	0.97	\pm 0.2	6.8	\pm 2.2
6	-10.5	48.4	715 \pm 102	301.9	\pm 6.6	0.76	\pm 0.2	5.1	\pm 1.9
12	-2.2	51.8	687 \pm 91	303.4	\pm 6.1	0.66	\pm 0.2	4.6	\pm 1.5
18	6.5	55.0	669 \pm 90	304.3	\pm 6.1	0.68	\pm 0.2	4.1	\pm 1.3

region Z

t [h]	centre			mean and standard deviation of					
	long	lat	p [hPa]	θ [K]		Q [pvu]		q [g/kg]	
-18	-26.7	43.7	898 \pm 102	291.4	\pm 4.4	0.27	\pm 0.4	7.1	\pm 2.8
-12	-21.4	45.0	868 \pm 112	294.0	\pm 4.0	0.45	\pm 0.3	7.4	\pm 2.7
-6	-15.0	47.4	821 \pm 117	296.4	\pm 5.3	0.64	\pm 0.3	6.8	\pm 2.7
0	-8.4	50.6	769 \pm 120	299.2	\pm 6.2	0.97	\pm 0.2	6.3	\pm 2.8
6	-1.9	53.9	719 \pm 127	300.0	\pm 7.1	0.87	\pm 0.3	4.4	\pm 2.0
12	4.4	57.1	685 \pm 148	301.5	\pm 7.5	0.77	\pm 0.4	3.6	\pm 2.0
18	9.7	60.1	633 \pm 147	302.9	\pm 7.7	0.63	\pm 0.3	3.0	\pm 2.1

TABLE 4.2: Mean values and standard deviations of the position (longitude, latitude, pressure p), potential temperature θ , potential vorticity Q , and specific humidity q every 6 hours of trajectory integration, for trajectory ensembles starting in region X, Y and Z. $t = 0$ corresponds to 18 UTC 20 October, negative times to backward, positive to forward trajectories.

simulations have been performed excluding diabatic processes due to condensation. The simulations commence

(a) in the first phase of the frontal wave development, after the production of the low-level PV band, and

(b) in the second phase before the eastern tip breaks off and rolls-up.

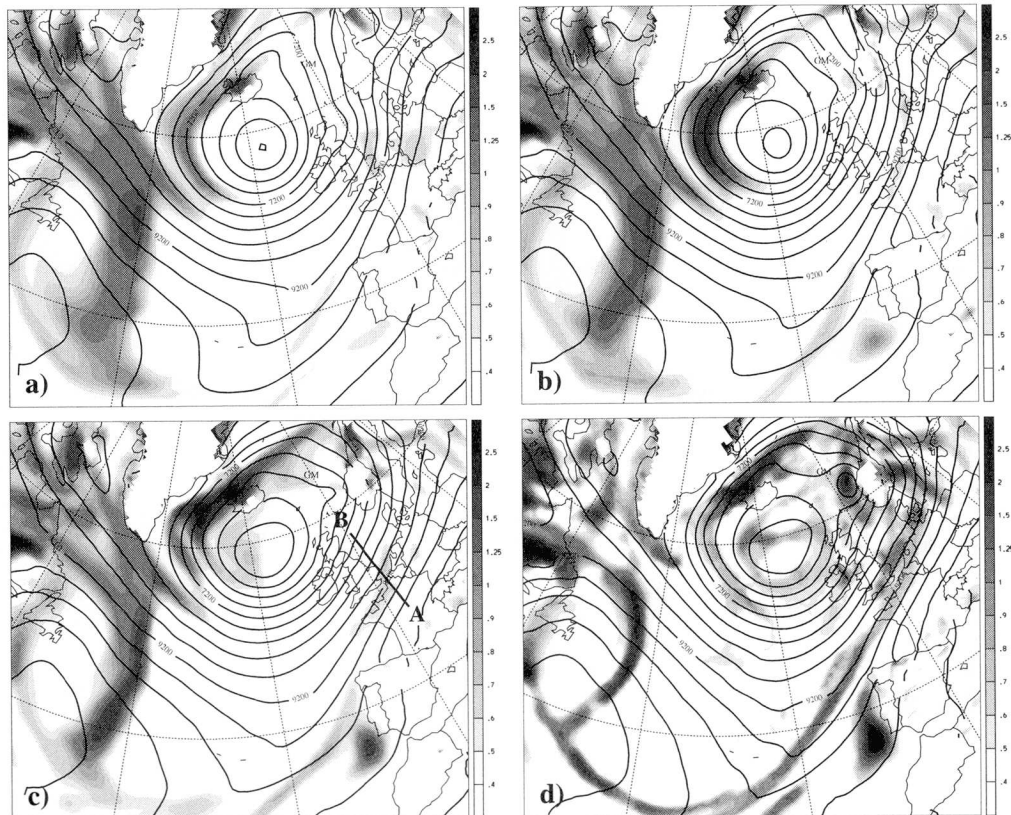


FIG. 4.12: The low-level PV-structure and the geopotential (shading and spacing as in Fig. 4.1) at 12 UTC on 21 October for a 54 (panel a), 36 (panel b), a 18 h dry simulation (panel c), and for the moist 54 h simulation.

These dry simulations show that the pre-existing PV-band, is advected to higher altitudes (about 100 hPa in 18 hours) by the strong frontal circulation. In the absence of further diabatic PV generation which previously served to continuously produce PV at the lower levels, the anomaly disappears from these levels on a time scale of $\sim 6 - 12$ hours (Fig. 4.12).

In the dry simulations the surface cyclone deepened only slightly once the diabatic production of PV had ceased. Fig. 4.13 shows the evolution of the surface pressure in the center of the cyclone after the switch from moist to dry dynamics. In the simulation where after 18 hours diabatrical effects have been turned off, the undulation decays on a time scale of about 12 – 18 hours, in the simulation where we switched after another 18 hours to dry dynamics, the central pressure parallels the reference simulation in the first 6 hours, but thereafter only a pressure drop of 2 hPa compared with one of 12 hPa in the moist and in the ECMWF fields could be observed.

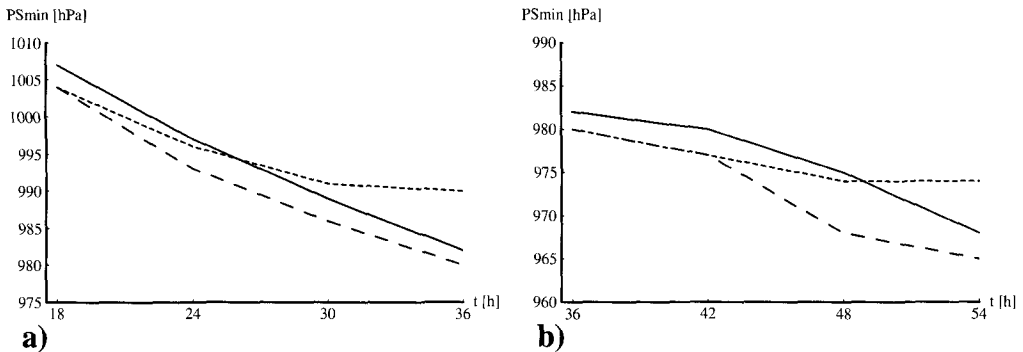


FIG. 4.13: The minimum SLP of the secondary cyclone for: – observed system (solid lines), the standard 54 hour forecast (long-dashed lines), and a dry simulation (short-dashed lines). The switch from moist to dry dynamics occurs after 18 hours (panel a) and after 36 hours (panel b).

A comparison of the PV structures of the dry and the moist 18 h simulation in a cross section is instructive (see Fig. 4.14). In the dry simulation the band is vertically centered at about 800 hPa, has an amplitude of ~ 0.8 pvu, and is comparatively shallow (panel b). In the moist simulation the band is much deeper (extends from the surface to about 650 hPa), and has values of more than 1 pvu throughout its vertical extension (panel a). The location and vertical extension of the PV band coincides with the region of high moisture (relative humidity exceeds 90%).

This comparison of the low-level PV structures of a dry and moist simulation indicates that PV is not only advected to higher altitudes in the dry simulations, but also that the amplitude of the moist PV band becomes much stronger in time, i.e. more PV is produced below the PV band by diabatic processes than is advected through and destroyed above the band. This is highlighted by a calculation of heating and PV rates for the moist simulation (Fig. 4.14c). The heating extends from low-levels to ~ 600 hPa, and reaches values of about 2.5 K h^{-1} at 600 hPa. Positive PV rates are confined below 850 hPa, have an amplitude of 0.7 pvu h^{-1} , and negative PV rates at 550 hPa have an amplitude of $\sim 0.2 \text{ pvu h}^{-1}$. Note that here diabatic processes are remarkably stronger than in an earlier phase of the development (compare with Fig. 4.10).

The negative PV rate close to the 310 K isentrope has in the vicinity of the front an effect on the upper-level PV structure (compare the upper-level PV in panel a and b), but the overall evolution of the upper-level PV is only slightly modified by the absence of moist processes (not shown), indicating the weak influence of low-level PV elements and diabatic processes upon the upper-level features.

The direct inferences are that moist processes play a dominant role for this event of frontal wave cyclogenesis. In particular the dry runs did not capture the (full) deepening of the secondary cyclone, and it is the continuous condensational heating that gives rise to the quasi-steady PV anomaly. This in turn enhances the flow field on the warm side of the front, i.e. the low-level jet is increased, and gives rise to additional warm moisture advection that serves to reinforce the diabatic heating and PV generation. These diabatic processes are confined to the lower and middle troposphere, and leave the upper-level dynamics comparatively

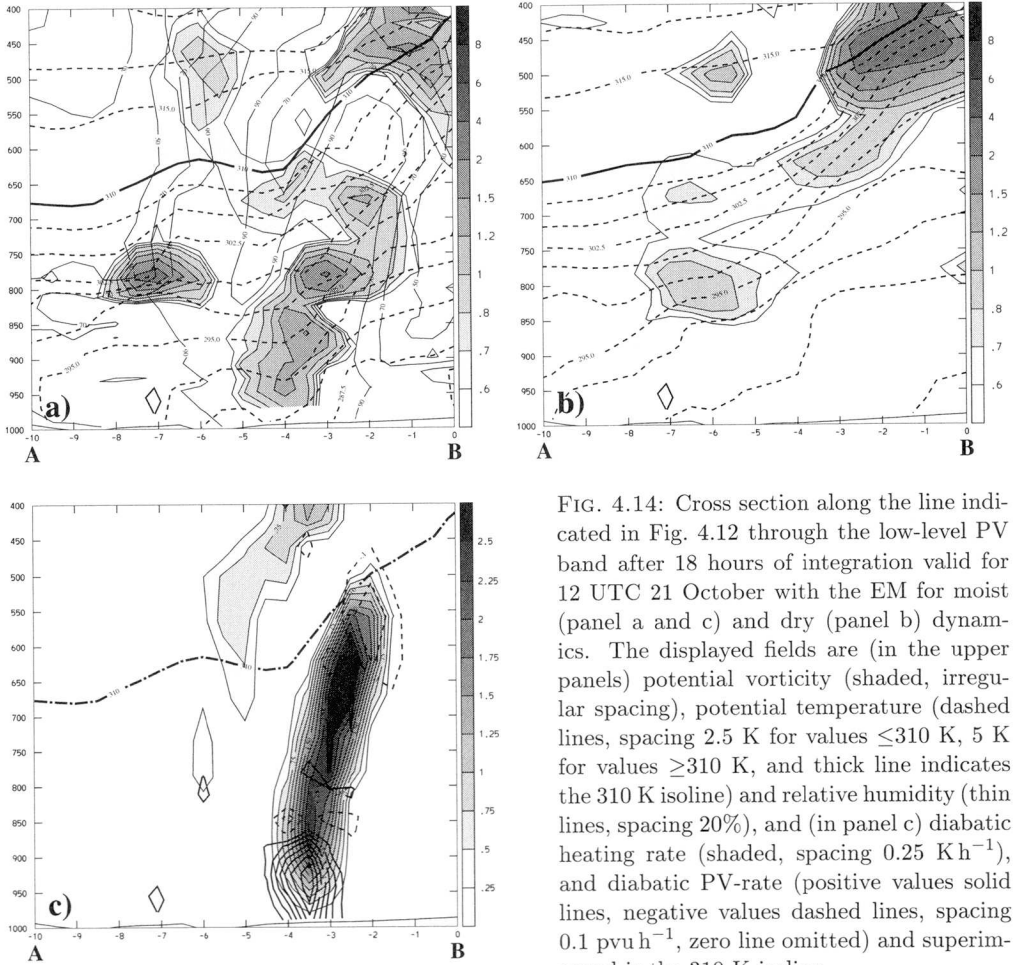


FIG. 4.14: Cross section along the line indicated in Fig. 4.12 through the low-level PV band after 18 hours of integration valid for 12 UTC 21 October with the EM for moist (panel a and c) and dry (panel b) dynamics. The displayed fields are (in the upper panels) potential vorticity (shaded, irregular spacing), potential temperature (dashed lines, spacing 2.5 K for values ≤ 310 K, 5 K for values ≥ 310 K, and thick line indicates the 310 K isotherm) and relative humidity (thin lines, spacing 20%), and (in panel c) diabatic heating rate (shaded, spacing 0.25 K h^{-1}), and diabatic PV-rate (positive values solid lines, negative values dashed lines, spacing 0.1 pvu h^{-1} , zero line omitted) and superimposed is the 310 K isotherm.

unaffected.

4.5 Dry Simulation with a Diagnosed PV-Rate

Here we take our diagnosis of the role of the low-level PV one step further and undertake a “dry” simulation but with a sequentially modified low-level PV corresponding to that of the moist simulation. The procedure is a sequence of the following steps:

- (i) a 6 hourly dry simulation from t to $t + 6$ is performed
- (ii) PV structures below the 450 hPa level at $t + 6$, i.e. tropospheric PV, is compared with a standard control simulation at the same time

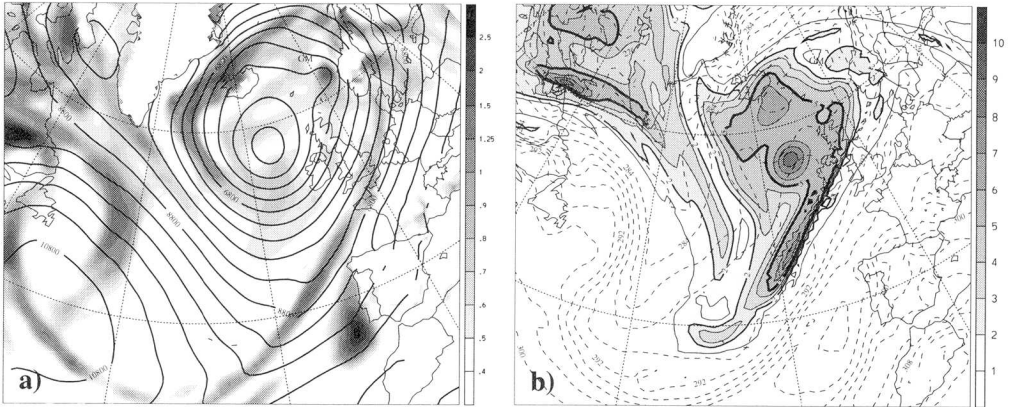


FIG. 4.15: A 54 hour dry simulation with a diagnosed PV rate. The displayed fields correspond to Fig. 4.1 and Fig. 4.2.

- (iii) the so defined PV differences between the control and the dry simulation are inverted and the flow fields of the dry simulation at $t + 6$ are modified such that the modified dry fields and the control simulation have the same PV structure in the troposphere
- (iv) the modified field then serves as the “initial” field for another sequence starting with point (i)

Such an experiment exhibits a very similar development as the simulation with the full physics. Fig. 4.15 shows the low and upper PV distribution of this dry simulation with diagnosed PV-rate after 54 hour of integration. Both the low- and upper-level patterns (where PV has not been modified) are very similar to the standard forecast. Panel a) should be compared with panel a) (dry 54 hour simulation) and panel d) (moist 54 hour simulation) of Fig. 4.12.

Table 4.3 gives a summary of the SLP values and locations of the secondary and the mother cyclone for the dry simulations. The dry simulation with modified PV is to be compared with the corresponding observed values and the moist simulations given in Table 4.1. In the dry simulations the secondary cyclone is located further south-west. Also in the modified dry simulation the location and depth of the frontal wave cyclone corresponds well to the observed one, but the mother cyclone deepened even more than the observed one.

This hybrid simulation demonstrates that (a) PV is a key dynamical variable in the sense that the development is accurately represented provided the parametrised physical processes accurately represent the influence of the PV generation/destruction and (b) that the changes in PV are adjusted to a balanced flow on a time scale which is small compared with the time scale of the instability process. Point (b) is a prerequisite for an analysis of the PV elements via PV inversion techniques.

		54 h dry	36 h dry	18 h dry	54 h with PVR
secondary cyclone	p	984 hPa	979 hPa	974 hPa	968 hPa
	long	3.0°W	0.5°W	1.0°E	1.5°E
	lat	57.5°N	61.5°N	62.0°N	62.0°N
mother cyclone	p	965 hPa	964 hPa	960 hPa	958 hPa
	long	17.5°W	17.0°W	17.5°W	15.5°W
	lat	58.0°N	58.0°N	59.0°N	57.5°N

TABLE 4.3: Central pressure and location of the secondary surface and mother cyclone at 12 UTC on 21 October for a 54, 36, and 18 hour dry simulation, and for a 54 hour dry integration with a diagnosed PV rate.

4.6 Inversion of Key PV Elements

A calculation of the balanced wind component associated with isolated PV anomalies should shed light on the interaction of PV elements and their influence upon other features. Such a partition of the PV distribution and attribution of the flow fields to isolated elements has been the subject of recent research.

Inversion techniques based on a nonlinear balance condition (e.g., Davis and Emanuel 1991, Davis 1992) or based on the quasi-geostrophic approximation (e.g., Hakim et al. 1996) have been invested. Both approaches hinge upon the use of specific boundary conditions in a limited domain, and the inverted flow fields are therefore dependent on for example the choice of the domain. Domain independent vorticity and divergence attribution has been proposed and studied by Bishop (1996a), Bishop (1996b), and Renfrew et al. (1997). There the free Greens function (i.e. with vanishing velocities at infinity) has been used. Here we choose a large enough inversion domain such that the inverted velocity fields, on the domain where the amplitude is significant, depend only weakly on the choice of the inversion domain. The inversion technique used here is that described in chapter 2, i.e. we apply a piecewise inversion in the quasi-geostrophic limit.

For the present case we select for partition three PV anomalies. These elements are (a) the low-level PV band, (b) the upper level anomaly P_{s1} , and (c) P_{s2} , but there remains some subjectivity in isolating these anomalies. A diagnosis of the flow structure associated with these elements is performed at the beginning of the second phase of the frontal wave development, i.e. at 18 UTC on the October 20 October.

As reference PV distribution the ECMWF analysis fields will be used and perturbations are defined in terms of these fields.

4.6.1 The Low-Level PV-Band

Fig. 4.16 displays the selected low-level PV anomaly, and significant interest is attached to the wind and temperature distribution. The instability of such a structure has been considered as a driving mechanism of a frontal wave development (see chapter 3 and references therein). The definition of this anomaly has been performed by inspecting the PV distribution and the

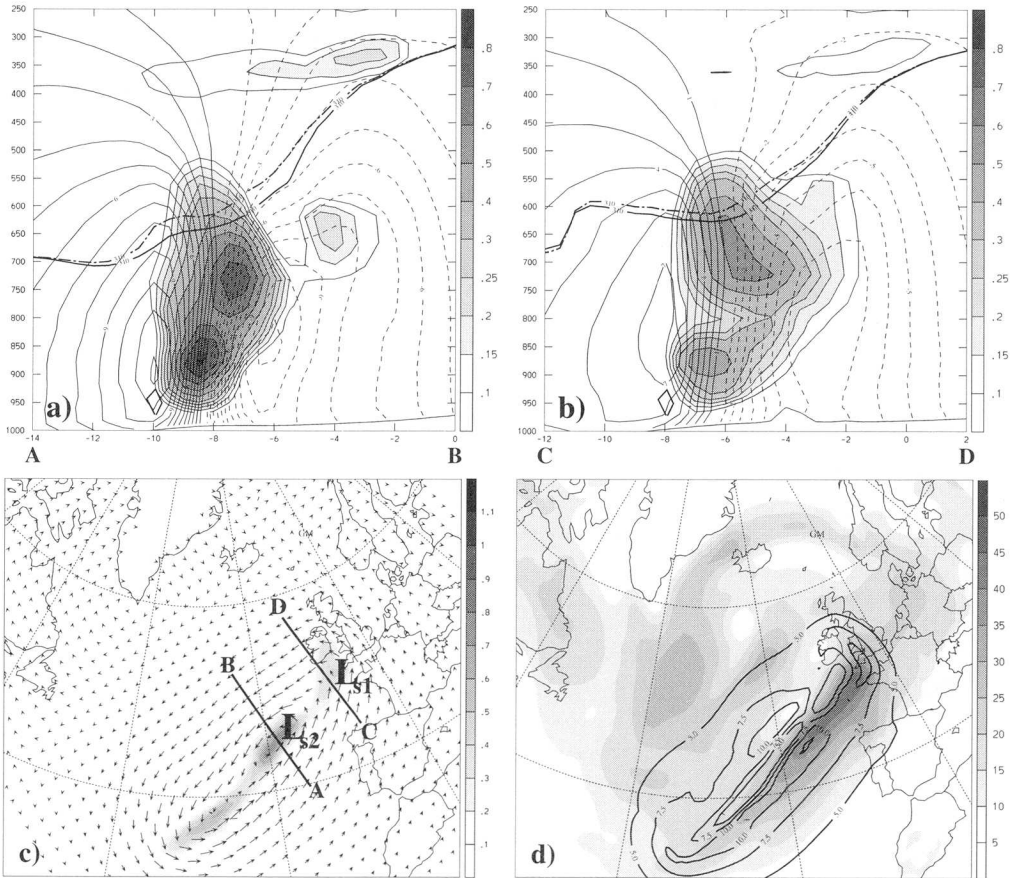


FIG. 4.16: Subjectively identified low-level PV band and associated wind components. In the upper panels the displayed fields are the PV perturbation that has been inverted (shaded, irregular spacing), the across wind field of the perturbation (positive values plain lines, negative values dashed lines, spacing 1 m s^{-1}), and superimposed is the 310 K isentropes of the ECMWF analysis (solid) and of the perturbed atmosphere (dash-dotted). The sections are indicated on panel c. Panel c) PV perturbation (shaded, spacing 0.1 pvu) and associated wind vectors at 850 hPa. Panel d) velocity field (shaded, spacing 5 m s^{-1}) indicating the prefrontal low-level jet and induced velocity field, (solid lines, spacing 2.5 m s^{-1}).

relative humidity field, and this enables us to distinguish between the low-level prefrontal PV anomaly and the upper-level PV intrusion. These two PV elements can, and often do, form a coherent PV structure along the frontal zone.

The anomaly intersects the 310 K isentropic surface in a region where the value of relative humidity exceeds 85% (panel a and b, compare also with Fig. 4.10 panel c and d). In the eastern (western) section the maximal across wind component is $\sim 7 \text{ m s}^{-1}$ ($\sim 11 \text{ m s}^{-1}$) and occurs at the edges of the PV anomaly at $\sim 850 \text{ hPa}$ ($\sim 900 \text{ hPa}$). The observed low-level

flow exhibits a wind maximum on the warm side of the front of $\sim 35 \text{ m s}^{-1}$ and a minimum of $\sim 10 \text{ m s}^{-1}$ on the cold side. Therefore a wind shear of about 25 m s^{-1} can be observed. Wind maxima attributable to the low-level PV anomaly via an inversion are $\sim 10 \text{ m s}^{-1}$ and these maxima are collocated with the observed extrema. From this considerations we estimate that the contribution of the PV anomaly on the induced wind field is about 80%. Note also that the region of strong prefrontal winds coincides with those of moist air (relative humidity $\sim 90\%$, see again Fig. 4.10), and therefore the wind component attributable to the low-level PV band contributes significantly to warm moist air advection.

The wind field decays strongly above the 310 K surface due to the higher value of the Brunt-Väisälä frequency in the stratosphere. At low levels the wind field has a component across the PV anomaly between the two vortices associated with L_{s1} and L_{s2} . This component is mainly attributable to the strong PV vortex corresponding to L_{s2} , and indicates that the wind field acts to a further breaking of the two PV maxima associated with the undulations L_{s1} and L_{s2} . At upper-levels the low-level induced wind field has an upstream component on the anomaly P_{s2} (not shown).

4.6.2 The Upper-Level Anomaly P_{s1}

On the 310 K surface the anomaly P_{s1} takes the form of an ellipsoid orientated west-east. Its length is of about 1000 km and it has a length to width ratio of $\sim 2 : 1$. In the vertical the anomaly is confined between 200 and 400 hPa, and the maximum amplitude is $\sim 8 \text{ pvu}$ (see Fig. 4.17). Maximum velocities ($\sim 20 \text{ m s}^{-1}$) related to this anomaly can be found near the 310 K surface at the edge of the anomaly. At the surface the contribution to the cold air advection of this anomaly has a maximum of $\sim 5 \text{ m s}^{-1}$ near the undulation L_{s1} . Note that the two maxima in the wind field near the surface are further apart than at tropopause level.

4.6.3 The Upper-Level Anomaly P_{s2}

Anomaly P_{s2} is located upstream of the developing frontal cyclone, has a length to width ratio of $\sim 4 : 1$ and resides in the layer between ~ 200 and 450 hPa. Inspection of the 7 pvu surfaces indicates that this anomaly is associated with a fold structure in the stratosphere (see Fig. 4.18 panel c). The induced wind field on the 310 K surface reaches up to 30 m s^{-1} , and at low-levels $\sim 6 \text{ m s}^{-1}$. At the western part of the PV band the wind field parallels the anomaly and its maximum is collocated with the upper-level PV anomaly (panel b), i.e. the induced wind field of the upper anomaly P_{s2} does not exert a lateral shear on the PV strip.

4.7 The Influence of the Upper-Level Structure on the Dynamics

The diagnosis of isolated PV elements with the inversion technique provides some indication of the interaction of these structures, but it constitutes a mere *static* diagnosis. The influence of these structures on the *dynamics* can be studied by performing simulations with modified

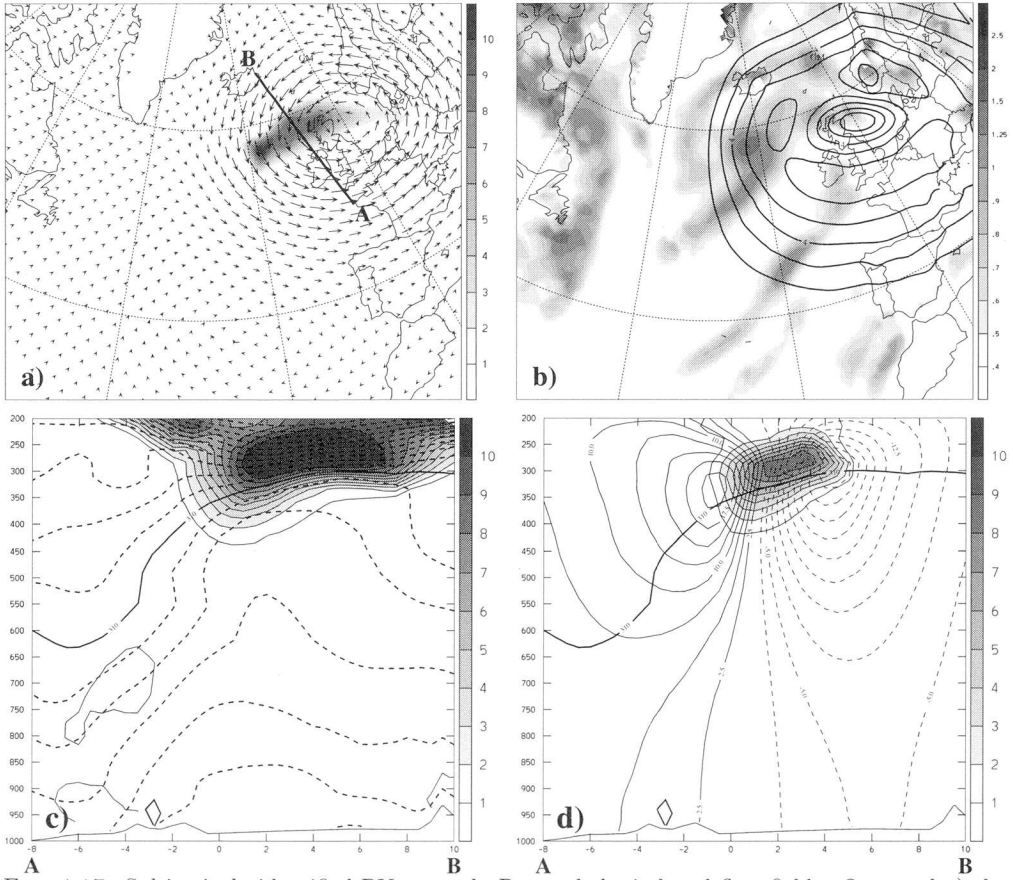


FIG. 4.17: Subjectively identified PV anomaly P_{S1} and the induced flow fields. On panel a) the displayed fields are the PV anomaly P_{S1} on the 310 K isentrope (shaded, spacing 1 pvu) and the induced wind field of the upper-level anomaly at 850 hPa. On panel b) the potential vorticity at 850 hPa (shaded, irregular spacing) and the absolute value of the wind field are displayed. The lower panels show cross sections along the line indicated on panel a). The displayed fields are on panel c) potential vorticity (shaded, spacing 1 pvu), potential temperature (dashed lines, spacing 2.5 K), and on panel d) the isolated upper-level PV anomaly (shaded, spacing 1 pvu) and the induced across wind field (positive values plain lines, negative values dashed lines, spacing 2.5 m s^{-1}).

PV structures in the initial fields. Such an analysis can help to determine the sensitivity of forecasts to initial analysis errors. (This theme is discussed in more detail in the next chapter.) Here we perform two 18 hour simulations from 18 UTC October 20 until 12 UTC October 21 with full physics but with modified PV. The first involves omitting the anomaly P_{S1} and in the second we exclude the anomaly P_{S2} .

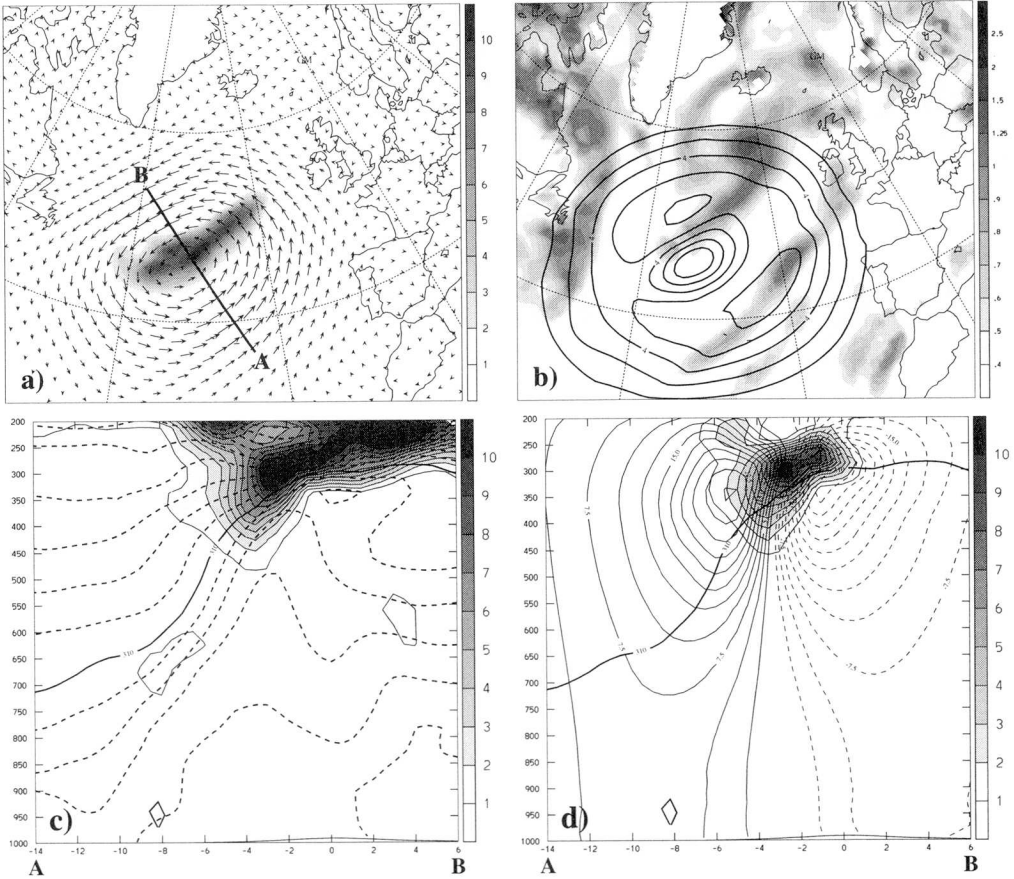


FIG. 4.18: The analogue of Fig. 4.17 but now for the PV anomaly P_{s2} .

4.7.1 A Simulation without Anomaly P_{s1}

In Fig. 4.19 the initial and 18 hour integrated structures are displayed. The PV features at low levels are comparable with those of a standard 18 hour integration. Inspection of the upper-level structures reveals the nonlinear interaction of the PV elements. The anomaly which formed in the standard forecast a vertically coherent structure with the mother cyclone is now located further west. There was less deepening of the frontal wave cyclone (by ~ 6 hPa) but slightly stronger development of the mother cyclone (by ~ 2 hPa) in the modified simulation. In this simulation the secondary cyclone is located about 300 km further to the south.

The upper-level PV distribution shows the missing of the anomaly in the standard forecast that is collocated with the mother cyclone. Other structures are very similar to the standard simulation.

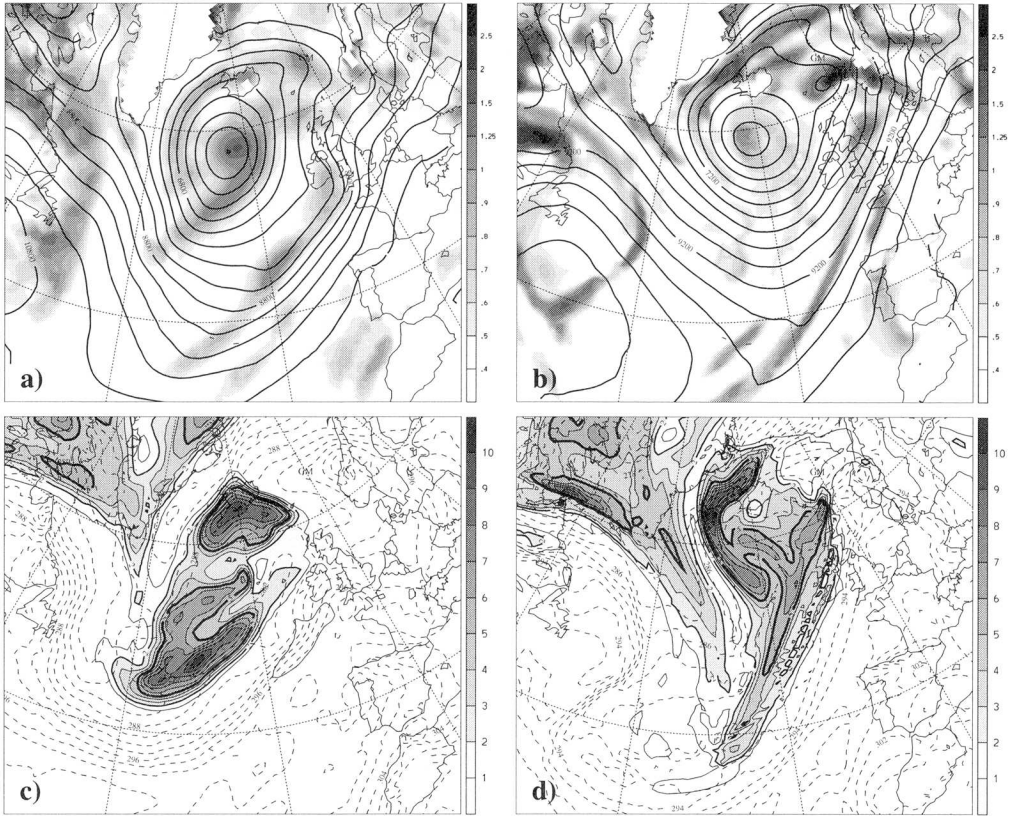


FIG. 4.19: 18 h forecast starting from an initial state without the upper-level anomaly P_{s1} . Displayed fields and shadings as in Figs. 4.1 and 4.2.

4.7.2 A Simulation without Anomaly P_{s2}

The influence of the anomaly P_{s2} on the low-level dynamics is weaker than that of anomaly P_{s1} . In this simulation the deepening and location of the frontal wave cyclone, and the low-level structural features are similar to the standard forecast. Also the structure of the low-level PV distribution for standard forecast and simulation with modified upper-level anomaly is very similar.

At upper-levels the elongated anomaly that lies parallel to the surface front in the standard simulation is much weaker. There is still an analogous structure of the anomaly P_{s2} , but this anomaly is here much weaker.

Table 4.4 gives the location and amplitude of the mother and frontal wave cyclone for these two simulations with modified initial state (compare also with values of standard 18 h forecast given in Table 4.1). Compared with the reference simulation, the modified upper-level structures caused in a 18 h simulation an error in the SLP of 6 hPa in the P_{s1} case, and of 2 hPa in the P_{s2} case.

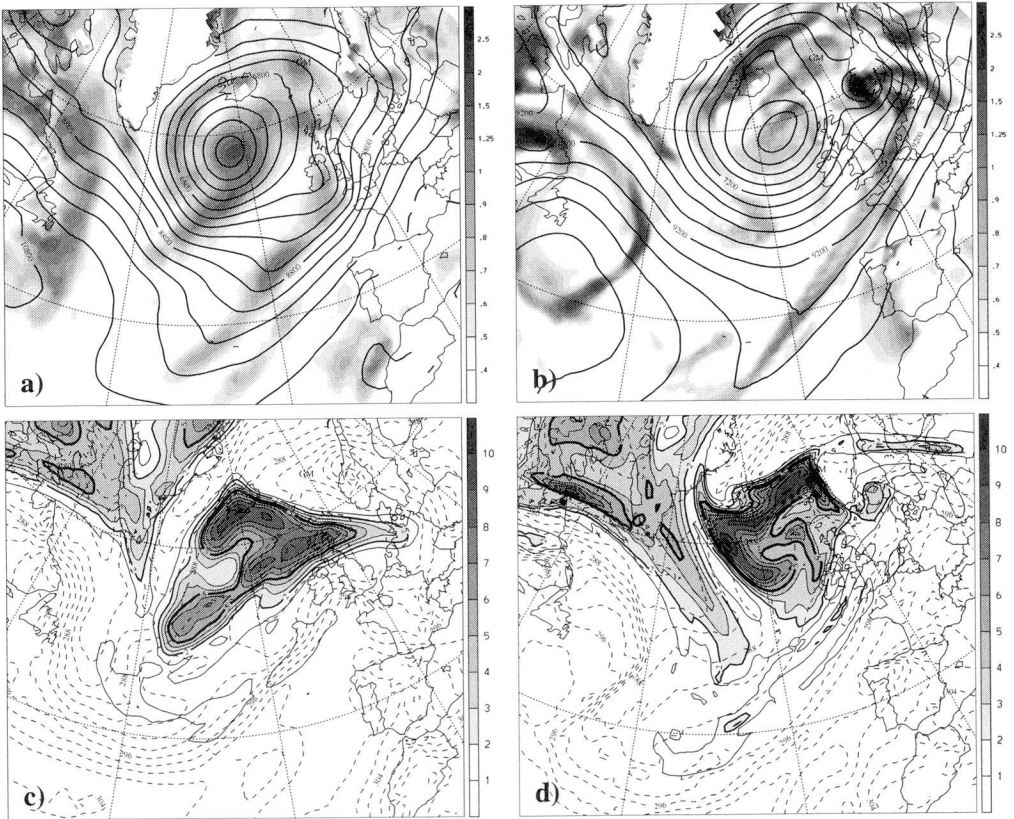


FIG. 4.20: 18 h forecast starting from an initial state without the upper-level anomaly P_{s2} .

		P_{s1}	P_{s2}
secondary cyclone	p	973 hPa	969 hPa
	long	1.5°W	5.0°E
	lat	62.0°N	59.5°N
mother cyclone	p	963 hPa	961 hPa
	long	21.5°W	15.5°W
	lat	58.5°N	59.0°N

TABLE 4.4: Central pressure and location of the secondary surface and mother cyclone at 12 UTC on 21 October for a 18 hour simulation without anomaly P_{s1} and P_{s2} .

4.8 Discussion

A case study of a frontal wave development was performed based on ECMWF analysis data and simulations with the EM. We focused on some possible mechanisms for the formation

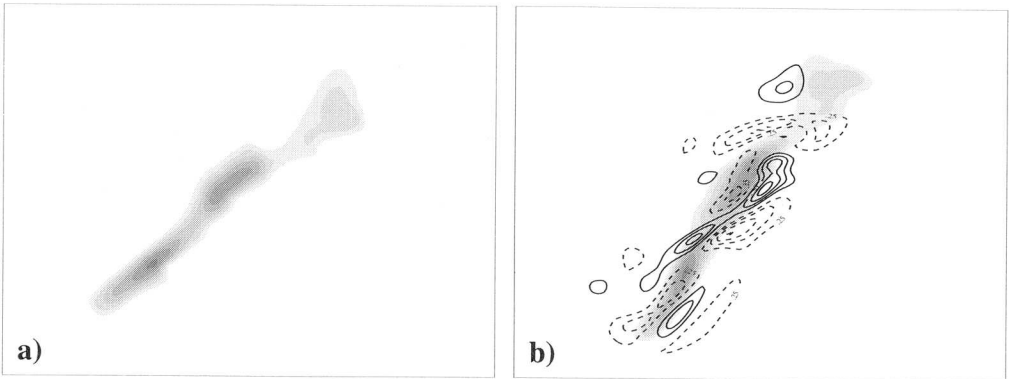


FIG. 4.21: 18 h forecast starting from an initial state including the observed low-level PV band at 18 UTC 20 October in an idealised environmental flow. In panel b) the vertical velocity is overlaid with continuous lines indicating upward, and dashed lines downward motion (spacing 0.25 hPa h^{-1} , zero line omitted).

of the secondary cyclone. The main results can be summarised as follows:

- (i) the limited area model forecast predicted the location and strength of this event satisfactorily,
- (ii) the development of the frontal waves can be linked to the evolution of the low-level PV band which in turn is strongly influenced by moist processes,
- (iii) the horizontal evolution of the PV band can be understood in terms of a pseudo advective development, i.e. the trajectory calculations indicate that the maxima of the observed and the corresponding advected PV maxima are horizontally collocated, i.e. there is a coherence of moist processes and the low-level PV band. This results from the continuous production and destruction of PV below and above the PV anomaly,
- (iv) most of the observed strong prefrontal low-level jet can be linked to the low-level PV anomaly,
- (v) the influence of small-scale upper-level PV structures on the low-level development is, in this particular case, marginal. Larger-scaled upper-level structures can modify the strength and location of the secondary cyclone, but the overall low-level PV structure is only weakly affected, and
- (vi) the cloud-diabatically generated low-level PV anomaly adjust on a comparatively short time scale to a balanced flow structure.

The idealised studies of chapter 3 suggest that the present PV band would in a barotropic environment undergo an instability process and would decay into isolated vortices. A 18 h simulation of the present PV band as isolated in Fig. 4.16 shows that in an idealised environment (barotropic, unsheared ambient flow on an f -plane) the PV band exhibits on a short time scale only a weak development (see Fig. 4.21). Again this demonstrates that the instability mechanism of the PV band alone can not capture the full strength of the development.

A notable difference between the idealised dry PE simulations of either simple geometrical low-level PV bands or of observed PV structures, and the simulations of this frontal wave development with full physics, is the strength of the vertical velocity field. In the idealised simulations the maximal vertical velocities are $\sim 4 \text{ hPa h}^{-1}$ for the simple PV structure of chapter 3 or $\sim 1 \text{ hPa h}^{-1}$ of the observed isolated PV anomaly. In the simulations of this particular frontal wave with moist processes, we obtained near the north-eastern tip of the PV band just before maximal intensification, strong upward velocities of $\sim 40 \text{ hPa h}^{-1}$ in amplitude. The maximum in the vertical velocity field occurs in the standard simulation of this frontal wave event at the north-eastern tip of the band, whereas in the idealised simulation it occurs near the central PV vortex.

Leer - Vide - Empty

Chapter 5

Misforecasts of Synoptic Systems: Diagnosis via PV-Retrodiction

5.1 Introduction

Short-range numerical weather prediction of synoptic and sub-synoptic features is an event-orientated task. The challenge is to predict for a narrow window in space and time the occurrence or non-occurrence of specific weather systems, for example, rapid frontal-wave cyclogenesis or a frontal passage with accompanying heavy rainfall. A significant forecast failure can be associated with the development of a nonpredicted system, the nondevelopment of a predicted system, or the inaccurate prediction of the amplitude and/or track of such a system in space and time.

Forecast failure can itself be attributed to deficiencies in the model formulation and/or error in the specification of the initial field. Both shortcomings are compounded by the error growth due to the *intrinsic unpredictability of atmospheric flow*. Studies of the errors growth of medium-range forecasts indicate that there remains significant scope for model improvement (Simmons et al. 1995) and that initial conditions can also play a crucial role (Molteni et al. 1996). Studies of the error characteristics of short-range forecasts need to take into account the event-orientated and short-range nature of the prediction task and thereby recognise that the error growth need neither be spatially diffuse nor temporally sustained. In effect localised transient growth, unrelated to the standard Lyapunov rate, might frequently dominate the error evolution.

The extant studies on error growth in short range forecasts have followed several avenues. Predictability experiments with limited-area models have documented the sensitivity of the domain averaged error-measures to the lateral boundary data and the structure of the initial perturbations/error fields (e.g. Errico and Baumhefner 1987, Van Tuyl and Errico 1989, Vukicevic 1991, Lüthi et al. 1996). Simulations of individual events have provided some indication of the influence of spatial resolution, parameterisation schemes, and initial analysis errors (see, e.g., Kuo and Reed 1988, Mullen and Baumhefner 1989, Shutts 1990). Likewise the COMPARE project (see, e.g., Gyakum and co authors 1995) intercompares the performance of different operational forecast models. Results from this project, derived for an event of secondary cyclogenesis, indicate a sensitivity to horizontal resolution, a tendency

to underestimate the deepening and to slightly misrepresent the track, and also an important contribution of upper-level features to the cyclone's initiation. An alternative approach to the problem is to exploit the adjoint of a limited-area forecast model to investigate the sensitivity to errors in the initial state and to ascertain the structure and growth rate of the associated singular vectors (Errico and Vukicevic 1992, Errico et al. 1993, Ehrendorfer and Errico 1995, Langland et al. 1995). The results suggest that the optimal structures for growth correspond to shallow lower-tropospheric perturbations that slope upstream with height. Caveats to this approach relate to the limitations of the tangent-linear model and the sensitivity of the perturbations to the choice of the error norm. Another conceivable approach would be to examine consecutive operational forecasts during their (inevitably short) overlapping integration periods.

The focus of this chapter is the diagnosis of the initial errors in short-range forecasts. Such a diagnosis should ideally help elicit the nature, cause, and/or origin of the associated error(s) and point to the requisite remedial action. For NWP forecast systems, the errors in the initial analysis stem from the combination of errors in the background fields derived from an earlier forecast and an inadequate observational dataset.

Deficiencies in the analysis can be related to, and interpreted in terms of, errors in the location of key upper- and lower-level flow features and to the richly structured sub-synoptic scale features of the precursor flow. Moreover, the projection of these errors onto the singular vectors will determine the form and amplitude of the subsequent error growth. A recent approach (Rabier et al. 1996) has been to adapt the adjoint approach to examine the sensitivity of the 48-hour forecast errors with respect to the initial analysis.

Here an alternative approach is pursued to diagnose the contribution of tropopause-level flow features to misforecasts. The strategy, based upon the potential vorticity (PV) perspective, is outlined in the next section. It can yield information on the nature of the PV-error in the initial analysis and insight on the dynamics of the error evolution. Its use is illustrated by application to a misforecast of an event of frontal-wave cyclogenesis (section 5.3). In light of the derived results some comments are made on more general analysis, predictability, and forecasting issues (section 5.4).

5.2 The Approach

The PV perspective of synoptic and sub-synoptic scale atmospheric flow is founded on three constituents: PV conservation in the adiabatic and frictionless limit; PV inversion in the balanced-flow limit; and PV partition into coherent, distinctive elements of the observed flow. The approach to be outlined here utilises all three constituents.

First, the concept of partition encourages the identification of cyclogenesis with the self-development and the strong interaction of key PV elements. These elements are taken to be major undulations and fragments of the potential vorticity on tropopause-transcending isentropic surfaces, elongated sub-synoptic prefrontal bands of low-level potential vorticity, emerging towers of potential vorticity in the neighbourhood of the incipient cyclone, and the surface potential temperature pattern that accompanies fronts. (For an account of the nature of the various possible cyclogenetic interactions see, for example, Hoskins et al. 1985, Hoskins

and Berrisford 1988, Schär and Davies 1990, Joly and Thorpe 1990a, Thorncroft and Hoskins 1990, Davis and Emanuel 1991, Reed et al. 1992, Malardel et al. 1993, Appenzeller and Davies 1996.) Pivotal to the present study is the deduction that in the ambient environment of incipient cyclogenesis the omission of one feature, or the misspecification of its amplitude or location (and thereby its phase relative to the other key PV signatures), can have a major impact upon the subsequent development.

Second, the principle PV conservation can be applied to anomalously positive PV-elements at tropopause level since, for these stratospheric in origin features, the in situ diabatic and frictional effects are comparatively weak. (This clearly does not apply to mid- and low-tropospheric PV-elements that often owe their very existence to cloud-diabatic effects.) In effect these elements are/were advected quasi-conservatively by the flow field.

Third, the concept of inversion (together with retrodictive advection) provides an estimate of the space-time history and the associated flow field of these tropopause-level PV elements.

The proposed diagnostic strategy utilises these three constituents of PV perspective to examine a misforecast and entails four sequential steps (see Fig. 5.1):

- Step (i) the identification of key upper-level PV error elements at the forecast-time by comparison with the contemporaneous analysis,
- Step (ii) the Lagrangian retrodiction of these elements back to the initial time in a process involving intermittent PV-inversion to successively modify the advective component of the analysed (or model forecast) flow fields,
- Step (iii) incorporation of the resulting PV distribution at the initial-time to form a revised initial analysis, and
- Step (iv) a further conventional forward prediction with the revised fields.

This four-step procedure isolates the contribution of the upper-level PV error. It has therefore the potential to provide information on the nature of the error in the initial field, and to yield insight on the role of upper-level effects in the cyclogenesis.

5.3 A Case-Study

To illustrate the foregoing approach we apply it to a misforecast of one particular event of rapid Atlantic frontal-wave cyclogenesis in January 1993. The analysis data is derived from the six-hourly “forecast-cum-analysis” cycle of the ECMWF. Simulations of the event are performed with a version of the EM.

5.3.1 Synopsis of the Analysed Event

The genesis of the frontal-wave cyclone occurred in the 24 hours from 12 UTC on the 12 January 1993. The system originated on an elongated cold front that trailed out from Europe to the mid-Atlantic. Fig. 5.2 shows the sea level pressure (SLP) pattern for 00 and 12 UTC on the 13 January. The system is discernible at the earlier time (panel a), and intensified rapidly in the 6 hour period to 12 UTC to yield a tight mesoscale low pressure system off the South Wales coast (panel b). A detailed analysis recording the synoptic,

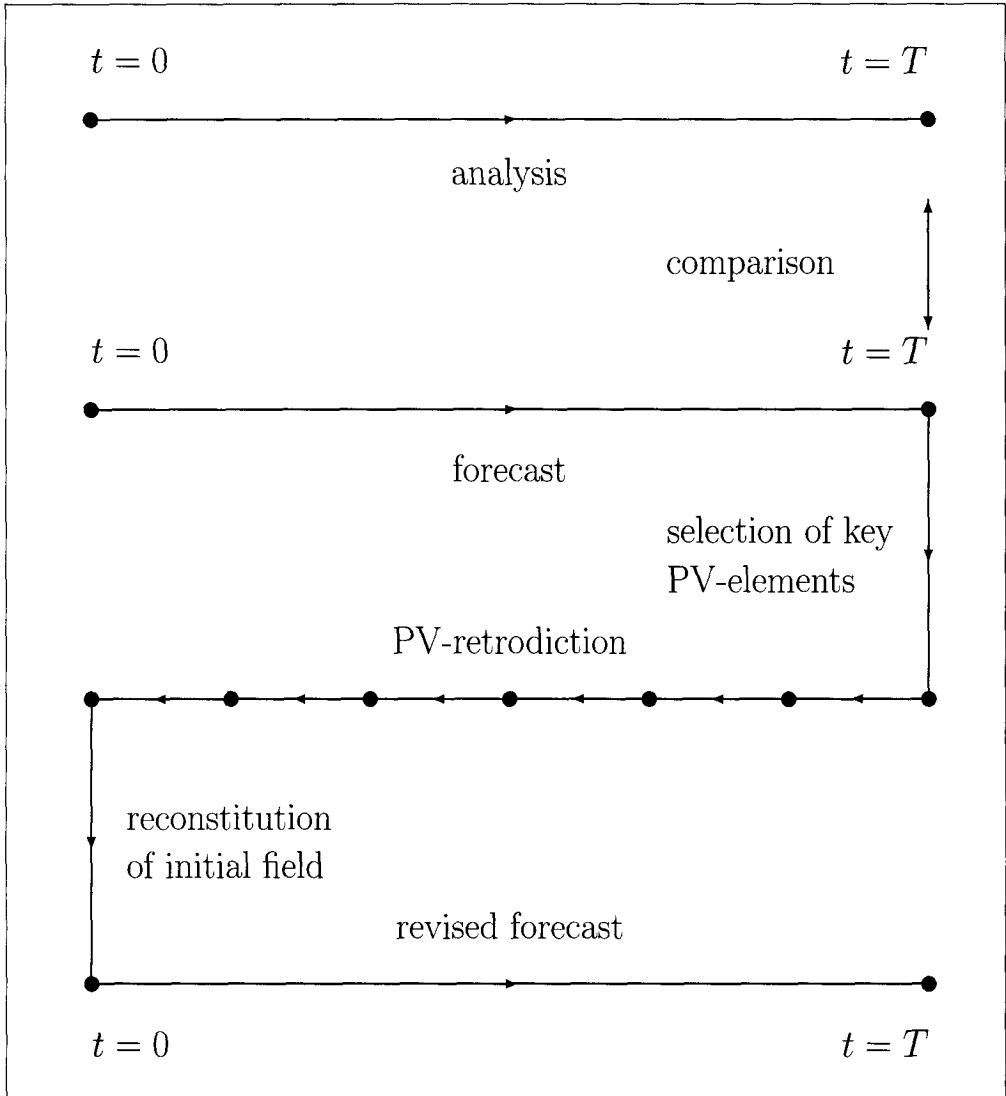


FIG. 5.1: A schematic of the four-step PV-retrodicted cycle. It comprises:- (i) a comparison of the analysis and the standard forecast and selection of key upper-level PV error elements at $t = T$, (ii) a Lagrangian advection of these elements back to the initial time in a process involving intermittent PV-inversion to successively modify the analysed fields, (iii) an incorporation of the resulting PV distribution at $t = 0$, and (iv) a further conventional forward prediction with the revised fields.

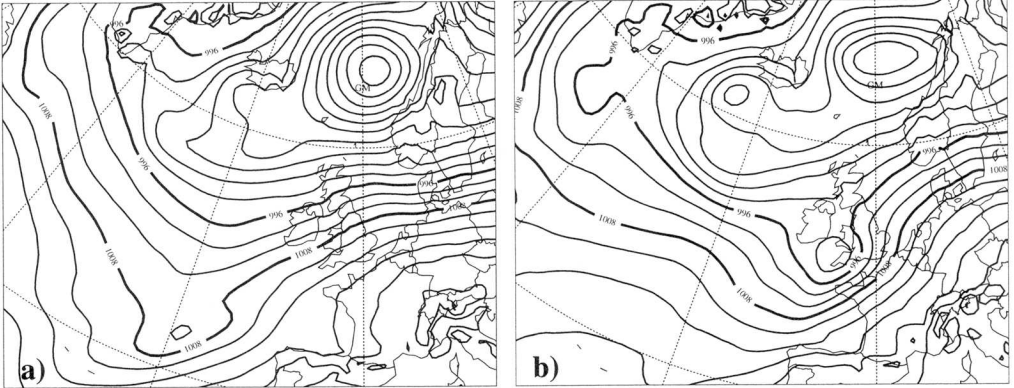


FIG. 5.2: The sea level pressure pattern (spacing 4 hPa, 996 and 1008 hPa isolines bold) for 00 and 12 UTC 13 January 1993.

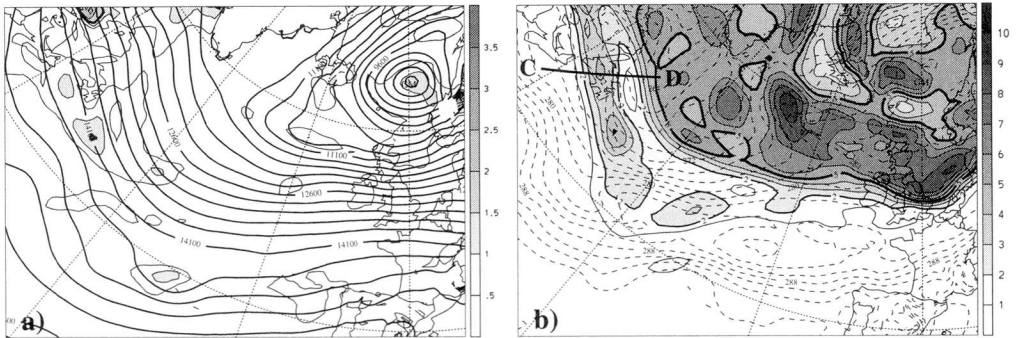


FIG. 5.3: ECMWF initialised analysis at the starting time of the forecast (i.e. 12 UTC 12 January). Panel a): Geopotential at 850 hPa (thin line, spacing $200 \text{ m}^2 \text{ s}^{-2}$) and potential vorticity (shaded, spacing 0.5 pvu, the thick line denotes the 1.5 pvu isoline). Panel b): Potential temperature field at 850 hPa (dashed lines, spacing 2 K), and potential vorticity on the 310 K isentropic surface (shaded, spacing 1 pvu). Contour spacing is 2 K for potential temperature and 1 pvu for potential vorticity. (The thick line corresponds to the 2 pvu and the bold to the 5 pvu isoline.)

satellite, radar, and PV signatures of the event is given by Browning and Roberts (1994). Here a synopsis is given of features that are particularly pertinent to the present study.

At the starting time for the forecast – 12 UTC on the 12th January – the analysis shows that at 850 hPa there is a slack mid-Atlantic trough with a weak PV anomaly at its base (Fig. 5.3a). Also at this time there are hints of almost collocated undulations in the 850 hPa thermal field and upper-level PV pattern (Fig. 5.3b). The corresponding fields at 00 and 12 UTC on the 13th (see Figs. 5.4 and 5.5) show synchronous development of upper and lower-level features. By 12 UTC on the 13th there is, at 850 hPa, a distinct mesoscale trough with a collocated thermal ridge and a strong mesoscale arch of potential vorticity, whilst aloft on the 310 K isentropic surface there has emerged a compact quasi-circular sub-synoptic PV

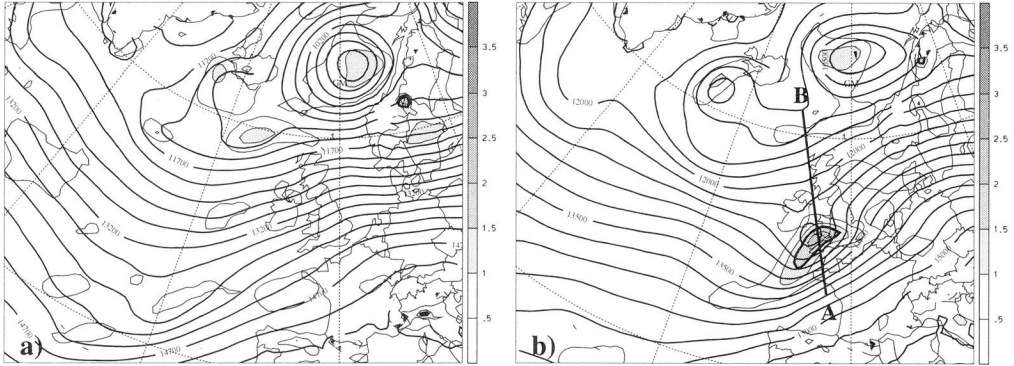


FIG. 5.4: ECMWF initialised analysis fields on the 850hPa surface for 00 UTC 13 January 1993 (panel a) and 12 UTC 13 January 1993 (panel b). The displayed fields are geopotential and potential vorticity (same spacing as in Fig. 5.3a). The bold line demarks the location of the vertical section shown in Fig. 5.6.

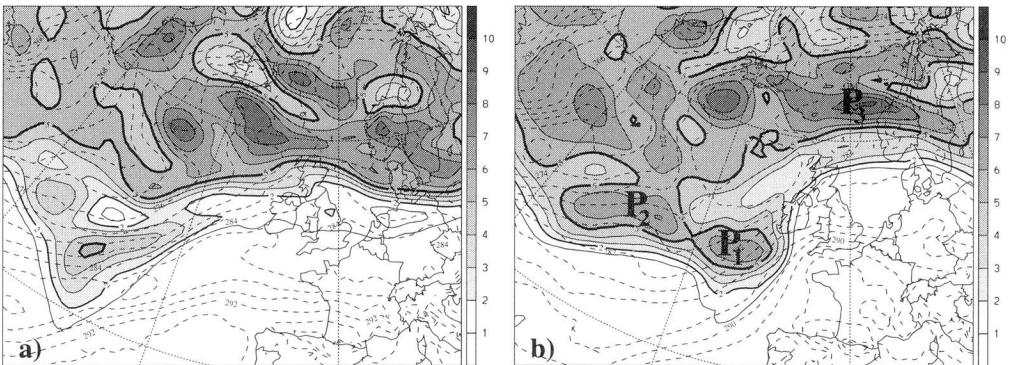


FIG. 5.5: ECMWF initialised analysis fields for 00 UTC 13 January 1993 (panel a) and 12 UTC 13 January 1993 (panel b). The displayed fields are potential temperature (dashed lines) on 850hPa and potential vorticity (shaded) on the 310K isentropic surface (same spacing as in Fig. 5.3b).

feature (labeled P_1 in Fig. 5.5) to the west of the low-level system.

Further details of the strength and structure of the system's PV anomalies at 12 UTC on the 13th are shown in the cross-sections displayed in Fig. 5.6 (location of the section is marked on Fig. 5.4b). A diabatic-induced tropospheric PV tower extends to 500 hPa with its maximum (~ 1.5 pvu) located just below the 850 hPa level. The tower's diabatic heating rate and PV production rate at this time (computed following Wernli and Davies (1997)) possess maxima of respectively 2 K h^{-1} at 800 hPa and 0.5 pvu h^{-1} at 950 hPa. These patterns are consistent with the continuous production and subsequent destruction of potential vorticity of the air parcels as they transit through the tower (cf. Wernli and Davies (1997)). The stratospheric PV intrusion aloft has an amplitude of about 7 pvu and reaches down to circa 450 hPa in a region that is essentially devoid of diabatic effects.

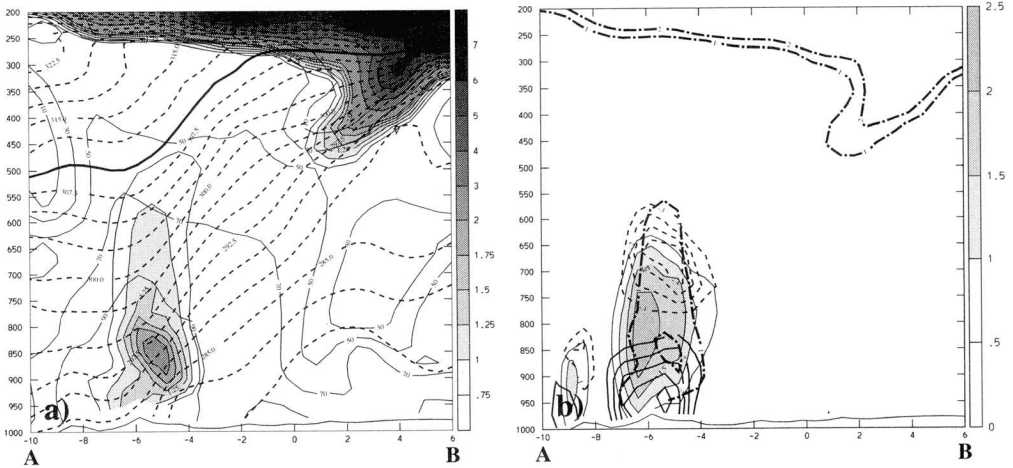


FIG. 5.6: Cross section at 12 UTC 13 January along the line indicated in Fig. 5.4. The displayed fields are (a) PV (shaded, spacing 0.25 pvu for values ≤ 2 pvu and 1 pvu for values ≥ 2 pvu), potential temperature (dashed lines, thick line indicates 310 K, spacing 2.5 K) and relative humidity (thin lines, spacing 20%); (b) diabatic heating rate (shaded, spacing 0.5 K h⁻¹), diabatic PV-rate (positive values solid lines, negative values dashed lines, spacing 0.1 pvu h⁻¹, zero line omitted) and superimposed the 1 pvu and 2 pvu isolines (dash-dotted lines).

From a PV perspective, the tower and the intrusion contribute substantially to determining the depth and location of the associated surface cyclone. Thus, the accurate representation of the structure and amplitude of these features is requisite for a successful forecast. Finally note that at 12 UTC on the 13th the system's upper- and low-level features are suitably phased for continued development, and indeed in the subsequent 24 hours the depression deepened a further 20 hPa.

5.3.2 A Forecast

A 24-hour forecast from 12 UTC on the 12th January performed with the EM model and starting from the initial analysis fields of the ECMWF fails to capture the cyclogenesis.

Comparison of the evolution of the forecasted fields (Figs. 5.7–5.9) with the corresponding analysis fields (Figs. 5.2, 5.4, 5.5) reveals only modest differences at 00 UTC on the 13th, but the differences amount to a significant misforecast by 12 UTC. At the latter time the SLP field shows only a weak cyclone, and likewise at 850 hPa the geopotential and potential temperature fields exhibit much weaker and more southerly undulations than those of the analysis. In the forecast fields the tropospheric PV signal is much less pronounced, and the upper-level PV pattern is less structured and weaker (approximately 3 pvu compared with 7 pvu in the analysis field).

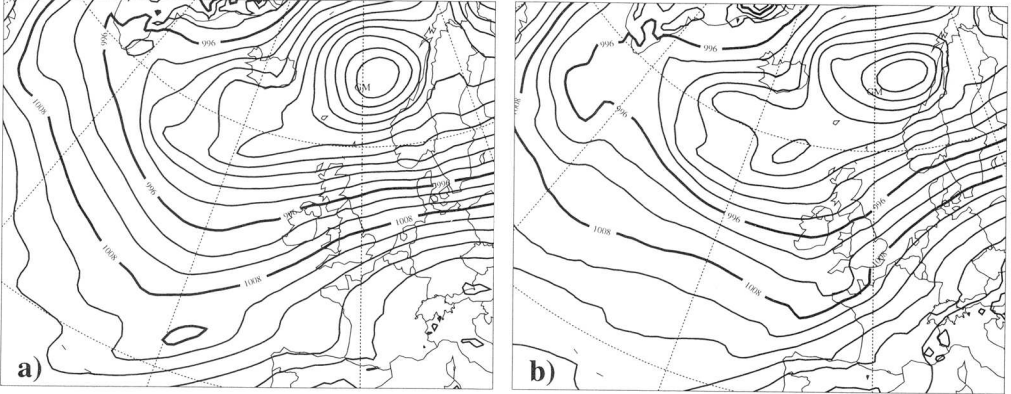


FIG. 5.7: As for Fig. 5.2 but now derived from the EM forecast.

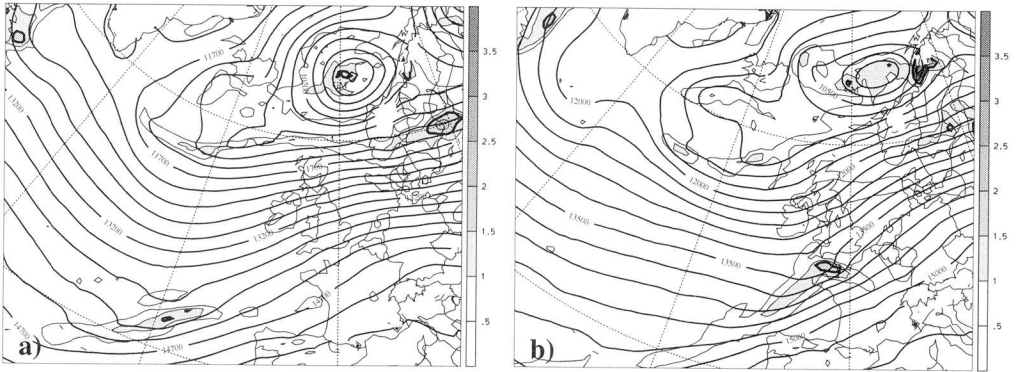


FIG. 5.8: The analogue of Fig. 5.4 but now derived from the forecast with the EM model.

5.3.3 Application of the Approach

The first task – Step (i) – is to identify key upper-level PV error elements at the forecast time. Coinspection of the forecasted and analysed PV patterns on the 310 K isentropic surface for 12 UTC on the 13th (Figs. 5.5b and 5.9b) indicates that two analysed anomalies (labeled P_1 and P_3 in Fig. 5.5b) are absent from the forecast field, whilst a third (labeled P_2) is much too weak. This is further highlighted in Fig. 5.3.3a, which shows the corresponding difference – hereafter termed somewhat loosely the PV error.

The error associated with P_1 is unipolar and localised, that of P_2 is unipolar but somewhat weaker and more diffuse, whereas that associated with P_3 is dipolar and more complex. The unipolar and dipolar error types are suggestive, respectively, of an undetected PV anomaly and of a mislocated PV-anomaly. The inference regarding P_1 is supported by inspection of a succession of analysed isentropic charts that reveal the non-conservation of its amplitude (cf. Figs. 5.3b and 5.5). The misrepresentation of the P_1 anomaly contributes directly to the misforecast of the structure and strength of the surface cyclone, and the

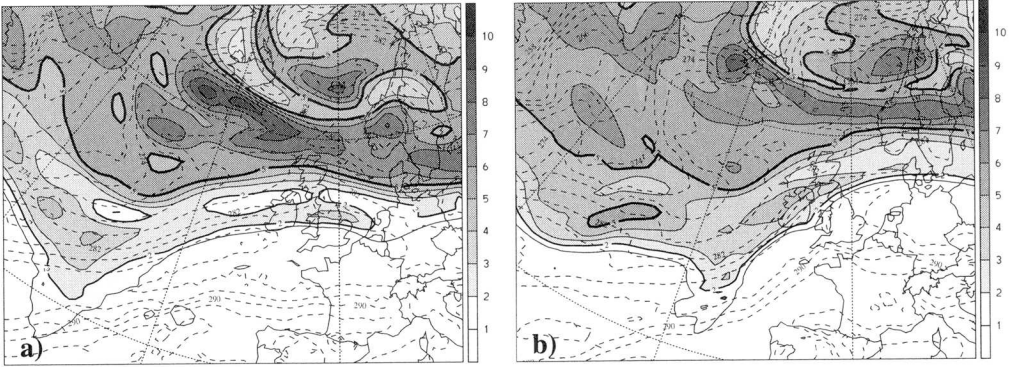


FIG. 5.9: The analogue of Fig. 5.5 but now derived from the forecast with the EM model.

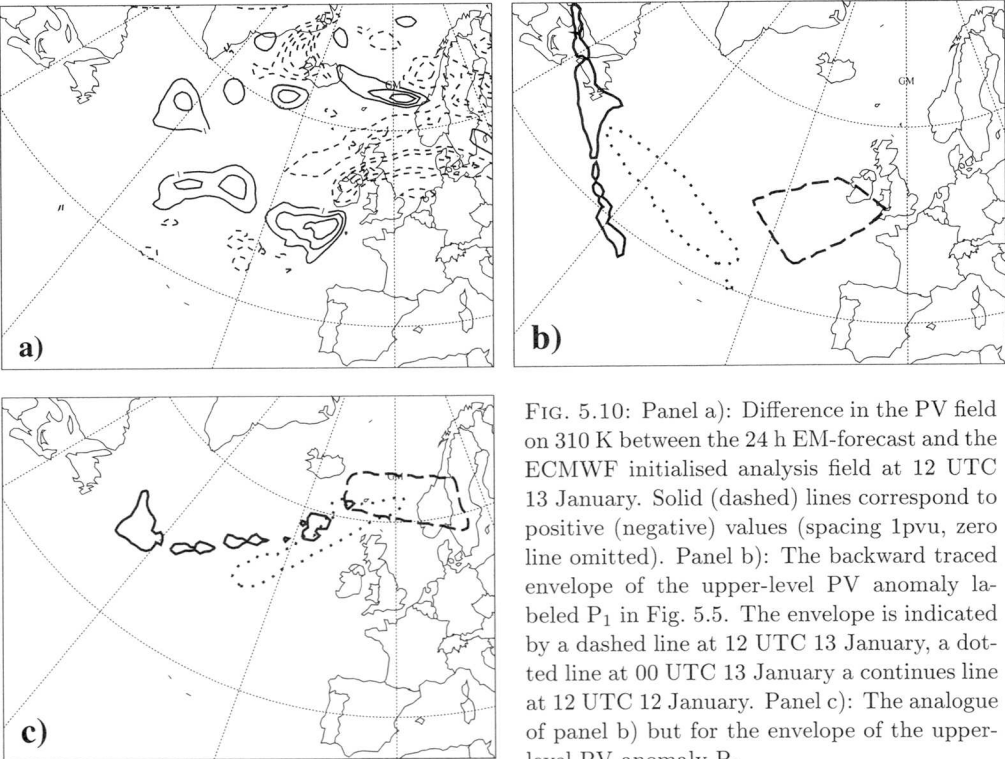


FIG. 5.10: Panel a): Difference in the PV field on 310 K between the 24 h EM-forecast and the ECMWF initialised analysis field at 12 UTC 13 January. Solid (dashed) lines correspond to positive (negative) values (spacing 1pvu, zero line omitted). Panel b): The backward traced envelope of the upper-level PV anomaly labeled P_1 in Fig. 5.5. The envelope is indicated by a dashed line at 12 UTC 13 January, a dotted line at 00 UTC 13 January a continues line at 12 UTC 12 January. Panel c): The analogue of panel b) but for the envelope of the upper-level PV-anomaly P_3 .

misplacement of P_3 to a location closer to the evolving cyclone could have influenced the latter's track and ascent field.

For Step (ii) two three-dimensional envelopes are established that fully encompass the spatial domains demarked by large PV-errors associated, respectively, with the P_1 and P_3

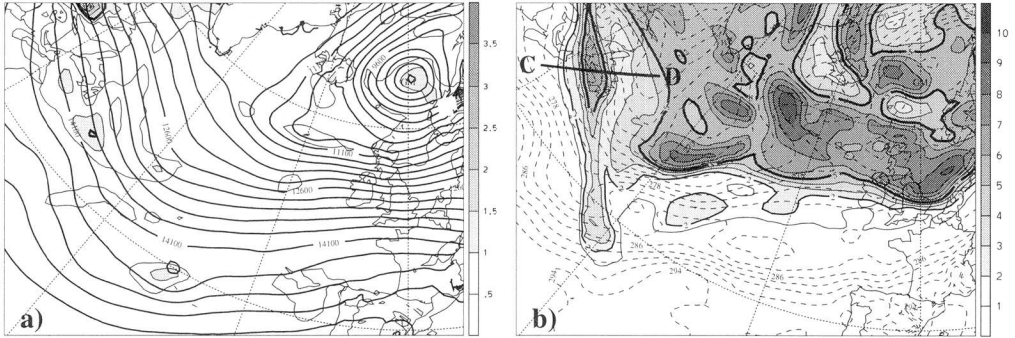


FIG. 5.11: Revised initial fields that incorporate the two retrodicted PV anomalies P_1 and P_3 . (Displayed fields and spacings as in Fig. 5.3.)

anomalies. These envelopes are then retrodicted for four successive intervals of six hours to 12 UTC on the 12th. At the end of each interval the modified PV distribution is inverted to derive a revised estimate of the flow. Depictions of the initial location and subsequent track of the two envelopes on the 310 K surface are shown in Fig. 5.3b,c. The P_1 -related and the P_3 -related anomalies at 12 UTC on the 12th have the form of two elongated bands that extend out over the Atlantic from near Newfoundland.

The result of Step (iii) – the reconstitution of the fields at 12 UTC on the 12th – is shown in Fig. 5.11. Comparison with the corresponding analysed patterns for this time (Fig. 5.3) is instructive. On the 310 K isentropic surface, the PV pattern is more richly structured with a stronger PV streamer extending southeast from Newfoundland into the Atlantic and a localised anomaly located poleward of its tip and within the stratospheric reservoir. In contrast at 850 hPa, the meteorological fields are essentially unchanged and this is consistent (see next subsection) with the signal from the upper-level mesoscale PV anomalies having a short vertical penetration scale.

The result of Step (iv) – the 24 hour forecast starting from the modified initial state at 12 UTC 12 January yields the forecast displayed in Figs. 5.12–5.14. Comparison with the corresponding ECMWF fields (Figs. 5.2, 5.4, 5.5) show that the structure of the upper-level PV pattern bears a closer resemblance to their analysis. However, the P_1 anomaly is more fragmented and assumes a structure not unlike the P_1 – P_2 couplet in the analysis field. (We comment further on this aspect in the next subsection). At low-levels the features resemble the realised cyclone, and in particular the observed and “repredicted” low-level PV anomalies possess similar structures and amplitude.

Fig. 5.15 shows the track and pressure fall of the surface wave-cyclone as recorded in the analysis and as predicted in the original and the revised forecasts. In the revised forecast the cyclone follows the observed track, but fails to capture the full pressure drop during the last six hours of the integration.

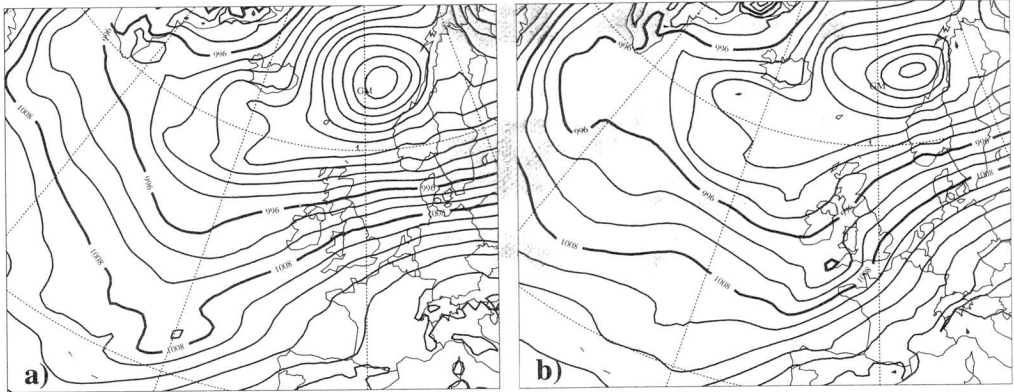


FIG. 5.12: As for Fig. 5.2 but now derived from the revised forecast.

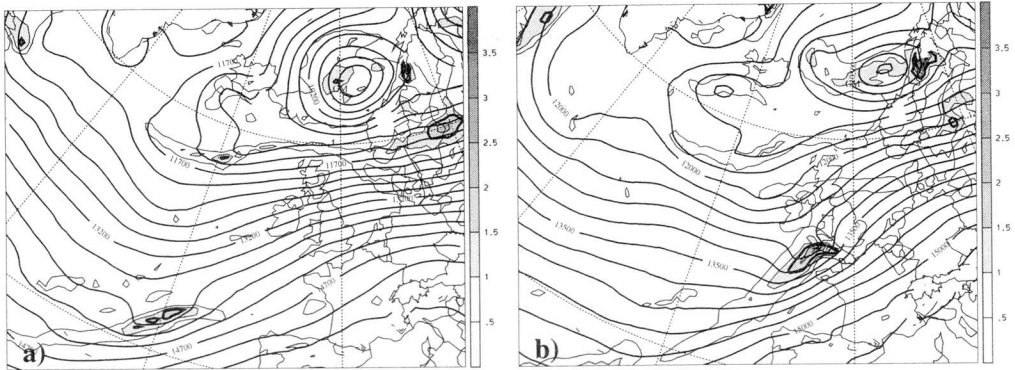


FIG. 5.13: The analogue of Fig. 5.4 but for the revised forecast.

5.3.4 Discussion

This case study demonstrates the feasibility and the potential of the present diagnostic approach for analysing misforecasts. To further illustrate this point we consider here four aspects that arise directly from an intercomparison of the ECMWF analysis, the original EM forecast, and the revised forecast with the modified initial state.

First, consider the original and the revised forecasts. The significant difference between these fields lends credence to the hypothesis that subsynoptic/mesoscale upper-level PV-anomalies can exert a seminal influence upon surface wavecyclogenesis. Furthermore, it indicates that the present approach constitutes an attractive tool for examining predictability aspects of such systems. (As an aside we stress that the role of the upper-level anomalies might be merely catalytic and possibly confined to triggering or modifying the location, timing, or amplitude of the low-level convection. It is clear that the strong low-level PV-signature of this cyclogenesis event is diabatically induced in situ).

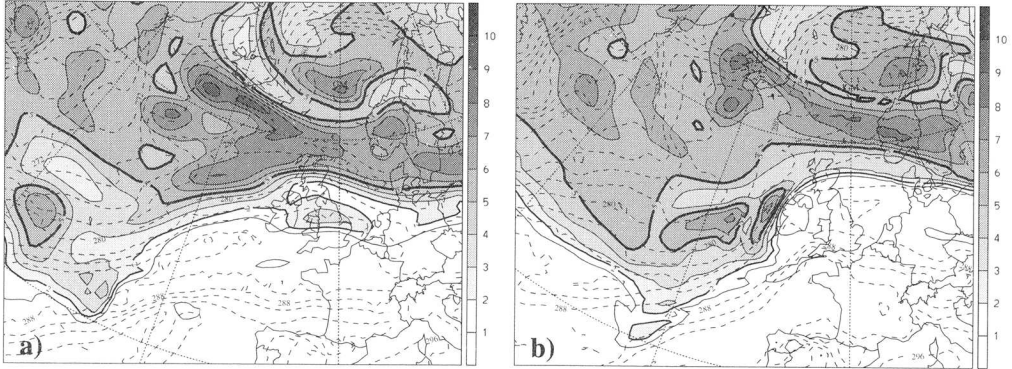


FIG. 5.14: The analogue of Fig. 5.5 but for the revised forecast.

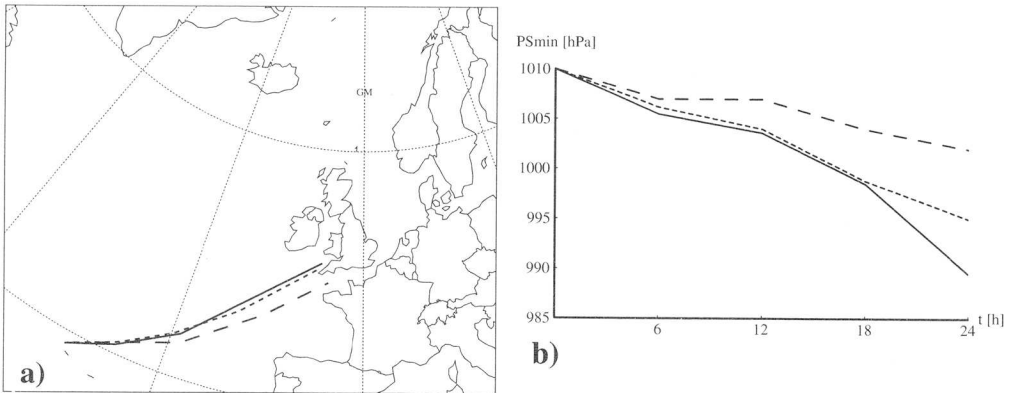


FIG. 5.15: Panel a) shows the track of the cyclone and panel b) the minimum sea-surface pressure. Solid lines correspond to the ECMWF analysis fields, long-dashed lines to the standard EM forecast and short-dashed ones to the revised forecast.

Second, consider the upper-level PV-anomalies in the ECMWF analysis and in the revised analysis at the initial time. The difference in their structure, together with the comparative success of the “revised forecast”, suggests that this difference accounts for a significant component of the error in the initial state. The retrodicted “PV-errors” are fine-scaled and located near the tropopause break and jet stream(s). These factors render their signal less apparent in the in situ geopotential and thermal fields. For example, it is difficult to visually distinguish between the 300hPa geopotential patterns of the ECMWF and the revised analyses, and the quantitative difference amounts to a maximum of about 50 meters at the core of the trough (see Fig. 5.16). The signal associated with the P_1 anomaly can be inferred from Fig. 5.17. The figure shows features of the ECMWF and the revised analysis at 12 UTC on the 12 January in a vertical section aligned across the distinctive PV-filament extending out over the Atlantic. The retrodicted P_1 anomaly directly supplements and intensifies the potential vorticity of this filament, concomitantly reduces (strengthens) by

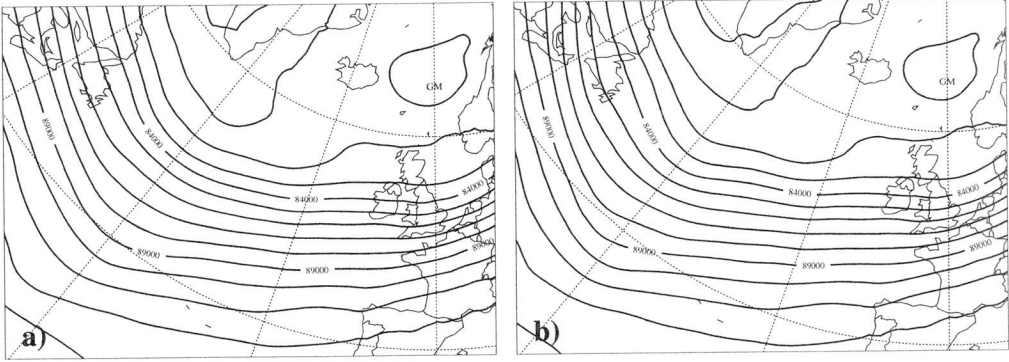


FIG. 5.16: Geopotential (spacing $1000 \text{ m}^2\text{s}^{-2}$) on 300 hPa for the analysis (panel a) and for the revised fields (panel b).

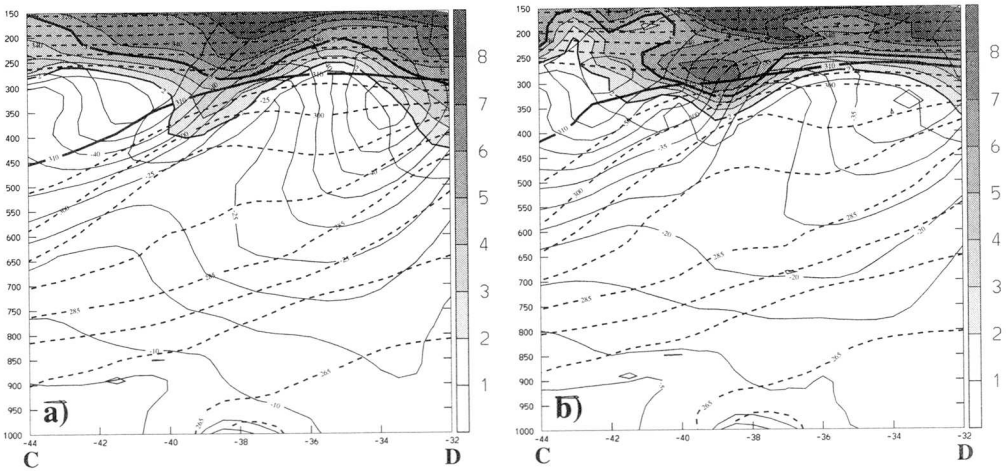


FIG. 5.17: Cross sections at 12 UTC 12 January along the line labeled CD in Fig. 5.3 and 5.11. The section transects the PV filament extending from the western Atlantic seaboard and are derived from (a) the ECMWF initialised analysis and (b) the initial state for the revised forecast. The displayed fields are PV (shaded, spacing 1 pvu, the thick line corresponds to the 2 pvu and the bold to the 5 pvu isoline), potential temperature (dashed lines, thick line indicates 310 K, spacing 5 K for values ≤ 310 K and 10 K for values > 310 K) and cross-velocity field (thin lines, spacing 5 m s^{-1}).

some 10 m s^{-1} the jet stream located to its west (east), and modifies somewhat more weakly the potential temperature field. The vertical penetration of this subsynoptic anomaly is comparatively small and its signal is not apparent below 700 hPa. One inference is that the anomaly's detection is favoured by in situ wind measurements.

Third, consider the structure of the analysed surface event and that simulated in the revised forecast. The reasonable resemblance suggests that the dynamics of the PV anomalies

detected at upper-level relate directly to and can shed light on the nature of the error evolution. In this context consider the dynamics of the two anomalies P_1 and P_3 . From a PV perspective their interaction influences their tracks. For example, it induces a tendency to increase the eastward progression of P_1 and to decrease that of P_3 . This inference is supported, for example, by the velocity signal of the P_1 anomaly as deduced from Fig. 5.17. Likewise P_1 and P_3 can in principle influence the movement and development of the surface low. The evidence of Fig. 5.17 suggests that, at least initially, the influence upon the track is negligible. However, the anomaly P_1 is suitably located to influence the location and strength of the low-level ascent and thereby to instigate and maintain the diabatic processes responsible for the generation of the PV tower.

Further insight, and indeed support, for the foregoing inferences can be gained by applying the method set out in section 5.2 in slightly different forms. Here we record some examples: (a) a simulation based upon the prior retrodiction of only the single anomaly P_1 produced, in comparison with the earlier “standard” experiment, a surface low with a similar structure but a retarded location; (b) a simulation following the retrodiction of a large upper-level envelope encompassing all three anomalies (P_1 , P_2 and P_3) resulted in only a marginally better forecast; and (c) a repeat of the standard simulation but omitting the intermittent PV-inversions during the retrodiction (i.e., performing the backward integration with merely the analysed fields) resulted in a significant misplacement of the cyclone. The latter experiment serves to illustrate the nonlinearity of the error evolution.

Fourth, consider the structure of the upper-level PV anomalies of the revised forecast and the ECMWF analysis at the final forecast time (Figs. 5.5b, 5.14b). It was noted earlier that the revised forecast resulted in a more fragmented P_1 anomaly. This is partly attributable to the revised forecast being based only upon a retrodiction of P_1 and P_3 . Other factors contributing to the difference are one or a combination of the following factors: (i) observational error at the forecast time, (ii) errors arising from numerical and/or physical limitations of the forecast model during the revised forecast, (iii) errors deriving from the four-step diagnostic procedure (in particular the approximations associated with the trajectories and the form adopted for the PV-inversion), and (iv) the incomplete representation of the upper-lower level interactions during retrodiction. None of these factors can be excluded a priori, and their relative contributions are difficult to disentangle since they are coupled during the retrodiction and forecast. The first three factors are in effect technical limitations. The fourth is intrinsic and related to the irreversibility of diabatic and/or rapidly mixing flow, and fragmentation of a PV anomaly is one phase of such mixing.

5.4 Further Remarks

In essence this study indicates that our phenomenological approach is useful for the diagnosis of misforecasts associated with upper-level errors. The adoption of a PV perspective helps to locate the geographical domain of the initial error and provides dynamical insight on the nature of the space-time evolution of that error. In principle the approach can also shed light on some esoteric aspects of predictability and on practical strategies for remedying deficiencies in the analysis.

In the context of predictability, we first note that singular vector analysis of idealised simulations of cyclogenesis (Rabier et al. 1992, Langland et al. 1995) and routine ensemble predictions (Molteni et al. 1996) both indicate that the amplitude of the dominant singular vectors tend to be confined to the lower troposphere. An interpretation is that suitably located small PV perturbations at these elevations can rapidly induce large-amplitude signals in the potential vorticity pattern at tropopause level and in the potential temperature pattern at the surface and that thereafter these induced perturbations could interact synergetically (cf. the quasi-resonant growth documented for an idealised, but related configuration, by Davies and Bishop 1994). Whereas such a mechanism might set the intrinsic predictability limit for initially *linear* atmospheric perturbations, the *preexistence of finite-amplitude* perturbations at tropopause level in realised flows can eliminate the need for, and reliance upon, a low-troposphere perturbation.

The diagnostic approach advocated in this study also has import for the design of adaptive observational strategies. This follows from noting that tropopause-level PV errors can influence the flow field throughout the troposphere, whereas their correction requires only in situ data. In effect, for these forms of error, additional data would be required only in a domain that is limited both horizontally and vertically.

Information related to the location of such domains can be obtained by: (a) routine use of the approach to yield climatological statistics on the frequency and location of PV errors (see next chapter); and (b) quasi-real time inspection of the upper-level PV errors plus frequent retrodictions (of say 12-hours) to provide synoptic patterns of the “current” error.

Improvement of the analysis fields within the presumed error domain can be sought by a more effective use of the time-history of the available data and possibly from appropriate adaptive observational strategies. It is helpful to note that the existence and evolution of tropopause-level flow features that are seminal to surface development are evident in satellite water vapour images (see, e.g., Appenzeller et al. 1996). For the case study reported here we also note that the domain of the initial error is regularly traversed by inter-continental flights of commercial airlines and that upstream over the north American continent there is also a wealth of observational data. However, the efficacy of the latter data is diminished somewhat by the potentially rapid evolution of the upper-level anomalies.

Finally we note that there have been two recent approaches to ameliorating the deficiencies in the initial fields, and both hinge upon the rapid identification of the evolving error fields and the instigation of corrective measures. Rabier et al. (1996) extended their study of the sensitivity of errors in the forecast field to the initial analysis and demonstrated that there is a potential to derive improved forecasts by performing a revised and longer forecast with a suitably modified initial field. Demirtas and Thorpe (private communication) advocate monitoring the satellite water vapour imagery and, in the event of a mismatch with the model’s initial analysis, adjusting the analysed tropopause’s topography to align with the imagery. In a similar vein to these studies, the present approach could also be adapted to provide ongoing pseudo-forecasts by regularly performing short (six- or twelve-hourly) cycles of “forecast – analysis – retrodiction”, followed by an extended revised forecast.

Leer - Vide - Empty

Chapter 6

Climatology of PV-errors

6.1 The Approach

In chapter 5 the PV error was defined as the difference between the PV distribution of the analysis and forecast fields. The retrodiction of such PV errors to the starting time of the forecast can provide information on the nature of the deficiencies in the initial analysis field. Here a climatology is presented of the retrodicted PV error (or short-term PV error) at tropopause levels. Such a statistical analysis can help locate the geographical domain of the deficiencies for a specified integration time and thereby give some indication of the regions where an improvement of the data quality in the initial field is desirable.

There are a number of caveats to be attached this statistical-climatological distribution of PV errors. They relate to the fact that analysis errors are not the only source for a signal in the such defined PV error field. There are also contributions to the PV error from:

- (i) the trajectory calculations,
- (ii) non-conservative physical processes such as diabatic heating,
- (iii) the non-conservation of PV in the adiabatic component of a numerical weather prediction model.

These additional contributions to the error field, even if they are small, occur on a daily basis whereas a significant error due to inaccurate specifications of the analysis field may occur on a time scale of several days. Thus the above listed alternative contributions to the “error” may contribute significantly to the climatology.

In addition to the diagnostic problem posed by different contributions to the error it has also to be noted that the dynamical relevance of a PV error may depend on its location. For example the significance of a local error-anomaly to a forecast will depend on the degree of its interaction with other PV structures. Also it is not the amplitude of an error itself but rather its amplitude relative to the ambient flow that is of dynamical importance.

To partially counter these problems we proceed as follows: *First* we weight the PV error field with a factor that depends on the latitude and altitude. Such a weighting is motivated for example by the inspection of the zonal mean of a PV climatology as displayed in Fig. 2.1. The figure serves to suggest that an error of given amplitude located nearer to the pole and at higher altitudes than another error anomaly is dynamically less important. *Second* we monitor only those errors that are larger than a certain threshold amplitude.

It helps eliminate small errors caused by either discrepancy between the non-conservative PV formulation of the numerical prediction model and the conservative formulation of the Lagrangian advection, or in the trajectory calculations. *Third* we distinguish between the sign of the amplitude in the error field. For example a PV vortex or a streamer that decays with time, would yield a localised negative signal¹. Therefore it may be expected that the negative error field is stronger in amplitude and that differences in the climatological distribution of positive and negative errors stem partly from “real” physical processes and are not only attributable to initial data errors. Furthermore, a phase error would yield a positive and negative signal of similar amplitude and would not contribute to an imbalance between positive and negative errors. On the other hand, a PV error as found in chapter 5 would yield mainly a positive signal in the error field.

Thus a climatology can not only indicate the regions where there is need for improved observational data, but can also help pinpoint those regions where parametrised physical processes have an impact on dynamical quantities, and hence where inadequate parametrisation can contribute to misforecasts.

In this analysis we confine our examination to tropopause level errors. The rationale is that in the troposphere the conservation of PV is often broken by diabatic heating rendering error analysis based on PV difficult. Furthermore the tropopause level dynamics represents a dynamical active zone with small-scale features that can be important for low-level dynamics, whereas the observational data set for this region is relatively sparse.

The 320 K isentropic surface was selected to examine differences between the retrodicted and analysis PV fields. This surface lies in the so called “middle-world” (Hoskins 1991) and intersects the tropopause in midlatitudes. Furthermore we restrict the study to the Atlantic region, i.e. only trajectories starting between 90°W – 30°E and 25°N – 80°N are calculated. The calculations were performed with ECMWF initialised analysis fields interpolated on a 0.75° × 0.75° longitude-latitude grid with a time resolution of 6 hours. The time interval for the retrodiction has been chosen to be 24 hours.

The motivation for a 24 hour time interval comes from the fact that for a longer time interval the contribution to the error as described in (i) – (iii) becomes more important and may hide the contribution from the inaccurate specification of the initial state. For a shorter time interval, on the other side, the additional observations during this time period may only slightly alter the initial state, and again this can result only a small contribution of initial state inaccuracies to the error field. This limits the adopted method to investigate the effect of initial state uncertainties to short range numerical forecasts, but these errors are thought to dominate short range misforecasts.

¹Recall that PV substance is only redistributed by diabatic processes (Haynes and McIntyre 1987). Cloud-diabatic heating will tend to produce negative anomaly rates at tropopause levels and positive anomaly rates in the lower troposphere. A process which can act contrary to heating, i.e. which increases the tropopause level PV and decreases the tropospheric PV is radiation. This process acts on a much larger domain than the cloud-diabatic heating process but is also weaker, and acts on a longer time scale.

6.1.1 Error Measures

Two possible candidates for a weighted PV error measure are assessed against the “difference-parameter”

$$Q_{err} = Q_{ret} - Q,$$

where Q_{ret} and Q are respectively the retrodicted, and analysis PV fields. The first corre-

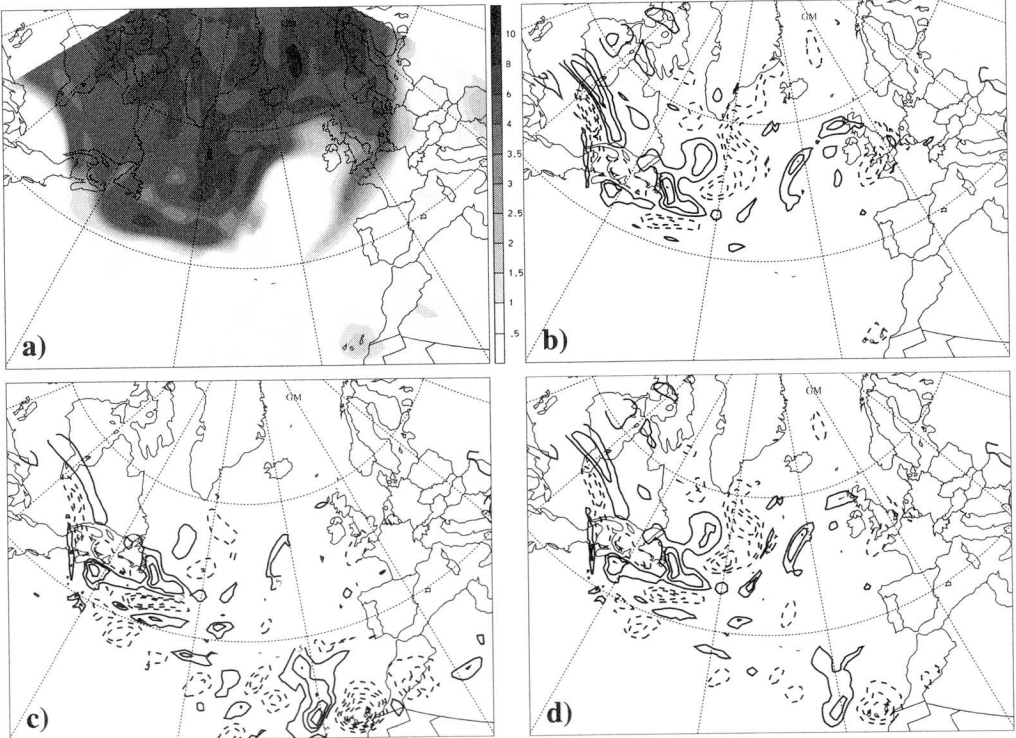


FIG. 6.1: Measures of PV error based on the various definitions introduced in the text. The displays correspond to the PV distribution (panel a) on the 320 K isentrope, and the corresponding Q_{err} , e_z , and e_f fields (panels b–d). Solid (dashed) lines indicate positive (negative) errors with spacing 1 pvu for b), 0.5 for c) and 1 for d).

sponds to a weighting of the PV differences by a monthly-mean zonal PV

$$e_z = \frac{Q_{err}}{Q_{zon}},$$

where $\overline{Q_{zon}}$ represents the monthly zonal mean of the PV distribution. The second candidate is defined by

$$e_f = \frac{Q_{err}}{Q_0}.$$

Here \overline{Q}_0 denotes a ten-year northern hemispheric mean which depends only on altitude. Note that both, but especially e_r , are related to the free PV charge as introduced by Thorpe and Bishop (1995).

Fig. 6.1 displays a typical isentropic PV distribution of Q_{err} , e_z , and e_r . The error field Q_{err} is confined between 40°N and 65°N. Strongest values can be observed in the region of the trough over the western Atlantic. The positive and negative amplitudes have a maximum of 3 pvu (panel b). Some of the anomalies occur in pairs, e.g. the elongated almost west-east orientated positive and negative anomalies over Canada, and can be linked to a phase shift between the analysis and the retrodiction field. For the e_z measure, low latitude anomalies are much stronger weighted than high latitude anomalies (panel c), and only anomalies south of 50°N give a significant contribution. The e_r field contains anomalies north and south of the 40°N parallel. We do not consider e_z any further.

The threshold value for the mean calculations have been chosen to be 1.5 pvu for the Q_{err} field and 1 for e_r .

6.2 Results

In this section we compare the PV error distribution with the regions where synoptic scale eddies in the extratropics are statistically most prevalent and intense. For the winter season two such regions have been identified in the northern hemisphere – over the Pacific and the Atlantic oceans downstream of the respective winter mean jet streams (see, e.g., Blackmon et al. 1977). These so-called storm tracks have been defined in terms of the height-field variance. Here it is appropriate to compare the PV error on a specific isentropic surface with the PV variance on the same surface. Fig. 6.2 shows the northern hemispheric mean PV

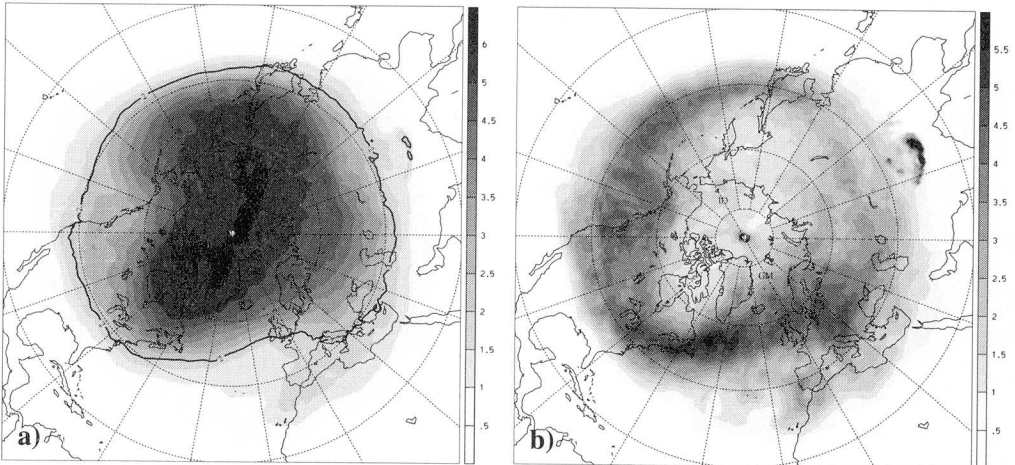


FIG. 6.2: Winter 1993 mean PV distribution on the 320 K surface (panel a) and PV variance (panel b) indicating the storm track for the northern hemisphere. The spacing is as indicated, and in panel a) the 2 pvu isoline is overlaid.

distribution and the PV variance, both on the 320 K surface, for winter 1993. Inspection of the 2 or 5 pvu isolines in the PV mean distribution identifies two large scale troughs with associated maxima of the isentropic PV gradients. These are centered respectively on the eastern coastline of the Asian and American continents. These two regions are also associated with maxima in the climatological zonal wind and meridional temperature gradient. Downstream of these two regions are the zones of maximal eddy activity, indicated by the PV variance, cf. the Pacific and Atlantic storm tracks. The eddy activity weakens over the eastern oceans, and there the PV variance is diffluent. For this particular winter the Atlantic storm track is slightly more intense than the Pacific storm track, and the Atlantic track has (compared with the Pacific) a more northward alignment.

6.2.1 The Seasonal Analysis for 1993

For the year 1993 we calculate the mean of PV errors for every season (DJF, MAM, JJA, SON). Recall that by the restriction of the data to a sector including the northern Atlantic, some of the data will advect out of this domain and therefore at each time there will be a limited area with no available error field. Only those sectoral points where the error could be calculated for at least 75% of the cases have been taken into account for the seasonal mean.

Winter Season

Strongest PV errors occur near the maximum in the isentropic PV gradient over the north eastern part of the American continent (see Fig. 6.3). This region coincides with the entrance of the Atlantic storm track (panel f). Positive Q_{err} and e_f errors exhibit a similar distribution. For negative errors beside the analogue of the positive errors, there is also a strong anomaly over south of Spain. This anomaly can be linked to streamers and cut-offs decaying diabatically over the European continent. Such streamers occur frequently on the longitudinal boarder of large scale anticyclones (Appenzeller et al. 1996). Streamers east of the anticyclone often stretch from north to south-west and subsequently curve anticyclonically around the south-western side of the anticyclone. Typically these streamers break up into a family of sub-vortices by an instability process akin to that studied in chapter 3. Sorts of blocking PV anomalies can here be identified in the PV mean distribution. Note that both, positive and negative errors are comparatively weak near the maximum of the eddy activity, south of Greenland, but the negative PV errors, south of Spain, are collocated with a corresponding anomaly in the PV variance distribution.

Spring Season

Here the mean PV distribution has an equatorward undulation extending from Iceland to Spain (Fig. 6.4), with associated strong eddy activity (panel f). The latter features have counterparts in the negative PV error distribution (see panel b and d). Note, for example, the correspondence on the mesoscale of the anomaly signal over Spain and over Corsica in the Q_{err} , e_f , and the PV variance. There is a discrepancy between positive and negative

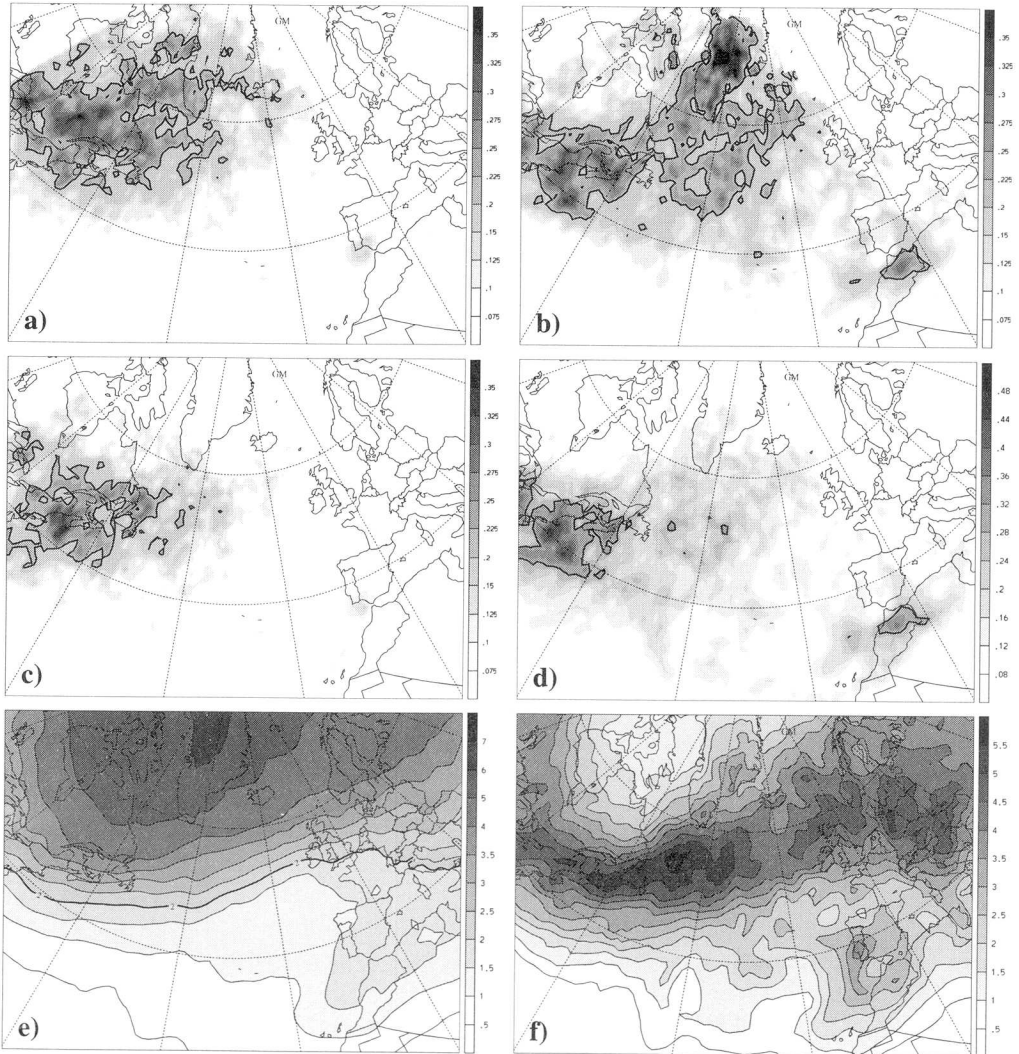


FIG. 6.3: Climatology of PV errors for Winter 1993. Shown are positive and negative Q_{err} errors (panel a and b), and positive and negative e_{err} errors (panel c and d). For each field a different spacing (as indicated) has been chosen, superimposed are the 0.2 pvu isolines (panel a and b) and the 0.2 and 0.32 isolines (panel c and d). In panel e) and f) the mean PV and the variance are displayed.

errors not only over the eastern Atlantic, but also over the northern American continent. For example, there is a negative anomaly over Newfoundland (panel b or d), and a strong positive anomaly over Labrador (panel a or c).

The PV errors over the western Atlantic ocean/eastern American continent are much

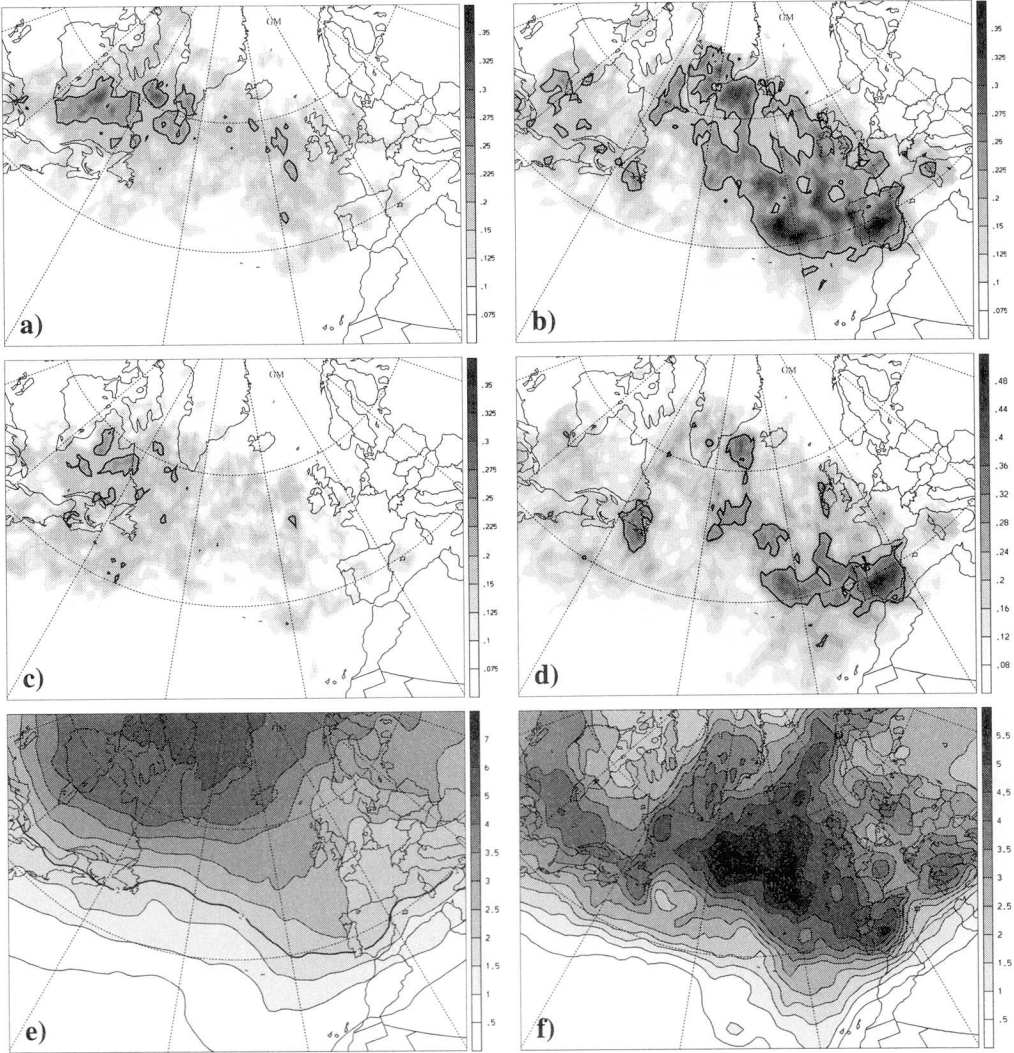


FIG. 6.4: The analogue of Fig. 6.3 but for Spring 1993.

weaker than the corresponding errors for wintertime.

Summer Season

The results for the summer season are shown for completeness (Fig. 6.5). Now the 320 K surface is in midlatitudes in the troposphere and therefore diabatic processes, e.g. convection, can influence the PV error.

Positive and negative errors are both centered over the northern mid-Atlantic. The strong

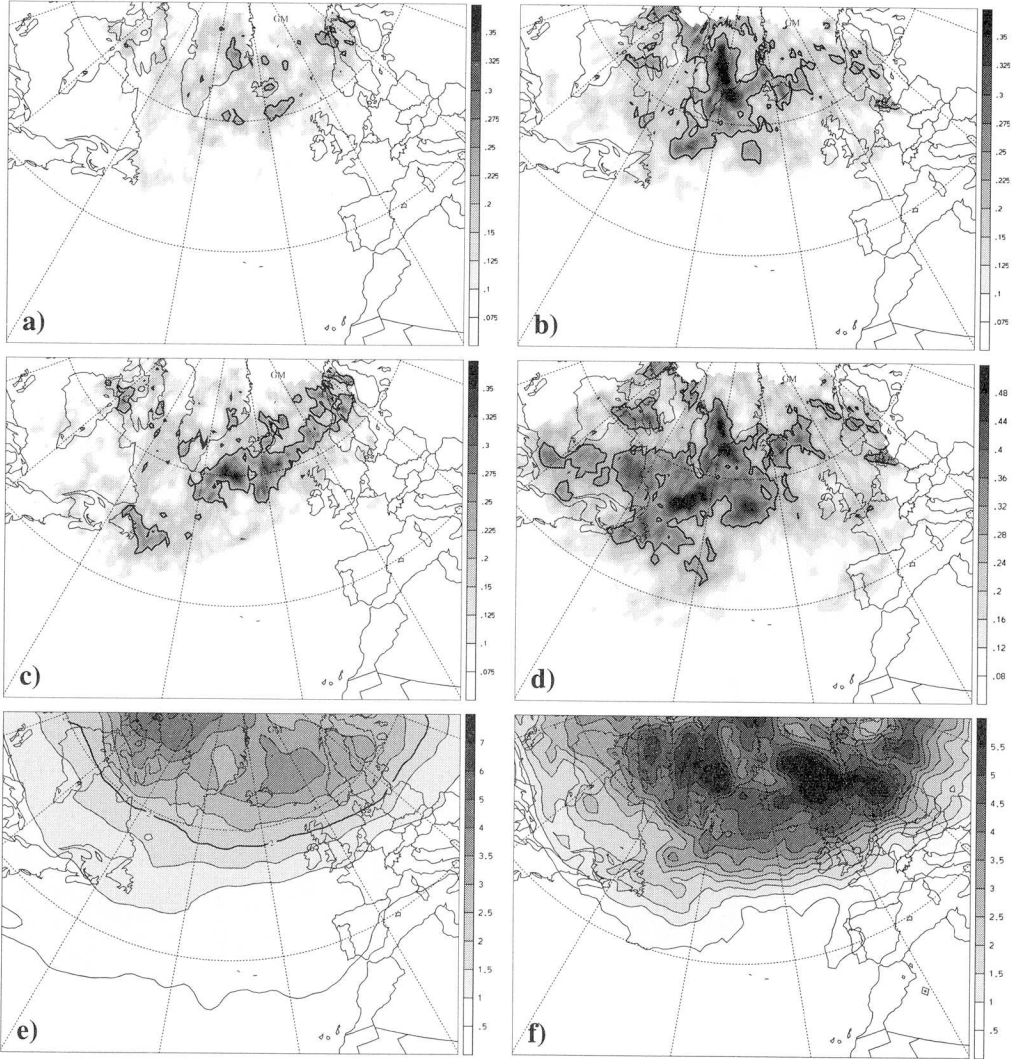


FIG. 6.5: The analogue of Fig. 6.3 but for Summer 1993.

northward shift of the Q_{err} field can be explained by the tropospheric location of the 320 K surface. The negative error distribution is stronger in amplitude than the positive, again indicative for the contribution of diabatic processes to the error field. No clear large scale extrema in the isentropic PV gradient can be observed.

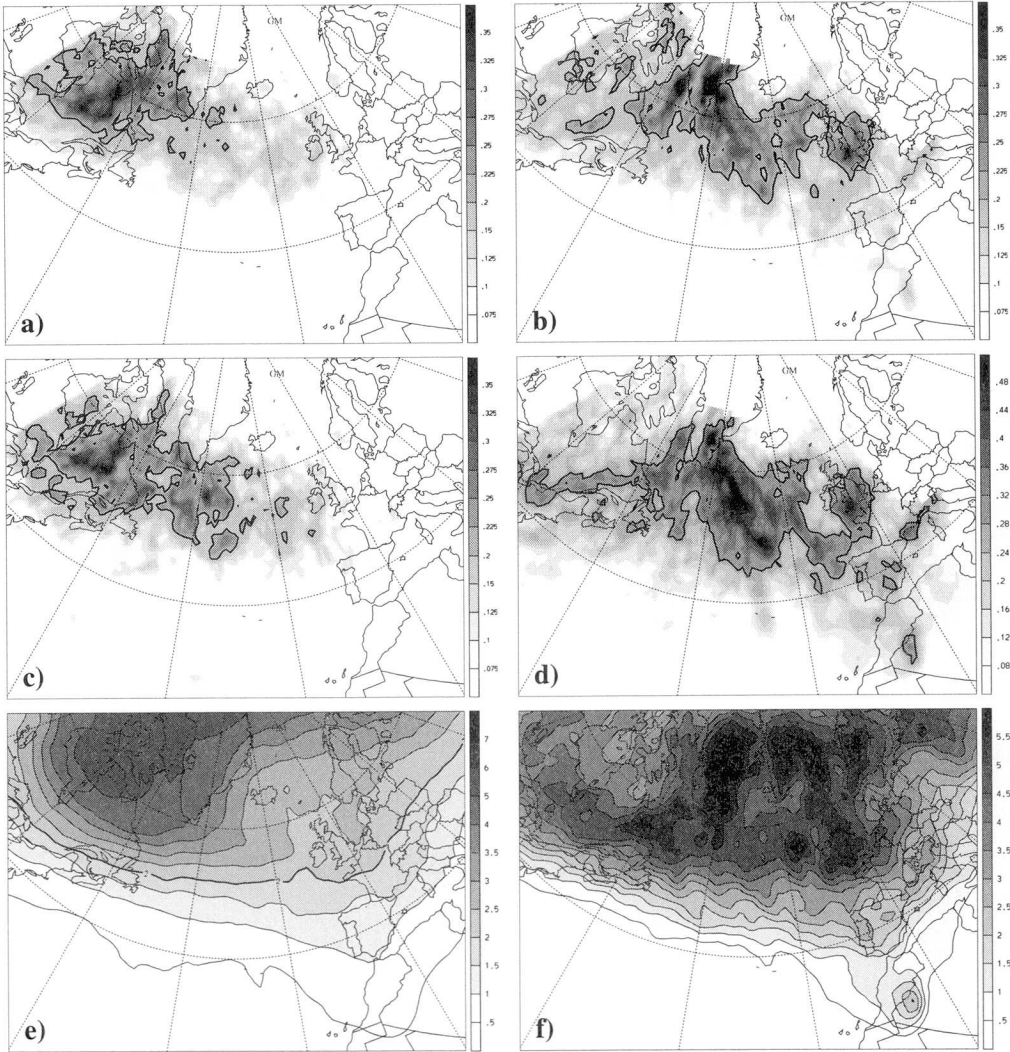


FIG. 6.6: The analogue of Fig. 6.3 but for Autumn 1993.

Autumn Season

A notable feature of the mean PV distribution in this season is the weaker latitudinal PV gradient over western Europe and the strong latitudinal PV gradient over the north western American continent (Fig. 6.6). The storm track starts near the maximum of the latitudinal PV gradient, is strongly diffluent, and exhibits an isolated vortex-like structure south of the Atlas mountains.

Again, negative PV errors can be linked to the PV variance (panel d), the negative PV

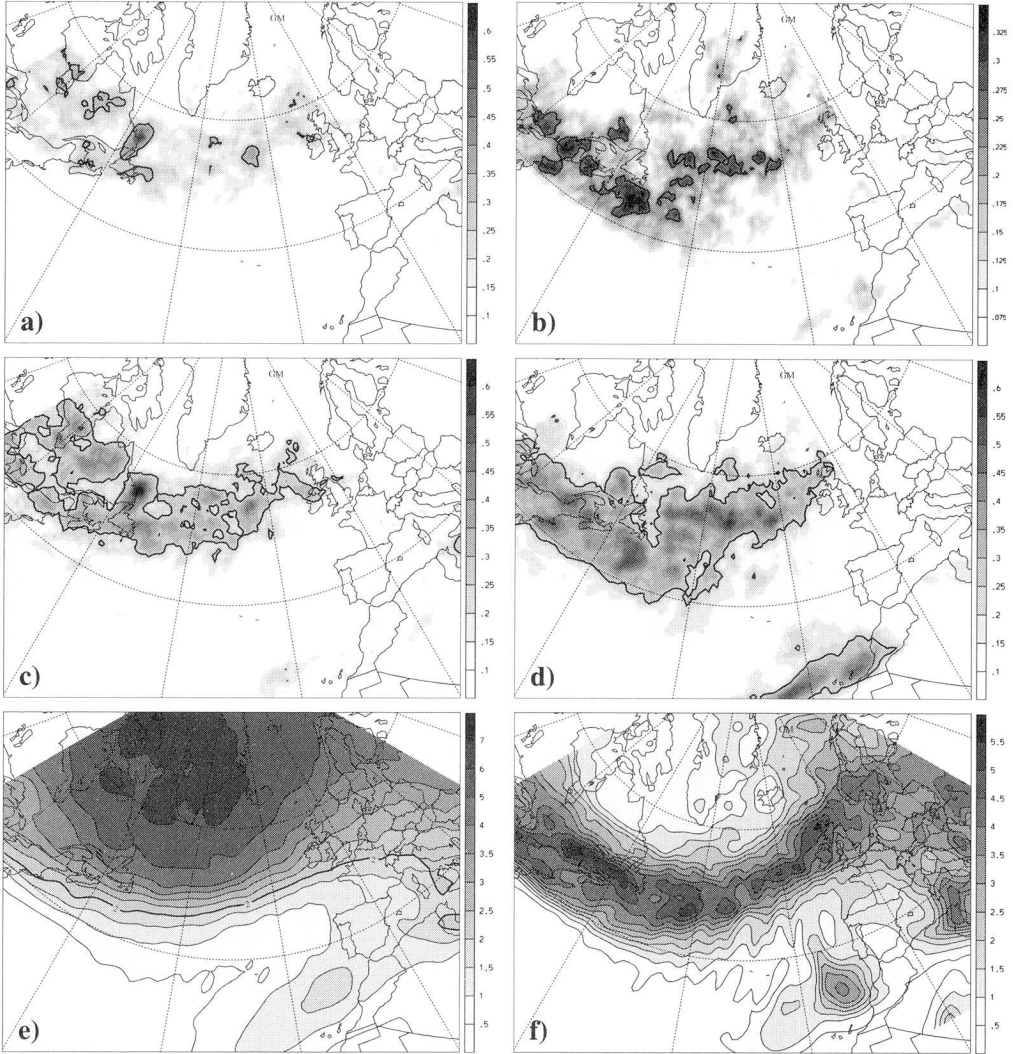


FIG. 6.7: Climatology of PV-errors for February 1997.

distribution is diffuent, with a maximum extending south of Greenland almost down to the Azores. The positive errors are mainly confined west of 30°W with a maximum over Labrador, and are in this region stronger than the negative errors.

6.2.2 The Period of February 1997 – FASTEX Cases

A similar climatology has been computed for February 1997 – the second half of the FASTEX observational programme. The results are shown in Fig. 6.7. (Note that a different spacing

than in the analogous figures for the 1993 calculations has been used.)

The mean PV distribution has its strongest latitudinal PV gradient around 40°W , and there is a tongue of high PV extending south-westward from southern Europe. The peak of the PV variance is west of 40°W at $\sim 50^{\circ}\text{N}$ and the track drifts downstream northward to $\sim 60^{\circ}\text{N}$.

Again, PV errors can be linked to the eddy activity. Compared with the analogous PV error field of winter 1993, the errors are here centered slightly further south. The strong positive error anomaly centered at about $55^{\circ}\text{N}/58^{\circ}\text{W}$ (panel a or c) has a contribution from the PV retrodiction valid for 06 UTC 9th, 12 UTC 14th, 06 UTC 18th, and 06 UTC 21th. In fact a distinct misforecast occurred in the 36 hour ECMWF forecast valid for 00 UTC 20th with respect to a frontal wave cyclone located north of Scotland. A detailed case study of this misforecast, as in chapter 5, would help to elucidate the cause of this misforecast, and a possible factor could be the strong PV error at 06 UTC 18th.

6.3 Discussion

The attribution of forecast failure to either initial state inaccuracies or to the formulation of a NWP model is often difficult to achieve. Current understanding is that errors in the specification of the initial state play a more important role for short range weather forecasts, whereas model errors become more important in the medium range (see, e.g., Tribbia and Baumhefner 1988, Simmons et al. 1995). Here an attempt was made to make a statistical analysis of initial analysis errors via the concept of PV retrodiction. This can help to locate, for a specific forecast time, the geographical domain where upper-level errors frequently occur and can thereby provide guidance as to the need for additional observational data.

For the Atlantic storm track region, it has been found not unexpectedly that the latitudinal distribution of errors is linked to the region of strongest eddy activity. The error distribution has a maximum near the entrance of the storm track, and is strongest in Autumn and Winter. But note that the correspondence of PV error and PV variance is not one-to-one, e.g. in the wintertime error climatology the strongest signal in the PV error is upstream of the maximum in the PV variance.

Besides the earlier noted caveats of such an analysis, one has also to note that this one-year analysis can merely provide some indication of the proposed strategy's utility. In a subsequent study it would be necessary to take into account the following points:

- (i) The use of higher temporal resolution of the data for the trajectory calculations can reduce the contribution to the error field of inaccurate advection. This contribution might well be related to the regions of strong eddy activity. This region in turn has been found to be where PV errors most likely occur.
- (ii) The quality of the PV advection technique by Lagrangian trajectory calculations can be tested by applying it to idealised simulations with an adiabatic version of a numerical model. In such an analysis the contribution to the error field caused by the non-conservative numerical formulation of the PV advection or the inaccuracies of the here used Lagrangian advection technique can be estimated.
- (iii) Here we made a statistics of all errors irrespective of causing a misforecast. A selective

statistical analysis, e.g. by monitoring only those errors prior to an unskillfull forecast can, for example, eliminate the error signal due to diabatical processes.

- (iv) The statistical analysis could be performed for different periods including various operational data assimilation procedures. The improved assimilation techniques should be reflected in our PV error climatology, and this can indicate the ability of this technique to identify analysis errors.
- (v) More sophisticated statistical methods can be applied to study the relationship between the PV error field and the storm tracks (e.g. EOF's of the error field and the eddy PV field and SVD's). This can further help pinpoint the cause(s) of errors in the initial data.

Chapter 7

Further Remarks

In this thesis aspects of the dynamics of PV elements linked to midlatitude cyclones have been studied in a variety of settings. These include a highly idealised framework, with quasi-geostrophic and primitive equation dynamics, and a more realistic setting with case study simulations with a numerical weather prediction model. The focus of the idealised studies has been upper and lower anomalies associated with PV bands. Investigation of the nonlinear evolution of such bands with a hierarchy of models can illustrate the roll-up and break-off features of these bands, stratosphere-troposphere mass exchange associated with the nonlinear evolution of these anomalies, interaction mechanisms, and the connection of the dynamical structure of elongated stratospheric intrusions with the direct observational data (e.g. water vapour images). These studies confirm and extend earlier work (e.g. Held et al. 1995, Wirth et al. 1997), and the emphasis here was to compare primitive equation internal PV anomalies with *quasi-geostrophic surface anomalies*.

The PE model simulations of elliptical stratospheric intrusions demonstrate that their development exhibits different characteristics at different heights, i.e. there is a degree of non-coherency in the vertical. The roll-up mechanism, a common feature at a certain horizontal level in the primitive equation simulations of an idealised PV streamer, could not be observed in the analogue SQG framework.

Interest of elongated stratospheric intrusions comes also from other atmospheric phenomena. Rossa (1995) noted that in the flood in Brig, Switzerland, in late September 1993, and in the flood event in the region of Piedmont, Italy, at the beginning of November 1994, intense elongated, North-South orientated upper-level PV anomalies could be observed which are likely to have influenced these heavy precipitation events. Massacand (personal communication) pointed out that other flood events in the southern Alpine region are linked to very similar PV structures. These anomalies have a typical length of ~ 1500 km, width ~ 250 km, and an amplitude of $\sim 6 - 8$ pvu on the 320 K isentropic surface (compared with $\sim 0.5 - 1$ pvu of the environment of the strip). In Fig. 7.1 the evolution of the PV distribution on the 320 K isentropic surface for the Piedmont case is displayed. Note that the strip was located during more than 2 days over the Alpine region, thinned and broke up into two vortices. A PV-inversion of this anomaly indicates the contribution of the wind field to the low-level jet, which in turn was responsible for the strong persistent moisture flux from the Mediterranean to the Alps.

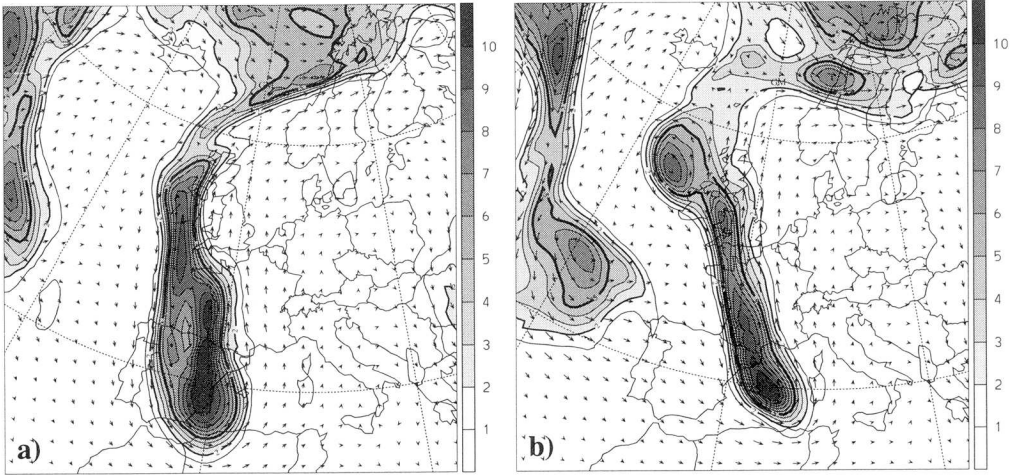


FIG. 7.1: Evolution of the upper-level PV anomaly for the Piedmont flood. Shown is the PV distribution on 320 K (shaded, spacing 1 pvu), and velocity vectors on the same isentropic surface valid for 12 UTC November 5 (panel a) and 00 UTC November 6 1994 (panel b).

Possible dynamical contributions to the precipitation of these structures include (i) a reduction of the stratification and therefore the stability in the vicinity of the anomaly, (ii) a vertical motion induced by instability process as described in chapter 3, (iii) contribution to the low-level jet, and (iv) their persistent location in connection with an advection of moist air to the southern Alpine region. The techniques used in this thesis offer the possibility to further investigate tropopause-level flow structures of these flood events.

The case studies of frontal wave developments, as presented in chapter 4 and 5, indicate that the influence of condensational processes on the low-level PV structures as well as the interaction of these PV structures with upper-level PV elements may significantly act on the development of secondary cyclones. The case-to-case variability in the most important contributions to the dynamical evolution of these weather systems may be one reason why some frontal waves develop into full blown storms where others decay on a comparatively short time scale.

Besides the purely academic interest in the relevant mechanisms contributing to the dynamics of rapid developing storms there is also need to increase the skill in forecasting such storms. PV retrodiction is one method that has the potential to both, improve our understand of the basic mechanisms involved in the development of extratropical cyclones, and can also propose strategies to improve numerical weather forecasts. The statistical application of this method suggests that for short-range forecasts of stipulated time there is need of improved observational tropopause level data in the region marked by the entrance of the Atlantic storm track.

Idealised studies of observational data improvements, in a similar way as undertaken by Houtekamer and Derome (1994) with the three level, global quasi-geostrophic spectral model of Marshall and Molteni (1993), in combination with a statistical diagnosis via PV retrod-

iction can point on the limitations of the generality of the proposed strategy. For example one could perform simulations where the observational data set is generated with a Monte Carlo method. This would allow the simulation of arbitrary regions of poor observational quality which than should be identified by the retrodiction method.

One of the main purposes of this thesis was to demonstrate the dynamical importance of PV structures. As a consequence we note that it might be of interest to use a PV related norm in calculating singular vectors to indicate regions where small perturbations are most likely to grow. Such an analysis has been performed by Joly (1995) for an idealised warm surface band in a baroclinic atmosphere. For example, the expressions of the various norms expressed by the streamfunction of the quasi-geostrophic model, are given by:

$$\text{the energy norm:} \quad \|\psi'\|_e^2 = \frac{1}{G} \int_G \nabla\psi' \cdot \nabla\psi' dG$$

$$\text{the enstrophy norm:} \quad \|\psi'\|_v^2 = \frac{1}{G} \int_G \Delta_n\psi' \Delta_n\psi' dG$$

$$\text{the PV norm:} \quad \|\psi'\|_q^2 = \frac{1}{G} \int_G \Delta\psi' \Delta\psi' dG,$$

where ψ represents a reference state, ψ_p a perturbed state and $\psi' = \psi - \psi_p$ the error. It is clear, from the definition of the norms, that they lead to different weighting of the scales of the systems. The PV norm will focus more on the small scale structures. It would be of interest to compare the structures that have strongest growth in the tangent linear model approach (based on different norms, such as the energy, enstrophy or the PV norm) with the structures of the PV error of a misforecast introduced in this thesis.

Leer - Vide - Empty

Appendix A

Potential Vorticity Inversion

As noted in Hoskins et al. (1985) the invertibility principle needs the spatial distribution of the PV, suitable boundary conditions, and a specification of some further dynamical principle: “Regardless of which theoretical device is used for the inversion, one must

- (i) specify some kind of balance condition, the simplest albeit least accurate being ordinary geostrophic balance;
- (ii) specify some kind of reference state, expressing the mass distribution of θ , in essentially the same way as in Lorentz’s theory of available potential energy; and
- (iii) solve the inversion problem globally, with proper attention to boundary conditions.”

Here a presentation is made of one approach to the inversion problem. It entails a specification of geostrophic balance and a Boussinesq reference state. In addition the numerical algorithm is provided to solve the resulting mathematical problem.

A.1 Mathematical Formulation of the Problem

The PV inversion technique used in the present study for both the idealised and real case studies is based on the quasi-geostrophic approximation. In this limit the relative potential vorticity and the boundary conditions are given by:

$$q = \frac{\partial^2 \psi}{\partial x^2} + \frac{\partial^2 \psi}{\partial y^2} + \frac{f^2}{\rho_0} \frac{\partial}{\partial z} \left(\frac{\rho_0}{N_0^2} \frac{\partial \psi}{\partial z} \right) \quad (\text{A.1})$$

$$\text{with } \left. \begin{aligned} g \frac{\theta^*}{\theta_0} &= f \frac{\partial \psi}{\partial z} \\ u &= - \frac{\partial \psi}{\partial y} \\ v &= \frac{\partial \psi}{\partial x} \end{aligned} \right\}. \quad (\text{A.2})$$

Here N_0^2 , ρ_0 and ψ denote respectively the Brunt-Väisälä frequency, the density of the Boussinesq reference state and the streamfunction. Note that, in contrast to the formulation in section 2.2, the assumption of a constant density throughout the atmosphere is abandoned.

In the idealised studies the Boussinesq reference state is determined through a definition of the Brunt-Väisälä frequency $N_0^2(z)$. An integration of the relation

$$N^2 = \frac{g}{\theta} \frac{\partial \theta}{\partial z} \quad (\text{A.3})$$

yields the reference potential temperature:

$$\theta_0(z) = \Theta \exp\left(\frac{1}{g} \int_{z_0}^z N_0^2(z) dz\right) \quad (\text{A.4})$$

where $\Theta = \theta_0(z = z_0)$. From the idealised gas law

$$p = \rho RT$$

and the definition of the potential temperature

$$\theta = T \left(\frac{p_s}{p}\right)^\kappa$$

where $\kappa = R/c_p \approx 2/7$ for the atmosphere and $p_s = 1000$ hPa one can eliminate the temperature and gets

$$\rho_0 = \frac{p_0}{R\theta_0} \left(\frac{p_s}{p_0}\right)^\kappa.$$

If we put this expression for the reference density into the hydrostatic assumption

$$\frac{\partial p}{\partial z} = -g\rho$$

we have an expression

$$\frac{\partial p_0}{\partial z} = -\frac{p_0^{1-\kappa} p_s^\kappa g}{R\theta_0}$$

which can be integrated to

$$p_0(z) = p_0(z_0) \left(1 - \frac{\kappa g}{R} \left(\frac{p_s}{p_0(z_0)}\right)^\kappa \int_{z_0}^z \frac{d\zeta}{\theta_0(\zeta)}\right)^{1/\kappa}. \quad (\text{A.5})$$

In the real case studies the Boussinesq reference state is determined by an average of the potential temperature on isosurfaces of the geopotential. This serves to define N_0^2 via equation (A.3). From the potential temperature and the stratification (N_0^2) the density (ρ_0) is calculated.

The problem posed by equation (A.1) with boundary conditions (A.2) constitutes a Neumann boundary value problem. It only has a solution if some further condition between the PV distribution and the boundary values is fulfilled. This compatibility condition of the interior PV distribution and the boundary values follows from Gauss' theorem. To demonstrate this define a new vertical coordinate such that the quasi-geostrophic PV q can

be expressed as the divergence of a vector-field \mathbf{E} (this is one part of the electrostatic analogy (Bishop and Thorpe 1994c)). Let

$$\zeta(z) := -\frac{p_0(z)}{gf^2} \quad \text{and} \quad \Delta_h = \frac{\partial^2}{\partial x^2} + \frac{\partial^2}{\partial y^2}$$

i.e. ζ is a scaled pressure coordinate, then we have, from the hydrostatic assumption $\frac{\partial \zeta}{\partial z} = \frac{\rho_0}{f^2}$, and hence the following expression for q

$$q = \Delta_h \psi + \frac{\partial}{\partial \zeta} \left(\frac{\rho_0^2}{f^2 N_0^2} \frac{\partial \psi}{\partial \zeta} \right).$$

From Gauss' theorem we obtain the relationship

$$\int_G q \, dx \, dy \, d\zeta = \int_{\partial G} \mathbf{E} \cdot d\boldsymbol{\sigma} \quad (\text{A.6})$$

where $\mathbf{E} = \left(\partial_x \psi, \partial_y \psi, \frac{\rho_0^2}{f^2 N_0^2} \frac{\partial \psi}{\partial \zeta} \right)$ (note that the integration has to be carried out in the coordinate system (x, y, ζ)). Let now B be any two-dimensional domain in the (x, y) -plane and $G = B \times [z_a, z_b]$ in the Cartesian space. We can transform the compatibility condition back into the Cartesian coordinate system and split the integration over the boundary of the domain G into an integration over the surface, the lid and the lateral boundaries of the domain. It then follows that

$$\begin{aligned} \int_G \rho_0(z) q(x, y, z) \, dx \, dy \, dz &= \int_{z_a}^{z_b} \left(\oint_{\partial B} \mathbf{v}(x, y, z) \cdot d\mathbf{r} \right) \rho_0(z) \, dz - \\ &\int_B \frac{\rho_0(z_a) g f \theta^*(x, y, z_a)}{\theta_0(z_a) N_0^2(z_a)} \, dx \, dy + \int_B \frac{\rho_0(z_b) g f \theta^*(x, y, z_b)}{\theta_0(z_b) N_0^2(z_b)} \, dx \, dy \end{aligned} \quad (\text{A.7})$$

Only if this condition is fulfilled does there exist a unique solution (up to a constant). This means that not every formulation of the inversion problem needs to have a solution. This issue is not yet fully clarified for other nonlinear inversion formulations, i.e. besides the condition of positive PV values there might be some additional conditions which need to be fulfilled to have a solution of the nonlinear inversion problem of Davis (1992).

A.2 Discretization and Numerical Algorithm

An elliptical PDE of the form

$$\frac{\partial}{\partial x} \left(\alpha \frac{\partial \psi}{\partial x} \right) + \frac{\partial}{\partial y} \left(\beta \frac{\partial \psi}{\partial y} \right) + \frac{\partial}{\partial z} \left(\gamma \frac{\partial \psi}{\partial z} \right) + \sigma = 0$$

can be discretised as

$$\Delta_x(A\Delta_x\psi) + \Delta_y(B\Delta_y\psi) + \Delta_z(C\Delta_z\psi) + S = 0$$

state grid. For simple examples of the stratification N^2 the integration can be carried out analytically. Fig. A.2 compares the analytical and numerical solution of the reference density for an atmosphere with constant stratification $N^2 = 10^{-4}\text{s}^{-1}$. The relative error $(\rho_0^n(z) - \rho_0(z))/\rho_0(z)$, where $\rho_0(z)$ is the exact and $\rho_0^n(z)$ is the numerical solution, is less than 0.5%.

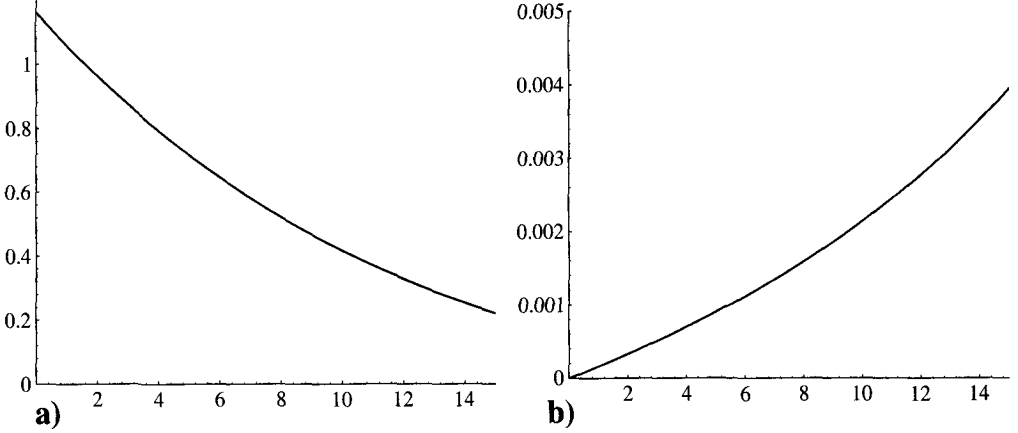


FIG. A.2: Reference density of an atmosphere with constant stratification $N_0^2 = 10^{-4}\text{s}^{-1}$. Panel a) analytical solution, panel b) relative error of the numerical solution.

Let $\rho(k) := \rho_{k/2}$ and $N^2(k) = N_{k/2}^2$. With these definitions we get for the coefficients of the inversion problem:

$$A_k = \frac{\Delta y \Delta z}{\Delta x} \rho(2k), B_k = \frac{\Delta x \Delta z}{\Delta y} \rho(2k) \quad k = 0, \dots, nz$$

$$C_k = \frac{\Delta x \Delta y}{\Delta z} \frac{\rho(k) f^2}{N^2(k)} \quad k = 0, \dots, 2nz, C_{-1} := C_0, C_{2nz+1} := C_{2nz}$$

$$S_{i,j,k} = -\Delta x \Delta y \Delta z \rho(2k) q_{i,j,k} \quad i = 0, \dots, nx, j = 0, \dots, ny, k = 0, \dots, nz$$

and the discretised PV-equation is

$$A_k (\psi_{i-1,j,k} - 2\psi_{i,j,k} + \psi_{i+1,j,k}) + B_k (\psi_{i,j-1,k} - 2\psi_{i,j,k} + \psi_{i,j+1,k}) \\ + C_{2k-1} \psi_{i,j,k-1} - (C_{2k-1} + C_{2k+1}) \psi_{i,j,k} + C_{2k+1} \psi_{i,j,k+1} = \Delta x \Delta y \Delta z \rho(2k) q_{i,j,k}$$

for $i = 0, \dots, nx$, $j = 0, \dots, ny$ and $k = 0, \dots, nz$. The values of ψ in an additional boundary layer (e.g. $\psi_{-1,j,k}$) have to be eliminated by the discretised Neumann boundary condition

$$A_k (\psi_{0,j,k} - \psi_{-1,j,k}) = \Delta y \Delta z \rho(2k) v_a(j, k) \\ A_k (\psi_{nx+1,j,k} - \psi_{nx,j,k}) = \Delta y \Delta z \rho(2k) v_b(j, k) \\ B_k (\psi_{i,0,k} - \psi_{i,-1,k}) = -\Delta x \Delta z \rho(2k) u_a(i, k) \\ B_k (\psi_{i,ny+1,k} - \psi_{i,ny,k}) = -\Delta x \Delta z \rho(2k) u_b(i, k)$$

$$\begin{aligned}
C_{-1}(\psi_{i,j,0} - \psi_{i,j,-1}) &= \Delta x \Delta y \frac{fg\rho(0)\theta_{bot}(i,j)}{N^2(0)\theta_0(0)} \\
C_{2nz+1}(\psi_{i,j,nz+1} - \psi_{i,j,nz}) &= \Delta x \Delta y \frac{fg\rho(2nz)\theta_{top}(i,j)}{N^2(2nz)\theta_0(2nz)}
\end{aligned}$$

This is a system of linear equations which can be expressed as $B\psi = b$, where B is a $m \times m$ -matrix with $m = (nx + 1)(ny + 1)(nz + 1)$. The matrix B has at least a one dimensional kernel ($\psi_{i,j,k} = 1, \forall i, j, k$), which can easily be checked. This means that the image of the operator represented by B is at most $(m - 1)$ -dimensional. Because the linear operator is normal the image is orthogonal to the kernel, thus the vector b (its entries are the PV and the boundary values) is in the image and the discretised PV-equation has a solution if

$$\sum_{i,j,k} b_{i,j,k} = 0$$

This gives exactly the discrete version of the compatibility condition (A.8). In practice this condition is achieved by adding to the boundary distributions of the potential temperature at the surface and the lid a constant value of opposite sign. For reasonable PV and temperature distributions this additional temperature is less than 2 K.

We solve the linear equation with a successive overrelaxation (SOR) method: Let A be an operator i.e. an $m \times m$ -matrix and $\omega \in R$ such that $\|1 - \omega(1 + A)\| < 1$ then there exists the limit $n \rightarrow \infty$ of

$$\psi_i^{(n+1)} = \omega \left(b_i - \sum_{j=1}^i A_{ij} \psi_j^{(n+1)} - \sum_{j=i+1}^m A_{ij} \psi_j^{(n)} \right) + (1 - \omega) \psi_i^{(n)} \quad (\text{A.8})$$

for any $\psi^{(0)}$ and is the solution of $A\psi + \psi = b$. We therefore have to choose $A := B - 1$, and get by the iteration method (A.8) a solution of the PV-equation. In our case B has 0 as an eigenvalue and therefore the operator $1 - \omega(1 + A)$ has 1 as an eigenvalue. The condition $\|1 - \omega(1 + A)\| < 1$ has to be understood on the sub-space orthogonal to the kernel of B and the $\psi^{(n)}$ have to lie in this sub-space. This is achieved by a projection of $\psi^{(n)}$ onto this sub-space after a couple of iterations.

The numerical algorithm (A.8) allows to overwrite the variable $\psi_i^{(n)}$ with $\psi_i^{(n+1)}$, and needs therefore a minimum of computational memory.

Appendix B

Exact Solutions of Shear Lines

B.1 Infinite θ -Band

The flow structure of a θ -band in SQG with top-hat profile can be calculated exactly by using the “contour dynamics” relation between the velocity field and temperature contours (see Dritschel 1989a). In general if $G(r)$ is the streamfunction of a point anomaly in \mathbf{x}' with $r = |\mathbf{x} - \mathbf{x}'|$, and B is a two-dimensional domain such that

$$\chi = D\psi = \begin{cases} 1 & \text{if } \mathbf{x} \in B \\ 0 & \text{elsewhere} \end{cases}$$

where D is the differential operator relating the streamfunction with the anomaly then the corresponding velocity fields $u = -\partial_y\psi$, $v = \partial_x\psi$ are given by

$$u(x, y) = -\oint_{\partial B} G(r) dx', \quad v(x, y) = -\oint_{\partial B} G(r) dy'.$$

Here the variable χ denotes either the potential temperature in SQG or the vorticity in

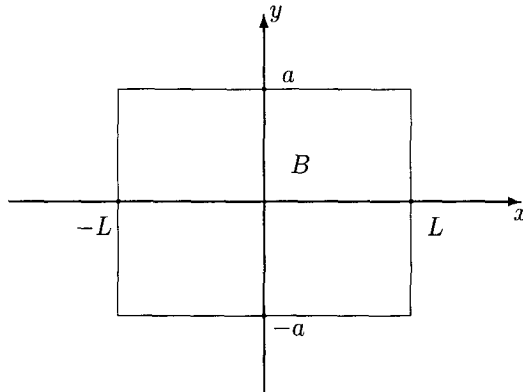


FIG. B.1: The integration domain for the contour dynamics solution of the infinite θ -strip.

BQG. Taking the Greens function of SQG we get

$$u(y) = \frac{1}{2\pi} \lim_{L \rightarrow \infty} \left\{ \int_{-L}^L \frac{dx}{\sqrt{x^2 + (y+a)^2}} - \int_{-L}^L \frac{dx}{\sqrt{x^2 + (y-a)^2}} \right\} =$$

$$\frac{1}{\pi} \lim_{L \rightarrow \infty} \left\{ \sinh^{-1} \left(\frac{L}{y+a} \right) - \sinh^{-1} \left(\frac{L}{y-a} \right) \right\}.$$

See Fig. B.1 for a prescription of the notation. On expressing the inverse of the hyperbolic function via the logarithm, the limit can be taken and we get for a temperature anomaly of amplitude Θ_0 and width $2a$:

$$u(y) = \frac{\Theta_0}{\pi} \log \left(\left| \frac{y-a}{y+a} \right| \right).$$

B.2 Infinite PV-Band

Consider an elliptic potential vorticity band. The band is characterised by a uniform q.g. PV in the interior and vanishing PV outside the band, and by the semi-axes a and c defining the horizontal and vertical scale. An exact solution of the time-independent solution is presented. The two limit forms $c \rightarrow \infty$ and $c \rightarrow 0$ yield solutions of an infinite vorticity in the BQG and θ band in the SQG framework.

$$\begin{aligned} \psi &: \mathbf{R}^3 && \rightarrow \mathbf{R} \\ (x, y, z) &\mapsto \psi(x, z) && \text{independent of } y \\ \Delta\psi &= && \begin{cases} q_0 & \text{if } ((x/a)^2 + (z/c)^2) \leq 1 \\ 0 & \text{elsewhere.} \end{cases} \end{aligned}$$

For $((x/a)^2 + (z/c)^2) \leq 1$ there exists a solution of the form

$$\psi_i(x, z) = \frac{1}{2}(Ax^2 + Bz^2).$$

$\Delta\psi_i = q_0$ yields $B = q_0 - A$, and A will be determined by the exterior solution. Introduce therefore elliptical coordinates ($a > c$):

$$\begin{aligned} x &= d \cosh \rho \cos \phi & , & & z &= d \sinh \rho \sin \phi \\ \rho &> 0 & , & & \phi &\in [0, 2\pi] \end{aligned}$$

with $a = d \cosh \rho_0$ and $c = d \sinh \rho_0$. (Note that $d^2 = a^2 - c^2$ and $e^{-2\rho_0} = \frac{a-c}{a+c}$). The inverse functions are

$$\sin^2 \phi = \frac{-(x^2 + z^2 - d^2) + \sqrt{(x^2 + z^2 - d^2)^2 + 4d^2 z^2}}{2d^2}$$

and

$$\sinh^2 \rho = \frac{(x^2 + z^2 - d^2) + \sqrt{(x^2 + z^2 - d^2)^2 + 4d^2 z^2}}{2d^2}.$$

In these coordinates the metric is:

$$g_{\mu\nu} = \frac{\partial x^\alpha}{\partial x'^\mu} \frac{\partial x^\beta}{\partial x'^\nu} \eta_{\alpha\beta} = \begin{pmatrix} h(\rho, \phi) & 0 \\ 0 & h(\rho, \phi) \end{pmatrix}$$

with $h(\rho, \phi) = d^2(\sinh^2 \rho + \sin^2 \phi)$. It follows that the Laplacian is given by:

$$\Delta(\cdot) = \frac{1}{\sqrt{g}} \partial_\mu (\sqrt{g} g^{\mu\nu} \partial_\nu(\cdot)) = \frac{1}{h(\rho, \phi)} (\partial_\rho^2(\cdot) + \partial_\phi^2(\cdot)).$$

In these new coordinates the interior streamfunction is

$$\psi_i(\rho, \phi) = \frac{1}{2} (Ad^2 \cosh^2 \rho \cos^2 \phi + (q_0 - A)d^2 \sinh^2 \rho \sin^2 \phi)$$

and thus on the boundary of the ellipse

$$\begin{aligned} \psi_i(\rho_0, \phi) &= \frac{1}{4}(Aa^2 - (q_0 - A)c^2) \cos 2\phi + \frac{1}{4}(Aa^2 + (q_0 - A)c^2) \\ \frac{\partial \psi_i}{\partial \rho}(\rho_0, \phi) &= \frac{ac}{2}(2A - q_0) \cos 2\phi + \frac{ac}{2}q_0. \end{aligned}$$

(The use of $\cos^2 \phi = \frac{1}{2}(\cos(2\phi) + 1)$ and $\sin^2 \phi = \frac{1}{2}(1 - \cos(2\phi))$ will become apparent later).

The Laplace-equation in the exterior region is solved by introducing a separation of the dependent variable, i.e.

$$\Delta(f(\rho)g(\phi)) = \frac{1}{h(\rho, \phi)}(f''(\rho)g(\phi) + f(\rho)g''(\phi)) = 0$$

so that

$$\frac{f''(\rho)}{f(\rho)} + \frac{g''(\phi)}{g(\phi)} = 0.$$

Both terms have separately to be constant and the function g must be 2π -periodic and that implies that $g''/g = -n^2$ where n is an integer. Thus the general solution of the Laplace-equation in elliptical coordinates is

$$\psi_e(\rho, \phi) = B_0 + C_0\rho + \sum_{n=1}^{\infty} (A_n \cos n\phi + B_n \sin n\phi)(e^{-n\rho} + C_n e^{n\rho}).$$

The coefficients are determined by the physical requirement of continuous velocity fields at the boundary of the ellipse, and by the fact that velocity-fields must go to zero at infinity:

$$\begin{aligned} \frac{\partial \psi_e}{\partial x} &\rightarrow 0 \quad \text{for } \rho \rightarrow \infty \\ \psi_e(\rho_0, \phi) &= \psi_i(\rho_0, \phi) \\ \frac{\partial \psi_e}{\partial \rho}(\rho_0, \phi) &= \frac{\partial \psi_i}{\partial \rho}(\rho_0, \phi) \end{aligned}$$

The inner solution on the boundary has only a $\cos(2\phi)$ term and the unbounded exponential ρ -terms must vanish, therefore the exterior solution is of the form

$$\psi_e(\rho, \phi) = \alpha + \beta\rho + \gamma \cos 2\phi e^{-2\rho},$$

and putting this in the continuity condition on the boundary of the ellipse we finally get

$$\psi_e(\rho, \phi) = \frac{acq_0}{4} \left(1 - \log \left(\frac{a+c}{a-c} \right) + 2\rho + \cos 2\phi e^{-2\rho} \right)$$

and

$$\psi_i(\rho, \phi) = \frac{q_0}{2}(a-c) \left(c \cosh^2 \rho \cos^2 \phi + a \sinh^2 \rho \sin^2 \phi \right)$$

or

$$\psi_i(x, z) = \frac{q_0}{2(a+c)} \left(cx^2 + az^2 \right)$$

We can now calculate the velocity field of this PV-band. For the exterior solution we carry out the derivatives in the elliptical coordinates and need therefore the following partial derivatives

$$\begin{pmatrix} \frac{\partial x}{\partial \rho} & \frac{\partial x}{\partial \phi} \\ \frac{\partial z}{\partial \rho} & \frac{\partial z}{\partial \phi} \end{pmatrix}^{-1} = \begin{pmatrix} \frac{\partial \rho}{\partial x} & \frac{\partial \rho}{\partial z} \\ \frac{\partial \phi}{\partial x} & \frac{\partial \phi}{\partial z} \end{pmatrix} = \frac{1}{h(\rho, \phi)} \begin{pmatrix} d \sinh \rho \cos \phi & d \cosh \rho \sin \phi \\ -d \cosh \rho \sin \phi & d \sinh \rho \cos \phi \end{pmatrix}.$$

Thus for example

$$v(x, 0) = \begin{cases} q_0 \frac{ac}{a^2 - c^2} \left(x + \sqrt{x^2 - a^2 + c^2} \right) & x < -a \\ q_0 \frac{c}{a+c} x & -a \leq x \leq a \\ q_0 \frac{ac}{a^2 - c^2} \left(x - \sqrt{x^2 - a^2 + c^2} \right) & x > a. \end{cases}$$

In Fig. B.2 the velocity field of a shallow PV strip with $a : c = 1 : 3$ according to the above formulae is shown.

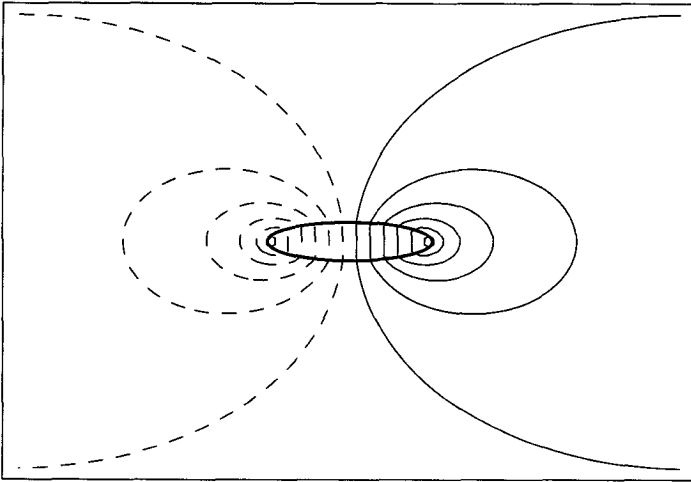


FIG. B.2: Velocity field (thin solid and dashed lines) of an elliptical infinite PV strip (overlaid bold line) in an unbounded atmosphere. The ratio $a : c$ is $1 : 3$.

B.3 The Kirchhoff Ellipse

The horizontal infinite elliptical PV-band in QG is mathematically isomorphic to an elliptical vorticity distribution in BQG (with z replaced by y). From this solution one derives easily the Kirchhoff solution for a steadily rotating vorticity ellipse. The previous solution equals to the streamfunction of a vorticity ellipse. In a frame rotating with constant angular velocity Ω the streamfunction transforms according to

$$\tilde{\psi}(x, y) = \psi(x, y) - \frac{\Omega}{2} (x^2 + y^2) .$$

If the ellipse is at rest in the rotating frame, the streamfunction must be constant on the boundary of the ellipse, i.e.

$$\frac{\partial \tilde{\psi}}{\partial \phi}(\rho_0, \phi) = \frac{\partial \tilde{\psi}_e}{\partial \phi}(\rho_0, \phi) = \frac{\partial \tilde{\psi}_i}{\partial \phi}(\rho_0, \phi) = 0 ,$$

thus there must be an Ω value such that (we use $\tilde{\psi}_i$)

$$\partial_\phi \left(\left(\frac{q_0 b}{a+b} - \Omega \right) a^2 \cos^2 \phi + \left(\frac{q_0 a}{a+b} - \Omega \right) b^2 \sin^2 \phi \right) = 0 , \quad \forall \phi$$

which is fulfilled if and only if

$$\Omega = q_0 \frac{ab}{(a+b)^2} .$$

Leer - Vide - Empty

Appendix C

The Profile Parameter

To construct profiles for the potential temperature and the PV anomalies we introduce a one-parameter family of “kink”-functions κ_δ such that: $\kappa_\delta(x) = 0$ for $x < 0$ and $\kappa_\delta(x) = \frac{1}{2}(2x)^\delta$ for $x \in [0, 1/2]$ with $\delta \geq 1$. Thus κ_δ is a continuous function for $x < 1/2$ and $\kappa_\delta(1/2) = 1/2$. For $x > 1/2$ we define $\kappa_\delta(x) = 1 - \kappa_\delta(1 - x)$, i.e. κ_δ is symmetric with respect to $(1/2, 1/2)$. Note that the derivative of κ_δ at $1/2$ is $\kappa'_\delta(1/2) = \delta$, i.e. the parameter of this “kink”-function describes the maximal slope. In Fig. C.1 the graphs of κ_δ are plotted for $\delta = 2$ and $\delta = 6$.

Utilising this function we define a hat-profile of half-width a and amplitude Θ_0 by:

$$\Theta(x) = \begin{cases} \Theta_0 \kappa_\delta(1 + x/a) & : x \leq 0 \\ \Theta_0 \kappa_\delta(1 - x/a) & : x > 0 \end{cases}$$

and the slope at half width is given by

$$\Theta'(-d/2) = \delta \frac{\Theta_0}{a}.$$

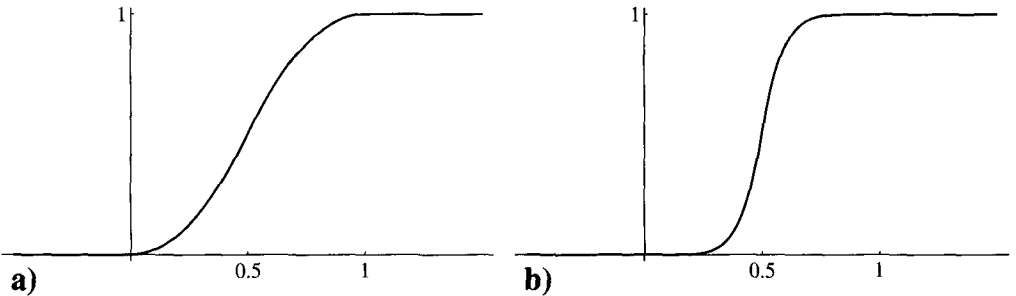


FIG. C.1: The kink function for $\delta = 2$ (panel a) and $\delta = 6$ (panel b).

Leer - Vide - Empty

Appendix D

Linear Instability

D.1 Transformation into an Algebraic Problem

The spectral representation of the shear component of the basic state streamfunction is given by a decomposition of the shear velocity:

$$\Lambda x = \sum_l \lambda_l e^{ik_l x} \quad (\text{D.1})$$

which gives

$$\lambda_l = \begin{cases} \Lambda(a+b)/2 & (l=0) \\ \Lambda i \exp(ik_l a)/k_l & (l \neq 0). \end{cases} \quad (\text{D.2})$$

Integrating yields

$$\bar{\psi}_{sh} = \sum_{l \neq 0} \frac{\lambda_l}{ik_l} e^{ik_l x} + \lambda_0 x. \quad (\text{D.3})$$

and the Fourier transformation of the periodic part of the surface temperature gives the Fourier coefficients

$$\vartheta_l = \frac{1}{L} \int_a^b \bar{\Theta}_p(x) e^{-ik_l x} dx. \quad (\text{D.4})$$

This gives the following spectral representation of the zonal streamfunction

$$\bar{\psi} = \sum_{l \neq 0} -\frac{\vartheta_l}{|k_l|} e^{-|k_l|z} e^{ik_l x} + Bxz + \sum_{l \neq 0} \frac{\lambda_l}{ik_l} e^{ik_l x} + \lambda_0 x. \quad (\text{D.5})$$

For the perturbation we put

$$\psi'(x, y, z, t) = \sum_l P_l^{(m)} e^{ik_l x} e^{imy} e^{-\mu_{l,m} z} e^{\sigma_m t}$$

with $\mu_{l,m} = \sqrt{k_l^2 + m^2}$, i.e. $q' = 0$, m is the zonal wavenumber. Inserting in the linearised thermodynamic equation (3.7) yields the eigenvalue problem

$$MP^{(m)} = \sigma_m P^{(m)}$$

with matrix elements of M :

$$\begin{aligned}
 M_{l,l'} &= -im(A_{l-l'} + \mu_{l',m}D_{l-l'})/\mu_{l,m} \\
 A_l &= \begin{cases} B & \text{if } (l=0) \\ ik_l\vartheta_l & \text{if } (l \neq 0) \end{cases} \\
 D_l &= \begin{cases} \Lambda(a+b)/2 & \text{if } (l=0) \\ -isgn(l)\vartheta_l + \Lambda i \exp(-ik_l a)/k_l & \text{if } (l \neq 0). \end{cases}
 \end{aligned} \tag{D.6}$$

D.2 Numerical Treatment

To solve the algebraic problem, we compute the Fourier coefficients ϑ_l numerically and approximate M by a finite dimensional matrix. Different values of the baroclinicity and the barotropic shear do not require a recalculation of the Fourier coefficients. It is therefore comparatively cheap to calculate a large number (here 1024) of the coefficients to yield an accurate result for the first few coefficients that are needed in the truncated matrix M .

The algebraic eigenvalue problem is truncated on 186 complex coefficients for all results presented in chapter 3. Fig. D.1 shows the growth rate for a truncation on 186 and 230 complex dimensions, and indicates that the results are for wavenumbers less than 2 not sensitive on the chosen truncation. For wavenumbers between 2 and 4 the difference remains less than 10%. (Eigenvalues and eigenvectors of the matrix are computed with the NAGLIB routine for general complex matrices).

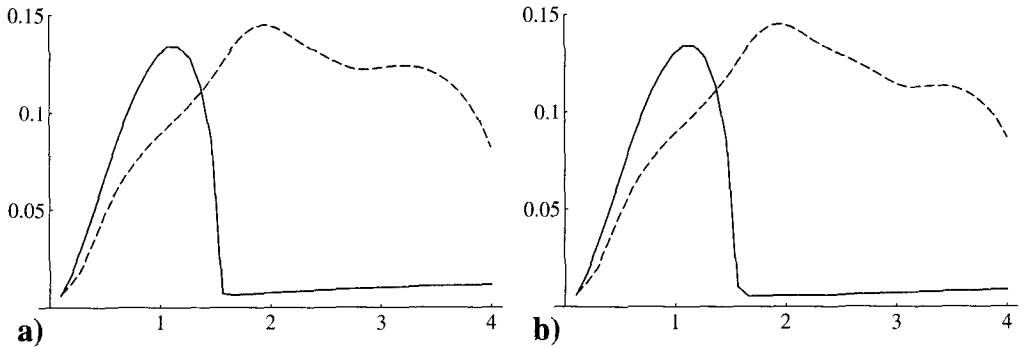


FIG. D.1: The growth rate calculated with a truncation on 186 (panel a) and 230 (panel b) complex dimensions. The profile, shear, and baroclinicity are $\delta = 4$, $\Lambda = 0$, and $B = 0$ for the solid line, and $\delta = 6$, $\Lambda = -0.25$, and $B = 0.5$ for the dashed line.

Appendix E

The Effect of the Resolution and the Domain Size in Numerical Nonlinear SQG Dynamics

The effect of the resolution and the domain size of numerical integration shall be tested by three simulations of an elliptical θ -anomaly of length $a = 5$ and width $b = 1$ in dimensionless units in an unsheared barotropic environment. The profile parameter as introduced in chapter 3 is $\delta = 2$. The three simulations to be compared are shown in Fig. E.1 at $t = 50$ and are characterised by the following values for the domain size and the number of spectral components:

	domain size	spectral components
panel a)	8×8	512×512
panel b)	8×8	256×256
panel c)	16×16	512×512

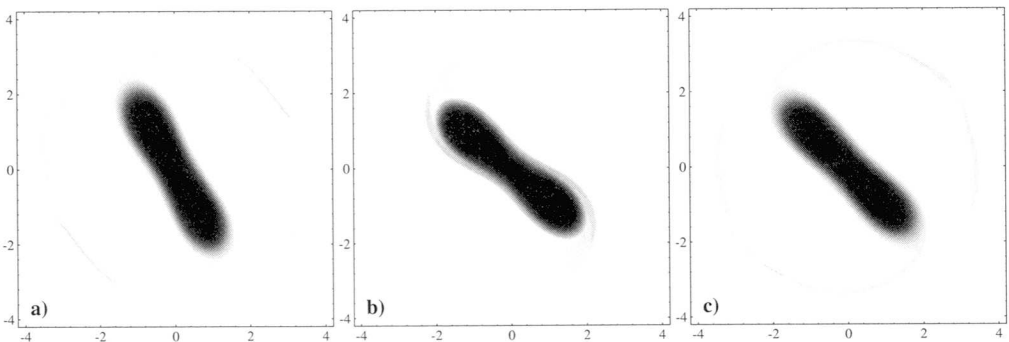


FIG. E.1: Nonlinear evolution of a finite θ -strip at $t = 50$ for length to width $5 : 1$ and integration domain 8×8 (panel a and b) and 16×16 (panel c). The number of spectral components in each direction is 512 in panel a) and 256 in panel b) and c).

Panel a) and b) represent integrations on a small integration domain but with high and low resolution, panel b) and c) represent simulations with the same resolution but on a small and on a large integration domain. Note that the angular velocity of the rotating strip depends on both the resolution and on the size of the integration domain.

References

- Appenzeller, C. 1994. *Wave Developments on Surface Fronts and Stratospheric Intrusions*. PhD thesis. Swiss Federal Institute of Technology (ETH). Dissertation Nr. 10471.
- Appenzeller, C., and H. C. Davies. 1992. Structure of stratospheric intrusions into the troposphere. *Nature* **358**, 570–572.
- Appenzeller, C., and H. C. Davies. 1996. PV morphology of a frontal-wave development. *Meteorol. Atmos. Phys.* **58**, 21–40.
- Appenzeller, C., H. C. Davies, and W. A. Norton. 1996. Fragmentation of stratospheric intrusions. *J. Geophys. Res.* **101**, 1435–1456.
- Berrisford, P. 1988. *Potential Vorticity in Extratropical Cyclones*. PhD thesis. University of Reading.
- Bishop, C. H. 1996a. Domain independent attribution. Part I: Reconstructing the wind from estimates of vorticity and divergence using free space Greens functions. *J. Atmos. Sci.* **53**, 241–252.
- Bishop, C. H. 1996b. Domain independent attribution. Part II: Its value in the verification of dynamical theories of frontal waves and frontogenesis. *J. Atmos. Sci.* **53**, 253–262.
- Bishop, C. H., and A. J. Thorpe. 1994a. Frontal wave stability during moist deformation frontogenesis. Part I: Linear wave dynamics. *J. Atmos. Sci.* **51**, 852–873.
- Bishop, C. H., and A. J. Thorpe. 1994b. Frontal wave stability during moist deformation frontogenesis. Part II: The suppression of nonlinear wave development. *J. Atmos. Sci.* **51**, 874–888.
- Bishop, C. H., and A. J. Thorpe. 1994c. Potential vorticity and the electrostatics analogy: Quasi-geostrophic theory. *Quart. J. Roy. Meteor. Soc.* **120**, 713–731.
- Bjerknes, J. 1919. On the structure of moving cyclones. *Geofys. Publ.* **1**, 1–8.
- Bjerknes, J., and H. Solberg. 1922. Life cycles of cyclones and the polar front theory of atmospheric circulation. *Geofys. Publ.* **3**, 3–18.
- Blackmon, M. L., J. M. Wallace, N.-C. Lau, and S. L. Mullen. 1977. An observational study of the Northern Hemisphere wintertime circulation. *J. Atmos. Sci.* **34**, 1040–1053.

- Bleck, R. 1990. Depiction of upper/lower vortex interaction associated with extratropical cyclogenesis. *Mon. Wea. Rev.* **118**, 573–585.
- Blumen, W. 1978. Uniform potential vorticity flow: Part I. Theory of wave interactions and two-dimensional turbulence. *J. Atmos. Sci.* **35**, 774–783.
- Bolton, D. 1980. The computation of equivalent potential temperature. *Mon. Wea. Rev.* **108**, 1046–1053.
- Boyle, J. S., and L. F. Bosart. 1986. Cyclone-anticyclone couplets over North America. Part II: Analysis of a major cyclone event over the eastern United States. *Mon. Wea. Rev.* **114**, 2432–2465.
- Bretherton, F. P. 1966. Critical layer instability in baroclinic flows. *Quart. J. Roy. Meteor. Soc.* **92**, 325–334.
- Browning, K. A., and N. M. Roberts. 1994. Structure of a frontal cyclone. *Quart. J. Roy. Meteor. Soc.* **120**, 1535–1557.
- Charney, J. G. 1947. The dynamics of long waves in a baroclinic westerly current. *J. Met.* **4**, 135–163.
- Charney, J. G. 1955. The use of primitive equations in numerical prediction. *Tellus* **7**, 22–26.
- Charney, J. G., and M. E. Stern. 1962. On the stability of internal baroclinic jets in a rotating atmosphere. *J. Atmos. Sci.* **19**, 159–172.
- Constantin, P., A. J. Majda, and E. G. Tabak. 1994. Singular front formation in a model for quasi-geostrophic flow. *Phys. Fluids* **6**, 9–11.
- Davies, H. C. 1994. Theories of frontogenesis. In *Proceedings of an international symposium on the life cycles of extratropical cyclones*. S. Grønås, and M. A. Shapiro. (Eds.). Vol. I. Bergen, Norway. Pp. 182–192.
- Davies, H. C., and C. H. Bishop. 1994. Eady edge waves and rapid development. *J. Atmos. Sci.* **51**, 1930–1946.
- Davies, H. C., C. Schär, and H. Wernli. 1991. The palette of fronts and cyclones within a baroclinic wave development. *J. Atmos. Sci.* **48**, 1666–1689.
- Davis, C. A. 1992. Piecewise potential vorticity inversion. *J. Atmos. Sci.* **49**, 1397–1411.
- Davis, C. A., and K. A. Emanuel. 1991. Potential vorticity diagnostic of cyclogenesis. *Mon. Wea. Rev.* **119**, 1929–1953.
- Davis, C. A., M. T. Stoelinga, and Y.-H. Kuo. 1993. The integrated effect of condensation in numerical simulations of extratropical cyclogenesis. *Mon. Wea. Rev.* **121**, 2309–2330.

- Dritschel, D. G. 1989a. Contour dynamics and contour surgery : Numerical algorithms for extended, high-resolution modelling of vortex dynamics in two-dimensional, inviscid, incompressible flows. *Comput. Phys. Rep.* **10**, 77–146.
- Dritschel, D. G. 1989b. On the stabilization of a two-dimensional vortex strip by adverse shear. *J. Fluid Mech.* **206**, 193–221.
- Eady, E. T. 1949. Long waves and cyclone waves. *Tellus* **1**, 33–52.
- Ehrendorfer, M., and R. M. Errico. 1995. Mesoscale predictability and the spectrum of optimal perturbations. *J. Atmos. Sci.* **52**, 3475–3500.
- Eliassen, A. 1983. The Charney-Stern theorem on barotropic-baroclinic instability. *Pure Appl. Geophys.* **121**, 563–572.
- Errico, R. M., and D. P. Baumhefner. 1987. Predictability experiments using a high-resolution limited-area model. *Mon. Wea. Rev.* **115**, 408–504.
- Errico, R. M., and T. Vukicevic. 1992. Sensitivity analysis using an adjoint of the PSU-NCAR mesoscale model. *Mon. Wea. Rev.* **120**, 1644–1660.
- Errico, R. M., T. Vukicevic, and K. Raeder. 1993. Comparison of initial and lateral boundary condition sensitivity for a limited-area model. *Tellus* **45A**, 539–557.
- Ertel, H. 1942. Ein neuer hydrodynamischer Wirbelsatz. *Meteor. Z.* **59**, 277–281.
- Fehlmann, R., and H. C. Davies. 1997. Misforecasts of synoptic systems: Diagnosis via PV-retrodiction. *Mon. Wea. Rev.* **125**, 2247–2264.
- Gall, R. 1976. Structure changes of growing baroclinic waves. *J. Atmos. Sci.* **33**, 374–390.
- Gyakum, J. R., and co authors. 1995. First COMPARE Workshop: 5–9 October 1994, Montreal, Quebec, Canada. *Bull. Amer. Meteor. Soc.* **76**, 1209–1218.
- Hakim, G. J., D. Keyser, and L. F. Bosart. 1996. The Ohio Valley wave-merger cyclogenesis event from 25–26 January 1978. Part II: Diagnosis using quasigeostrophic potential vorticity inversion. *Mon. Wea. Rev.* **124**, 2176–2205.
- Haynes, P. H., and M. E. McIntyre. 1987. On the evolution of isentropic distributions of potential vorticity in the presence of diabatic heating and frictional or other forces. *J. Atmos. Sci.* **44**, 828–841.
- Held, I. M., R. T. Pierrehumbert, S. T. Garner, and K. L. Swanson. 1995. Surface quasi-geostrophic dynamics. *J. Fluid Mech.* **282**, 1–20.
- Holton, J. R., P. H. Haynes, M. E. McIntyre, A. R. Douglass, R. B. Rood, and L. Pfister. 1995. Stratosphere-troposphere exchange. *Reviews of Geophysics* **33**, 403–439.
- Hortal, M. 1991. Numerical methods in atmospheric models. *Technical report*. European Center for Medium Range Weather Forecasts. Reading UK.

- Hoskins, B. J. 1991. Towards a PV- θ view of the general circulation. *Tellus* **43AB**, 27–35.
- Hoskins, B. J., and P. Berrisford. 1988. A potential vorticity perspective of the storm of 15–16 October 1987. *Weather* **43**, 122–129.
- Hoskins, B. J., H. H. Hsu, I. N. James, M. Masutani, P. D. Sardeshmukh, and G. H. White. 1989. Diagnostics of the global atmospheric circulation based on ECMWF analyses 1979–1989. *WMO/TD* **326**, Pp. 219.
- Hoskins, B. J., I. Draghici, and H. C. Davies. 1978. A new look at the ω -equation. *Quart. J. Roy. Meteor. Soc.* **104**, 31–38.
- Hoskins, B. J., M. E. McIntyre, and A. W. Robertson. 1985. On the use and significance of isentropic potential vorticity maps. *Quart. J. Roy. Meteor. Soc.* **111**, 877–946.
- Houtekamer, P. L., and J. Derome. 1994. Prediction experiments with two-member ensembles. In *Proceedings of an international symposium on the life cycles of extratropical cyclones*. S. Grønås, and M. A. Shapiro. (Eds.). Vol. III. Bergen, Norway. Pp. 2179–2191.
- Hoyer, J.-M., and R. Sadourny. 1982. Closure modelling of fully developed baroclinic instability. *J. Atmos. Sci.* **39**, 707–721.
- Joly, A. 1995. The stability of steady fronts and the adjoint method: Non-modal frontal waves. *J. Atmos. Sci.* **52**, 3082–3108.
- Joly, A., and A. J. Thorpe. 1990a. Frontal instability generated by tropospheric potential vorticity anomalies. *Quart. J. Roy. Meteor. Soc.* **116**, 525–560.
- Joly, A., and A. J. Thorpe. 1990b. The stability of a steady horizontal shear front with uniform potential vorticity. *J. Atmos. Sci.* **47**, 2612–2622.
- Juckes, M. 1994. Quasi-geostrophic dynamics of the tropopause. *J. Atmos. Sci.* **51**, 2756–2768.
- Juckes, M. 1995. Instability of surface and upper-tropospheric shear lines. *J. Atmos. Sci.* **52**, 3247–3262.
- Keyser, D., M. J. Reeder, and R. J. Reed. 1988. A generalization of Pettersen's frontogenesis function and its relation to the forcing of vertical motion. *Mon. Wea. Rev.* **116**, 762–780.
- Kleinschmidt, E. 1950. Über Aufbau und Entstehung von Zyklonen, Teil 1. *Meteor. Rundsch.* **3**, 1–6.
- Kuo, Y.-H., and R. J. Reed. 1988. Numerical simulations of an explosively deepening cyclone in the eastern Pacific. *Mon. Wea. Rev.* **116**, 2081–2105.
- Langland, R. H., R. L. Elsberry, and R. M. Errico. 1995. Evaluation of physical processes in an idealized extratropical cyclone using adjoint sensitivity. *Quart. J. Roy. Meteor. Soc.* **121**, 1349–1386.

- Love, A. E. H. 1893. On the stability of certain vortex motions. *Proc. London Math. Soc.* **25**, 18–42.
- Lüthi, D., A. Cress, H. C. Davies, C. Frei, and C. Schär. 1996. Interannual variability and regional climate simulations. *Theor. Appl. Climatol.* **53**, 185–209.
- Majewski, D. 1991. The Europa-Modell of the Deutscher Wetterdienst. *Numerical methods in atmospheric models*. Vol. 2. European Centre for Medium Range Weather Forecasts, Reading, GB.
- Malardel, S., A. Joly, F. Courbet, and P. Courtier. 1993. Nonlinear evolution of ordinary frontal waves induced by low-level potential vorticity anomalies. *Quart. J. Roy. Meteor. Soc.* **119**, 681–713.
- Marshall, J., and F. Molteni. 1993. Toward a dynamical understanding of planetary-scale regimes. *J. Atmos. Sci.* **50**, 1792–1818.
- Mattocks, C., and R. Bleck. 1986. Jet streak dynamics and geostrophic adjustment processes during the initial stage of lee cyclogenesis. *Mon. Wea. Rev.* **114**, 2033–2056.
- Meacham, S. P. 1992. Quasigeostrophic, ellipsoidal vortices in a stratified fluid. *Dyn. Atmos. Oceans* **16**, 189–223.
- Melander, M. V., J. C. McWilliams, and N. J. Zabusky. 1987. Axisymmetrization and vorticity-gradient intensification of an isolated two-dimensional vortex through filamentation. *J. Fluid Mech.* **178**, 137–159.
- Miller, J. E. 1948. On the concept of frontogenesis. *J. Meteor.* **5**, 169–171.
- Molteni, F., R. Buizza, T. N. Palmer, and T. Petroliagis. 1996. The ECMWF ensemble prediction system: Methodology and validation. *Quart. J. Roy. Meteor. Soc.* **122**, 73–120.
- Moore, G. W. K., and W. R. Peltier. 1987. Cyclogenesis in frontal zones. *J. Atmos. Sci.* **44**, 384–409.
- Mullen, S. L., and D. L. Baumhefner. 1989. The impact of initial condition uncertainty on numerical simulations of large-scale explosive cyclogenesis. *Mon. Wea. Rev.* **117**, 2800–2821.
- Norton, W. A. 1994. Breaking Rossby waves in a model stratosphere diagnosed by a vortex-following coordinate system and a technique for advecting material contours. *J. Atmos. Sci.* **51**, 654–673.
- Orlanski, I. 1968. Instability of frontal waves. *J. Atmos. Sci.* **25**, 178–200.
- Petterssen, S. 1936. A contribution to the theory of frontogenesis. *Geofys. Publ.* **11**, 1–27.

- Petterssen, S. 1956. *Weather analysis and Forecasting*. In: Motion and motion systems. Pp. 428. Vol. I. Mc-Graw-Hill.
- Petterssen, S., and S. J. Smebye. 1971. On the development of extratropical cyclones. *Quart. J. Roy. Meteor. Soc.* **97**, 457–482.
- Polavarapu, S. M., and W. R. Peltier. 1993. Formation of small-scale cyclones in numerical simulations of synoptic-scale baroclinic wave life cycles: Secondary instability at the cusp. *J. Atmos. Sci.* **50**, 1047–1057.
- Rabier, R., E. Klinker, P. Courtier, and A. Hollingsworth. 1996. Sensitivity of forecast errors to initial conditions. *Quart. J. Roy. Meteor. Soc.* **122**, 121–150.
- Rabier, R., P. Courtier, and O. Talagrand. 1992. An application of adjoint models to sensitivity analysis. *Beitr. Phys. Atmos* **65**, 177–192.
- Reed, R. J., A. J. Simmons, M. D. Albright, and P. Undén. 1988. The role of latent heat release in explosive cyclogenesis: Three examples based on ECMWF operational forecasts. *Wea. Forecasting* **3**, 217–229.
- Reed, R. J., M. T. Stoelinga, and Y.-H. Kuo. 1992. A model-aided study of the origin and evolution of the anomalously high potential vorticity in the inner region of rapidly deepening marine cyclone. *Mon. Wea. Rev.* **120**, 893–913.
- Renfrew, I. A., A. J. Thorpe, and C. H. Bishop. 1997. The role of the environmental flow in the development of secondary frontal cyclones. *Quart. J. Roy. Meteor. Soc.* **123**, 1653–1675.
- Rose, H. A., and P. L. Sulem. 1978. Fully developed turbulence and statistical mechanics. *J. Phys. Paris* **47**, 441–484.
- Rossa, A. 1995. *The Impact of Latent Heat Release on the Dynamics of Extratropical Cyclogenesis*. PhD thesis. Swiss Federal Institute of Technology (ETH). Dissertation Nr. 11039.
- Rossby, C. G. 1940. Planetary flow patterns in the atmosphere. *Quart. J. Roy. Meteor. Soc.* **66**, 68–87.
- Schär, C., and H. C. Davies. 1990. An instability of mature cold fronts. *J. Atmos. Sci.* **47**, 929–950.
- Schär, C., and H. Wernli. 1993. Structure and evolution of an isolated semi-geostrophic cyclone. *Quart. J. Roy. Meteor. Soc.* **119**, 57–90.
- Schär, C., and R. B. Smith. 1993. Shallow-water flow past isolated topography. Part I: Vorticity production and wake formation. *J. Atmos. Sci.* **50**, 1373–1400.
- Seibert, P. 1993. Convergence and accuracy of numerical methods for trajectory calculations. *J. Appl. Meteor.* **32**, 558–566.

- Shapiro, M. A. 1976. The role of turbulent heat flux in the generation of potential vorticity in the vicinity of upper level jet stream systems. *Mon. Wea. Rev.* **104**, 892–906.
- Shapiro, M. A., and D. Keyser. 1990. Fronts, jet streams and the tropopause. Pp. 167–191. In *Extratropical cyclones: The Erik Palmén memorial volume*. C. Newton, and E. O. Holopainen. (Eds.). American Meteorological Society, Boston.
- Shutts, G. J. 1990. Dynamical aspects of the October storm 1987: A study of a successful fine-mesh model simulation. *Quart. J. Roy. Meteor. Soc.* **116**, 1315–1347.
- Simmons, A. J. 1991. Development of a high resolution, semi-Lagrangian version of the ECMWF forecast model. *Numerical methods in atmospheric models*. Vol. 2. European Centre for Medium Range Weather Forecasts, Reading, GB.
- Simmons, A. J. 1994. Numerical simulations of cyclone life cycles. In *Proceedings of an international symposium on the life cycles of extratropical cyclones*. S. Grønås, and M. A. Shapiro. (Eds.). Vol. I. Bergen, Norway. Pp. 149–160.
- Simmons, A. J., and B. J. Hoskins. 1976. Baroclinic instability on the sphere: Normal modes of the primitive and quasi-geostrophic equations. *J. Atmos. Sci.* **33**, 1454–1477.
- Simmons, A. J., and B. J. Hoskins. 1978. The life cycles of some nonlinear baroclinic waves. *J. Atmos. Sci.* **35**, 414–432.
- Simmons, A. J., and B. J. Hoskins. 1979. The downstream and upstream development of unstable baroclinic waves. *J. Atmos. Sci.* **36**, 1239–1254.
- Simmons, A. J., and B. J. Hoskins. 1980. Barotropic influences on the growth and decay of nonlinear baroclinic waves. *J. Atmos. Sci.* **37**, 1679–1684.
- Simmons, A. J., R. Mureau, and T. Petroliaigis. 1995. Error growth and estimates of predictability from the ECMWF forecasting system. *Quart. J. Roy. Meteor. Soc.* **121**, 1739–1771.
- Sinton, D. M., and C. R. Mechoso. 1984. Nonlinear evolution of frontal waves. *J. Atmos. Sci.* **41**, 3501–3517.
- Snyder, C., W. C. Skamarock, and R. Rotunno. 1991. A comparison of primitive-equation and semigeostrophic simulations of baroclinic waves. *J. Atmos. Sci.* **48**, 2179–2194.
- Thorncroft, C. D., and B. J. Hoskins. 1990. Frontal cyclogenesis. *J. Atmos. Sci.* **47**, 2317–2336.
- Thorncroft, C. D., B. J. Hoskins, and M. E. McIntyre. 1993. Two paradigms of baroclinic-wave life-cycle behaviour. *Quart. J. Roy. Meteor. Soc.* **119**, 17–56.
- Thorpe, A. J. 1986. Synoptic scale disturbances with circular symmetry. *Mon. Wea. Rev.* **114**, 1384–1389.

- Thorpe, A. J., and C. H. Bishop. 1995. Potential vorticity and the electrostatics analogy: Ertel-Rossby formulation. *Quart. J. Roy. Meteor. Soc.* **121**, 1477–1495.
- Thorpe, A. J., and K. A. Emanuel. 1985. Frontogenesis in the presence of small stability to slantwise convection. *J. Atmos. Sci.* **42**, 1809–1824.
- Tribbia, J. J., and D. P. Baumhefner. 1988. The reliability of improvements in deterministic short-range forecasts in the presence of initial state and modeling deficiencies. *Mon. Wea. Rev.* **116**, 2276–2288.
- Uccellini, L. W. 1990. Processes contributing to the rapid development of extratropical cyclones. Pp. 81–105. In *Extratropical cyclones: The Erik Palmén memorial volume*. C. Newton, and E. O. Holopainen. (Eds.). American Meteorological Society, Boston.
- Uccellini, L. W., D. Keyser, K. F. Brill, and C. H. Wash. 1985. The Presidents' Day cyclone of 18–19 February 1979: Influence of upstream trough amplification and associated tropopause folding on rapid cyclogenesis. *Mon. Wea. Rev.* **113**, 962–988.
- Van Tuyl, A. H., and R. M. Errico. 1989. Scale interaction and predictability in a mesoscale model. *Mon. Wea. Rev.* **117**, 495–517.
- Vukicevic, T. 1991. Nonlinear and linear evolution of initial forecast errors. *Mon. Wea. Rev.* **119**, 1602–1611.
- Wernli, H. 1995. *Lagrangian Perspective of Extratropical Cyclogenesis*. PhD thesis. Swiss Federal Institute of Technology (ETH). Dissertation Nr. 11016.
- Wernli, H. 1997. A Lagrangian-based analysis of extratropical cyclones. Part II: A detailed case study. *Quart. J. Roy. Meteor. Soc.* **123**, 1677–1706.
- Wernli, H., and H. C. Davies. 1997. A Lagrangian-based analysis of extratropical cyclones. Part I: The method and some applications. *Quart. J. Roy. Meteor. Soc.* **123**, 467–489.
- Wernli, H., R. Fehlmann, and D. Lüthi. 1997. The effect of barotropic shear on upper-level induced cyclogenesis: Semigeostrophic and primitive equation numerical simulations. *J. Atmos. Sci.*, accepted.
- Whitaker, J. S., L. W. Uccellini, and K. F. Brill. 1988. A model-based diagnostic study of the rapid development phase of the President's Day cyclone. *Mon. Wea. Rev.* **116**, 2337–2365.
- Wirth, V. 1996. Quasi-geostrophic dynamics of an upper tropospheric PV anomaly in two idealized high resolution models and related stratosphere-troposphere exchange. *Beitr. Phys. Atmosph.* **69**, 333–347.
- Wirth, V., C. Appenzeller, and M. Juckes. 1997. Signatures of induced vertical air motion accompanying quasi-horizontal roll-up of stratospheric intrusions. *Mon. Wea. Rev.* **125**, 2504–2519.

Acknowledgments / Dank

The present work would not have been possible without the help of many persons to whom I am indebted. I would like to express my gratitude to

Huw Davies who gave me, as a newcomer in the field of dynamical meteorology, the chance to work with him. He introduced me into the world of atmospheric dynamics and supported me through many valuable discussions. He also gave me the opportunity to present my work at international conferences.

My co-examiners Adrian Simmons and Christoph Schär who reviewed carefully the present thesis.

Weiter gilt mein herzlicher Dank

Heini Wernli für seine stetige Hilfsbereitschaft in der Bedienung der Modelle und der zur Verfügungstellung des Trajektorien-Paketes und dessen Anpassung auf meine spezifischen Bedürfnisse. Seinem Enthusiasmus für dynamische Meteorologie verdanke ich es auch, dass ich den Weg ans Institut für Atmosphärenphysik gefunden habe.

Daniel Lüthi für seine Hilfsbereitschaft bei allen Problemen, welche bei der Benützung des Europa-Modells auftraten.

Dem Deutschen Wetterdienst (DWD) und der Schweizerischen Meteorologischen Anstalt (SMA) für die zur Verfügungstellung des Vorhersagemodells und der EZMW-Daten.

Eugen Müller, Michael Sprenger und Christian Quadri für den Einsatz, den sie als Diplomanden leisteten. Es bereitete mir Freude, ihre Diplomarbeiten zu betreuen und jene von Eugen löste meine Arbeit von Kapitel 5 aus.

Allen Mitarbeiterinnen und Mitarbeitern des Instituts für Atmosphärenphysik, die mit ihrem Einsatz eine ausgezeichnete Infrastruktur aufbauten und aufrecht erhalten.

Prof. C. Constantinescu und Prof. C. Blatter dafür, dass sie es mir ermöglichten, als Mathematik-Assistent Erfahrungen in der Arbeit mit Studenten zu sammeln. Allen Assistentinnen und Assistenten der Mathematik-Assistenz II für die Zusammenarbeit und für die unterhalt-same Zeit.

Dani Perruchoud für den Austausch verschiedener Erfahrungen mit dem Textverarbeitungssystem \LaTeX .

René Fehlmann, Juli 1997

Leer - Vide - Empty

Curriculum Vitae

René Fehlmann, born on April 23 1966 in Dornach (SO), Switzerland, married with Ursula Fehlmann-Walter

EDUCATION AND PROFESSIONAL TRAINING

1981 – 85 Kantonsschule Romanshorn

Matura Type C

1986 – 91 University study in Physics at the Swiss Federal Institute of Technology (ETH) Zürich. Specialisation in the fields *Theoretical Physics* and *Algebra*. Diploma thesis “*Quantum Group Symmetries in the Sine-Gordon Model*” under the guidance of Prof. G. Felder

Dipl. Phys. ETH

1992 – 96 Teaching assistant at the Mathematics Department, ETH Zürich

1993 – 96 Ph.D. student at the Institute for Atmospheric Science, ETH Zürich, in the group for Theoretical Meteorology of Prof. H. C. Davies

INTERNATIONAL CONFERENCES AND WORKSHOPS

Workshop on Geometrical and Algebraic Methods in Quantum Physics, Centro Stefano Franscini, Ascona 1992; EGS Hamburg 1995; 10th Conf. on Waves and Instabilities, Big Sky 1995; 11th Conf. on Numerical Weather Prediction, Norfolk 1996; 7th Conf. on Mesoscale Processes, Reading 1996; MAP Meeting, Belgirate 1997.

SPECIAL TRAINING COURSE

Summer School in Geophysical and Environmental Fluid Dynamics, University of Cambridge 1994.

CURRENT ADDRESS

René Fehlmann
Unterdorfstrasse 19
CH – 8105 Watt

e-mail: fehlmann@atmos.umnw.ethz.ch